Doctoral Thesis

# Design of catalyst support for high durability of oxygen electrocatalyst

Juchan Yang

Department of Energy Engineering

Graduate School of UNIST

2018

# Design of catalyst support for high durability of oxygen electrocatalyst

Juchan Yang

Department of Energy Engineering

Graduate School of UNIST

# Design of catalyst support for high durability of oxygen electrocatalyst

A thesis/dissertation
submitted to the Graduate School of UNIST
in partial fulfillment of the
requirements for the degree of
Doctor of Philosophy

Juchan Yang

6. 11. 2018
Approved by

_____

Advisor
Hyun-Kon Song

# Design of catalyst support for high durability of oxygen electrocatalyst

Juchan Yang

This certifies that the thesis/dissertation of Juchan Yang is approved.

6. 11. 2018

_____

Advisor: Hyun-Kon Song

_____

Jong-Beom Baek: Thesis Committee Member #1

_____

Youngsik Kim: Thesis Committee Member #2

_____

Sang Hoon Joo: Thesis Committee Member #3

_____

Youngkook Kwon: Thesis Committee Member #4;

# Abstract

In Polymer electrolyte membrane fuel cells (PEMFC) and direct methanol fuel cell (DMFC) systems, the catalyst is supported on a conductive porous support for high stability and activity. The support should have adequate surface area, porosity, electrical conductivity, electrochemical stability, surface functional groups, and the like. The suitable supports for metal nanoparticle should be included (1) high electrical conductivity (2) high catalyst-support interactions (3) large surface area (4) adequate porous structure to maximize the triple phase interface (5) ease of water management to prevent flooding; (6) high corrosion resistance, and (7) easy recovery of the catalyst. Therefore, the choice of a suitable support will have a key impact on determining the catalyst, and hence the behavior, performance, lifetime and cost of the fuel cell. Until now, carbon black (CB) with high surface area and high conductivity have been widely used as fuel cell catalyst supports. However, since CB is vulnerable to durability such as carbon corrosion or oxidation, research is continuing to find materials that are durable materials. Therefore, many nanostructured materials, including carbon nanostructures, metal oxides and conductive polymers have been extensively studied over the last decades to improve the existing performance of catalyst supports for PEMFC/DMFC and to develop new ones. However, the development of supporting materials that possess high durability while reducing the amount of platinum is becoming very important, so it is not enough to develop supporting materials. Fundamental research is needed to secure catalysts with high durability through the design of catalyst supports that can solve the drawbacks. Representatively, strong catalyst-support interaction is able to improve the cell efficiency and charge mobility while reducing metal catalyst losses. In addition, the support can help improve catalyst performance and durability by reducing poisoning of the catalyst, and also affects the catalyst particle size.

In this dissertation, I present the result of solving the disadvantage by developing a new support material and identifying the relationship between support and catalyst. And also, it proposes a method to ensure durability through simple engineering of surface of support material.

To address the issues of the conventional carbon supports, chapter 2 presents carbon nano-onion (CNO), a new class of carbon allotrope, as a support for Pt catalysts. CNO had the spherical shape with 3 to 5 nm in diameter consisting of ~5 concentric graphitic layers. Superior durability of catalytic oxygen reduction reaction (ORR) was guaranteed by Pt supported by CNO (Pt/CNO) due to: (1) the *islands-by-islands* configuration of the Pt/CNO composites (c.f. *islands-on-a-particle* configuration for Pt/C) to isolate each Pt nanoparticle from its neighbors by the same-size CNO particles and to suppress Ostwald ripening by highly tortuous void structure; (2) the *curvature-induced strong interaction* between CNO and Pt; and (3) the graphite-like

concentric layers guaranteeing corrosion resistivity.

In chapter 3, an oxygen reduction reaction (ORR) catalyst/support system was designed to have Pt nanoparticles nanoconfined in nano-dimensionally limited space. Holey crumpled reduced graphene oxide plates (hCR-rGO) were used as a carbon support for Pt loading. As expected from Pt-to-Pt distance of Pt-loaded hCR-rGO longer than that of Pt/C (Pt-loaded carbon black as a practical Pt catalyst), the durability of ORR electroactivity along cycles was improved by replacing the widely used carbon black with hCR-rGO. Unexpected morphological changes of Pt were electrochemically induced during repeated ORR processes. Spherical multi-faceted Pt particles were evolved to {110}-dominant dendritic multi-pods. Nano-confinement of a limited number of Pt within a nano-dimensionally limited space was responsible for the morphological changes. The improved durability observed from Pt-loaded hCR-rGO originates from (1) dendritic pod structure of Pt exposing more number of active sites to reactants and (2) highly ORR-active Pt {110} planes dominant on surface.

Through the results of this dissertation. researchers related to fuel cell and catalyst materials will be able to summarize the results of the study on catalyst supports and hope to be a reference for future research.

Keyword: oxygen reduction reaction • platinum • carbon support • durability • carbon nano onions • holey graphene • methanol tolerance • catalyst-support interaction

# Contents

# List of figures

## Chapter 1

Pt/CNO (inset: energy dispersive spectra in b). The sizes of the CNO particles that is clearly identified as concentrically graphene-layered objects. More than 50 particles were counted.

**Figure 2.5. TEM images.** (a) Nano-diamond. (b) Vulcan XC-72R

**Figure 2.6. Pt/CNO versus Pt/CB.** (a) X-ray diffraction (XRD) patterns. (b) Raman spectra.

**Figure 2.7.** (a) *Islands on a particle* for Pt/CB. (b) *Islands by islands* for Pt/CNO. The sizes of Pt particles (orange spheres) in c and d are identical. Pt particles were drawn smaller than CNO particles for the best view to emphasize Pt particles entrapped between CNOs even if both particles are similar in size (5.3 ± 1.3 nm for CNO versus 2.8 ± 0.83 nm for Pt). (c, d) Oswald ripening or surface migration in Pt/CB (e) and Pt/CNO (f). ***d*** = particle-to-particle distance. ***l*** = pathways of dissolved ions in Ostwald ripening or atoms in surface migration.

**Figure 2.8. ORR**. Aqueous solution of 0.1 M KOH and $HClO_4$ were used as the alkaline and acid media, respectively. 10 and 20 wt. % Pt were used in Pt/CNO and Pt/CB respectively unless indicated otherwise. (a) ORR polarization in oxygen-saturated alkaline media (Figure S5 for acid media) at 10 mV $s^{-1}$ with 1600 rpm. Three different Pt amounts (10, 20 and 50 wt. % Pt) were loaded on CB while 10 wt. % Pt was loaded on CNO. (b) Corresponding Tafel plots for Pt/CNO and Pt/CB in 0.1 M KOH. (c) ORR polarization curve in oxygen-saturated acid media (Figure 2a for alkaline media) at 10 mV $s^{-1}$ with 1600 rpm.

**Figure 2.9.** Chronoamperometric responses in the alkaline media saturated by oxygen at 0.329 $V_{RHE}$ with 1600 rpm.

**Figure 2.10.** (a, b) 5000 times repeated cyclic voltammograms at 50 mV $s^{-1}$ in the acid media purged by nitrogen: Pt/CB in a and Pt/CNO in b.

**Figure 2.11.** The change in the electrochemical surface area (ECSA) of Pt/CNO and Pt/CB along voltammetric cycles**.**

**Figure 2.12. Durability.** (a to d) TEM images (inset = size distribution) of Pt/CB (a, b) and Pt/CNO (c, d) before durability test (a, c) and after durability test (b, d). (e) X-ray photoelectron Pt 4f spectra of Pt/CB and Pt/CNO before and after durability test. The accelerated durability tests (ADT) were performed by sweeping potential between -0.1 $V_{RHE}$ and 1.2 $V_{RHE}$ for 5000

cycles. Nitrogen-saturated 0.1M $HClO_4$ solution was used as the electrolyte. (f) Pt L3-edge XANES spectra by a synchrotron light source

**Figure 2.13. Pt-support interaction.** (a) Adsorption energy ($\Delta E_{ads}^{Pt}$), the amount of atomic charge transfer ($\Delta q$) and Fermi level change ($\Delta E_F$) of Pt nanoparticles on carbon supports. Density function theory (DFT) was used. $Pt_7$ was used for representing Pt nanoparticles while $sp^2$ carbon nanoribbons of zigzag or armchair structures were modelled for the carbon supports. Flat facet and edge represented the low-curvature Vulcan XC-72R (CB) while curved facet was used for describing the high-curvature CNO. (b and c) The optimized structures of a $Pt_7$ cluster adsorbed on flat and curved $sp^2$ carbon nanoribbons. $Pt_7$ nanoparticles on zigzag and armchair nanoribbons (ZZNR and ACNR) were shown in b and c, respectively. The curved nanoribbons were made by curving the corresponding flat nanoribbons along the x-axis. The structures were viewed from the y-axis.

**Figure 2.14**. The schematic representation of the effect of curvature on the adsorption affinity. (A) Planar graphitic carbon system. (B) Curved graphitic carbon system.

**Figure 2.15.** The optimized structure of carbon nanoribbons. Top views of (a) ZZNR, (b) c-ZZNR, (c) ACNR and (d) c-ACNR, and side views of (e) c-ZZNR and (f) c-ACNR. Note that in (a) and (c) the orange colored atoms were fixed to reduce the distortion of $sp^2$ carbon nanoribbons during the $Pt_7$ adsorption on the other edge. Gray and white spheres indicate carbon and hydrogen atoms, respectively. The orange triangles indicate the adsorption sites for the $Pt_7$ nanoparticle.

**Figure 2.16.** The optimized structure of $Pt_7$ nanoparticle. Pt atoms were colored navy and the triangular facet, which is the adsorption site of the nanoparticle, was colored orange.

**Figure 2.17.** Density of states (DOS) of $Pt_7$ in adsorbed (Pt-a) and deformed (Pt-d) states. The deformed states were synthesized by removing nanoribbons from $Pt_7$-adsorbed states. (a) ZZNR. (b) c-ZZNR. (c) ACNR. (d) c-ACNR. The dashed lines indicate the Fermi levels ($E_F$) of the states of $Pt_7$. $\Delta E_F$ is difference of Fermi energies between adsorbed and deformed states. $\Delta q$ is the amount of atomic charge transfer from $sp^2$ carbon nanoribbon to $Pt_7$.

**Figure 2.18.** The optimized structure of adsorbed $Pt_7$ nanoparticle on (a) ZZNR facet, (b) ACNR facet, (c) ZZNR edge, (d) ACNR edge, (e) c-ZZNR facet and (f) c-ACNR facet. $\Delta E_{ads}^{Pt}$ is the adsorption energy of $Pt_7$ nanoparticle and $\Delta q$ is the amount of atomic charge transfer from $sp^2$

# List of tables

# Nomenclature

| | |
|---|---|
| **A-CNO** | Arc-discharge-driven carbon nano onion |
| **ACNR** | Armchair nanoribbon |
| ***b*** | Tafel slope |
| **c-ACNR** | Curved armchair nanoribbon |
| **CB** | Carbon black |
| **CNF** | Carbon nanofiber |
| **CNO** | Carbon nano onion |
| **CNT** | Carbon nanotube |
| **CR** | Crumpled |
| **CVD** | Chemical vapor deposition |
| **c-ZZNR** | Curved zigzag nanoribbon |
| **D** | Disorder band of carbon structure in Raman spectroscopy |
| **D*** | Disordered graphitic lattice by $sp^2$-$sp^3$ bonds in Raman spectroscopy |
| **D"** | Amorphous carbon structure of carbon structure in Raman spectroscopy |
| **DFT** | Density function theory |
| **DOS** | Density of states |
| **ECSA** | Electrochemical active surface area |
| **FCEV** | Fuel cell electric vehicle |
| **RRDE** | Rotating ring disk electrode |
| **FL** | Flat |
| **FT-IR** | Fourier transform infrared spectroscopy |
| **G** | Graphite structure of carbon in Raman spectroscopy |
| **GO** | Graphene oxide |
| **hCR** | Holey crumpled |
| **HER** | Hydrogen evolution reaction |
| **HOR** | Hydrogen oxidation reaction |
| ***i*** | Current density |
| $i_0$ | Exchange current |
| $Q_H$ | The charge for the hydrogen adsorption |
| ***L*** | The weight of the Pt loading |
| $q_H$ | The charge required for monolayer adsorption of hydrogen on a Pt surface |
| $\kappa$ | Conductivities |
| ***RHE*** | Reversible hydrogen electrode |
| $L_c$ | [002] direction of carbon |
| $i_b$ | Backward scan of the peak current of $CO_{ads}$ oxidation |
| $L_a$ | [100] direction of carbon |
| **XANES** | X-ray absorption near edge structure |
| $i_d$ | Disk current |
| $i_f$ | forward scan of the peak current of methanol oxidation reaction |
| $i_r$ | Ring current |
| **LSV** | Linear sweep voltammetry |
| **MEA** | Membrane electrode assembly |
| **MeOH** | Methanol |

| | |
|---|---|
| **MOR** | Methanol oxidation reaction |
| **MWCNT** | Multiwall carbon nanotubes |
| ***N*** | Collection efficiency |
| **N-CNO** | Nanodiamond-driven carbon nano onion |
| **OER** | Oxygen evolution reaction |
| **OHNC** | Ordered hierarchical nanostructured carbon |
| **ORR** | Oxygen reduction reaction |
| **PAL** | Pohang accelerator laboratory |
| **PEMFC** | Proton exchange (or polymer electrolyte) membrane fuel cell |
| **Pt/C** | Platinum nanoparticles supported by carbon |
| **Pt/CR-rGO** | Platinum loaded crumpled reduced graphene oxide |
| **Pt/FL-rGO** | Platinum loaded reduced graphene oxide |
| **Pt/hCR-rGO** | Platinum loaded Holey crumpled reduced graphene oxide |
| **SEM** | Scanning electron microscopy |
| **TEM** | Transmission electron microscopy |
| **TGA** | Thermogravimetric analysis |
| **XAFS** | X-ray absorption fine spectra |
| **XPS** | X-ray photoelectron spectroscopy |
| **ZZNR** | Zigzag nanoribbon |
| $\Delta E_{ads}^{MeOH}$ | The methanol adsorption energy |
| $\Delta E_{ads}^{O2}$ | Adsorption energy of oxygen on $Pt_7$ |
| $\Delta E_{ads}^{Pt}$ | The adsorption energy of $Pt_7$ on $sp^2$ carbon nanoribbons |
| $\Delta E_F$ | Fermi level change |
| $\Delta q$ | The amount of atomic charge transfer |
| $\eta$ | Overpotential |

# Chapter 1: General Introduction

## 1.1. The important of electrocatalyst

Polymer electrolyte membrane fuel cells (PEMFCs) are power generation devices that produce electricity using hydrogen and oxygen as fuel. They do not emit pollutants such as $CO_2$ and $NO_x$, which are the main causes of air pollution. As a power generation device, it receives much attention. Fuel cell technology is based on the generation of energy when hydrogen fuel is converted to water through an electrochemical reaction. The principle of the fuel cell is as follows (**Figure 1.1a**). Hydrogen injected into the oxidation electrode (anode) is separated into hydrogen ions ($H^+$) and electrons ($e^-$), and oxygen ions and electrons are separated from the air injected from the reduction electrode (air electrode). At this time, electricity is generated by the movement of the separated electrons, and hydrogen and oxygen are generated, and water is generated to generate heat.[1] Electricity generation efficiency is 30 ~ 40% and thermal efficiency is 40% or more, which is 70 ~ 80% high efficiency.

$$\text{Anode: } H_2 \rightarrow 2H^+ + 2e^- \quad (1)$$

$$\text{Cathode: } 1/2O_2 + 2H^+ + 2e\text{-} \rightarrow H_2O \quad (2)$$

The reaction efficiency of the fuel cell depends on how well the oxygen reduction reaction (ORR) occurs in the reducing electrode since there is an energy wall during the reaction process, a catalyst is required to increase the reaction efficiency. Platinum catalysts are mainly used. The reason for this is that the reaction rate is relatively slow compared to the hydrogen oxidation reaction at the oxidizing electrode, and thus serves as a step of determining the overall reaction rate of the fuel cell. The main reason for the slow rate of ORR is that the ORR progresses through several stages of reaction and exist a step of high energy wall. Since the energy wall depends on how strongly the oxygen is adsorbed during the oxygen adsorption step in the ORR step, the oxygen adsorption strength is an important parameter for determining the efficiency of the ORR.[2] Platinum catalysts have been proven to excel in their catalytic effects through many years of research, but they are still difficult to commercialize due to their high cost. As shown in the **figure 1.1b**, the most expensive fuel cell component is the electrode, which is composed of many catalyst layers. Platinum nanoparticles supported by carbon (Pt/C) have been the most popular catalysts for cathodes of fuel cells in terms of this reason. Because, it is possible to obtain a small size of particles and a large efficiency after synthesizing them on a support.

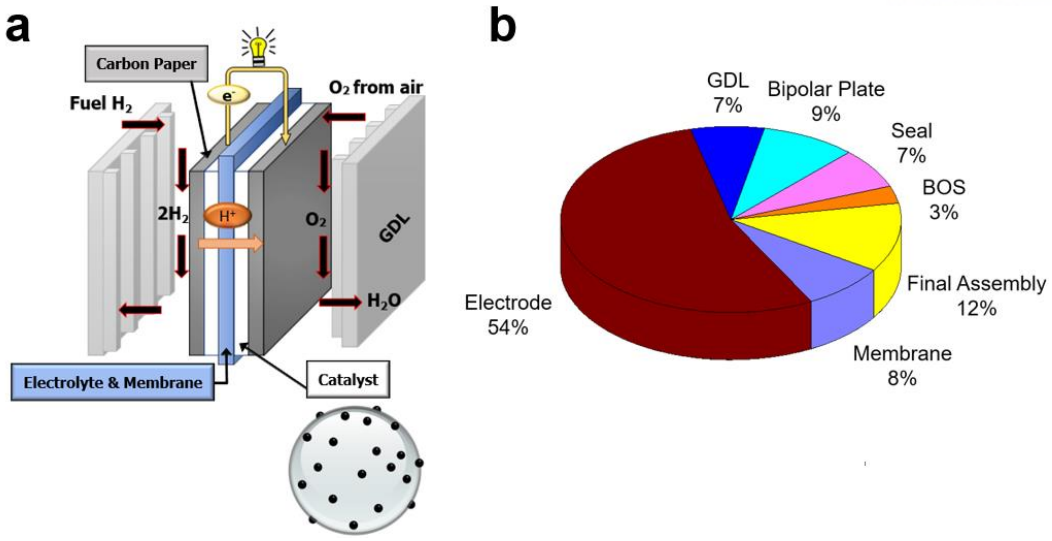


**Figure 1.1. Components of polymer electrolyte membrane fuel cell.** (a) The working principle of PEMFC. (b) The price distribution of fuel cell components (the data result from 2014 annual merit review and peer evaluation meeting in Department of Energy).

As mentioned above, Pt has been considered as the electrocatalyst exhibiting the highest electroactivity of oxygen reduction reaction (ORR) that is the cathodic process of fuel cells.[3] (**Figure 1.2**). In order to the ORR performance, the characteristics of the new catalyst are to induce the oxygen adsorption strength to be about 0.2 ~ 0.4 eV weaker than platinum.[4] This is because the oxygen atom, the intermediate product of ORR, helps to facilitate conversion to other intermediates. The oxygen adsorption strength depends on the geometry of the catalyst. In particular, the oxygen adsorption strength can be controlled by increasing or decreasing the interatomic spacing.[5] Therefore, if the optimum oxygen adsorption strength to improve the performance of the ORR is searched and the catalyst structure is optimized to cause such an oxygen adsorption reaction, the efficiency of the fuel cell can be improved.

In spite of its superior intrinsic activity, Pt nanoparticles (practically around 5 nm) supported by carbon (Pt/C) suffers from unsatisfied durability for practical fuel cell operations. I am going to discuss the reason in the next section.

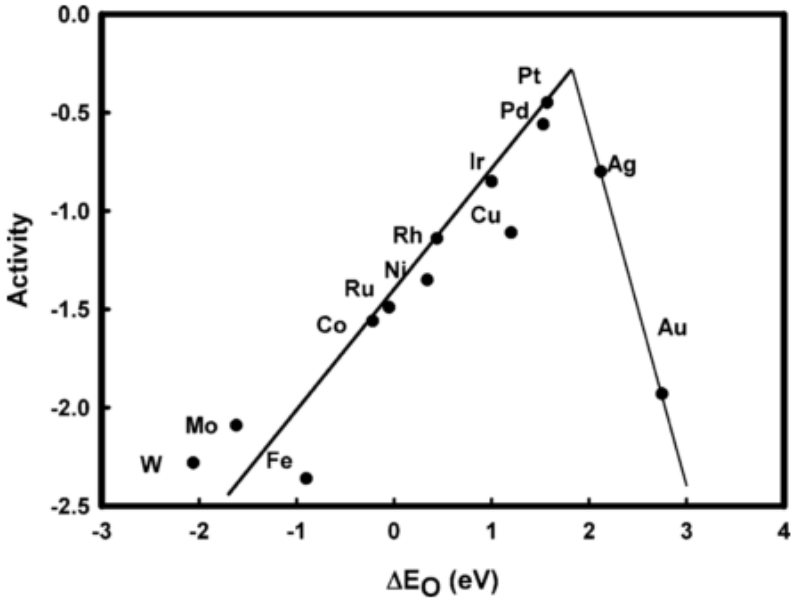


**Figure 1.2.** Trend in oxygen reduction activity plotted as a function of the oxygen binding energy from ref. 3.

### 1.2. The drawback of platinum nanoparticles supported by carbon

Generally, the automotive fuel cell stack experiences repeated start-up and shut-down (Strat-up / Shut-down). At this time, the fuel cell electrode is inevitably exposed to a high potential region. Carbon, which is used as a MEA catalyst carrier, is subjected to sustained oxidative damage in this potential region. The carbon used is often thermodynamically unstable under the operating conditions of the PEMFC and can be corroded as shown in the following equations (3) and (4).

$$C + 2H_2O \rightarrow CO_2 + 4H^+ + 4e^- \text{ (0.207 V vs. SHE)} \qquad (3)$$

$$C + 2H_2O \rightarrow CO + 2H^+ + 2e^- \text{ (0.518 V vs. SHE)} \qquad (4)$$

Carbon oxidation reactions of the above equation slowly proceed in general condition. But, the progress is going along more rapidly under high voltage conditions such as start/stop. The weakened interaction between the Pt particles and the carbon support due to carbon corrosion causes the platinum particles to detach from the support.[6,7]

In addition, in the normal operation range of the fuel cell, the platinum supported by c arbon electrocatalyst has a problem that the active surface area of the catalyst decreases due to the Ostwald-ripening and the particle migration on the carbon surface due to the dissolution-

redeposition, and as a result, the catalyst performance deteriorates. It is known that platinum dissolution is severe in smaller particles than in bulk platinum. This is because the surface energy is large that it is already dissolved at a lower potential (Gibbs Thompson effect).[8] The particle growth can occur when dissolved platinum is reprecipitated to other larger platinum particles. This decomposition mechanism is called Ostwald-ripening. And also, A possible explanation for the growth of platinum particles is the collision between the platinum particles on the surface of the carbon support.[9] The platinum particles come into contact with each other by continuous adhesion and contraction caused by carbon corrosion. In a nutshell, carbon corrosion is a primary process, which creates a secondary problem of platinum particle detachment and agglomeration. Platinum dissolution can also be regarded as another fundamental degradation process that produces a second decomposition process called platinum deposition and Oswald ripening.

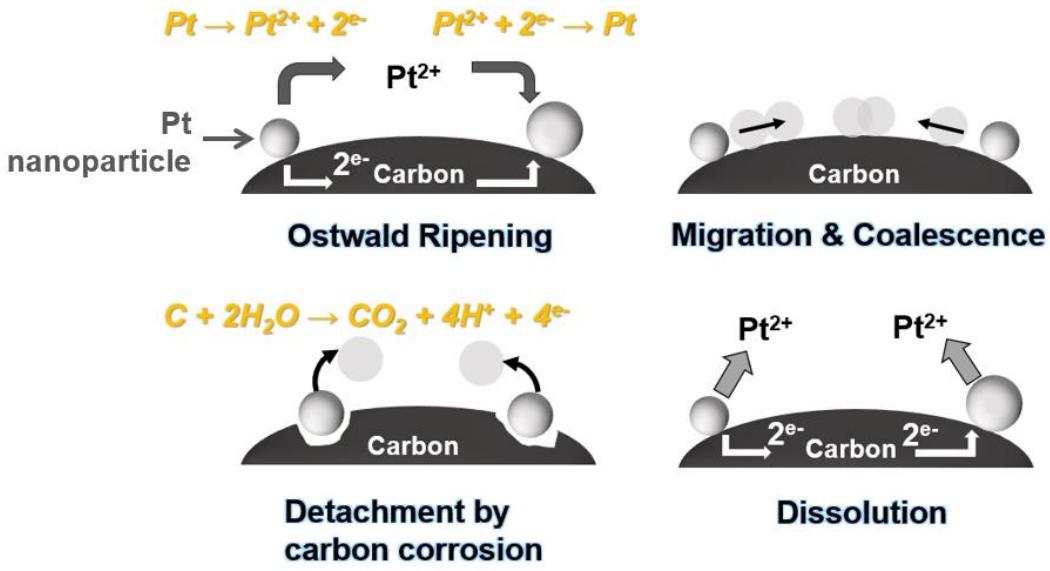


**Figure 1.3.** Simplified representation of degradation mechanisms for platinum supported by carbon (Pt/C)

### 1.3. The improvement of durability method

Even in the normal operation region of the fuel cell, the fuel cell catalyst has a problem that the effective surface area of the catalyst is reduced due to Ostwald-ripening and migration due to dissolution-redeposition, and as a result, the catalyst performance is deteriorate. To solve these problems, studies for improving the durability of catalyst and electrodes have been progressing actively. In this section, I present some representative methods that have been reported to improve durability. One of the solutions is the application of OER (oxygen evolution reaction) active materials.[10,11] The OER catalyst is a catalyst that generates oxygen by decomposing water. When OER active materials (Ru, Ir, $RuO_2$, $IrO_2$, etc.) are present in the fuel

cell electrode, the water is first decomposed before the catalyst is corroded by the high potential at start-up/start-down condition. So, it can be prevented carbon corrosion.

Ruthenium, the most widely known OER catalyst, shows a phenomenon of leaching due to vulnerability to acidic atmosphere, which is a fuel cell condition. Also, it is not suitable to commercial fuel cell vehicle system because of high cost. For this reason, recent studies use iridium, a material that has OER activity but is relatively inexpensive and does not dissolve in an acidic atmosphere. Nevertheless, there is a problem in applying an OER catalyst such as iridium metal to a catalyst electrode in fuel cell system. Due to the crystallinity of the surface, it is difficult to uniformly disperse in the slurry, and due to the aggregation of metals, the catalytic active site is blocked to deteriorate the electrode structure, resulting in deterioration in performance due to the materials. To solve this problem, iridium was alloyed with the platinum as ORR active material. The synthesis of platinum iridium alloy (PtIr/C) has been tried with various studies such as sol-gel method, vapor deposition, and electroplating method. However, there has been a problem that the uniformity is low and it is not suitable for mass production application. Ultimately, the PtIr/C catalyst synthesized on the carbon support surface needs to have better initial performance than the existing MEA using the platinum supported catalyst. In addition, there is a need for research that can improve the durability of the vehicle simulation system. Above all, iridium is also an expensive metal, so the price cut remains a problem. In order to solve this problem, researches for making alloys using nickel, iron and the like have recently become popular.

Another method for ensuring durability is to inhibit the dissolution and size increase of the metal ions described in the above section by keeping the metal catalyst in the support. The Mayrhofer group which has been studying the catalyst durability studies for a long time reported hollow graphitic spheres (HGS) such as a mesostructured graphitic carbon support with a high surface area (1000 $m^2g^{-1}$) and precisely controlled pore structure.[12] From this structure, that was developed to overcome the catalyst degradation during the long-term condition while still sustaining high activity. As shown in **Figure 1.4**, the size of the Pt nanoparticles does not show a significant change despite the substantial morphological changes caused by potential repetition during operation by limiting the platinum catalyst in the pores. Therefore, it can be seen that the decomposition of the fuel cell due to the separation of the particles and the aggregation of the particles is remarkably suppressed.

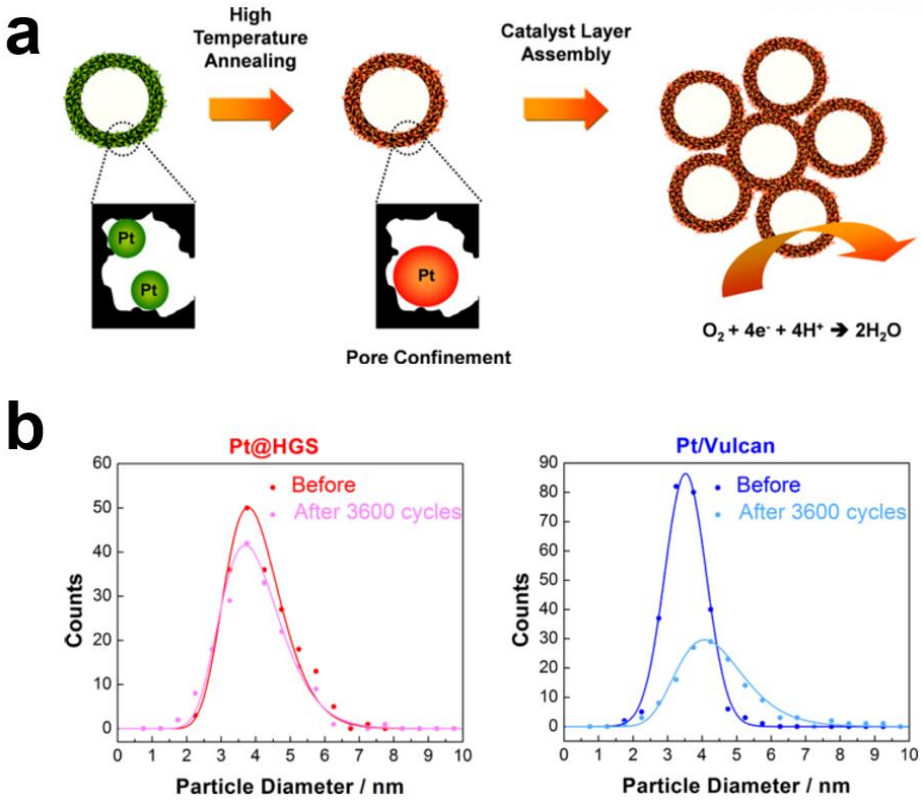


**Figure 1.4. Schematic model of Pt encapsulation by pore confinement and particle size distribution.** (a) Pre-synthesized HGS is impregnated with a Pt salt precursor under ultrasonication. After a reduction step under 30% $H_2$ in argon at 250 °C, Pt nanoparticles smaller than 2 nm are formed. A high temperature annealing step up to 900 °C leads to the growth and subsequent confinement of Pt nanoparticles of ca. 3−4 nm in the mesoporous structure of the HGS. (b) Pt@HGS catalyst (left) and Pt/Vulcan reference catalyst (right) before and after 3600 degradation cycles between 0.4 and 1.4 $V_{RHE}$ with a scan rate of 1 V $s^{-1}$ in argon saturated 0.1 M $HClO_4$ from ref. 12.

And also, Mayrhofer's group has successfully synthesized 3-4 nm diameter Pt alloy nanocatalyst with a narrow size distribution by space-confined alloying of Pt-Ni nanoparticles on a mesoporous support (PtNi @ HGS).[13,14] PtNi @ HGS reported that the mass activity was tripled compared to conventional catalysts, resulting in a 3-fold reduction in the required Pt mass and thus cost savings. Also, the Ni content of the activated catalyst remained almost unchanged after the weak aging, and the pores were not separated or aggregated due to pore confinement. Thus, the improved activity is expected to be a promising candidate for PEM fuel cells after being aged within the operating range of the ORR catalyst. (**Figure 1.5**)

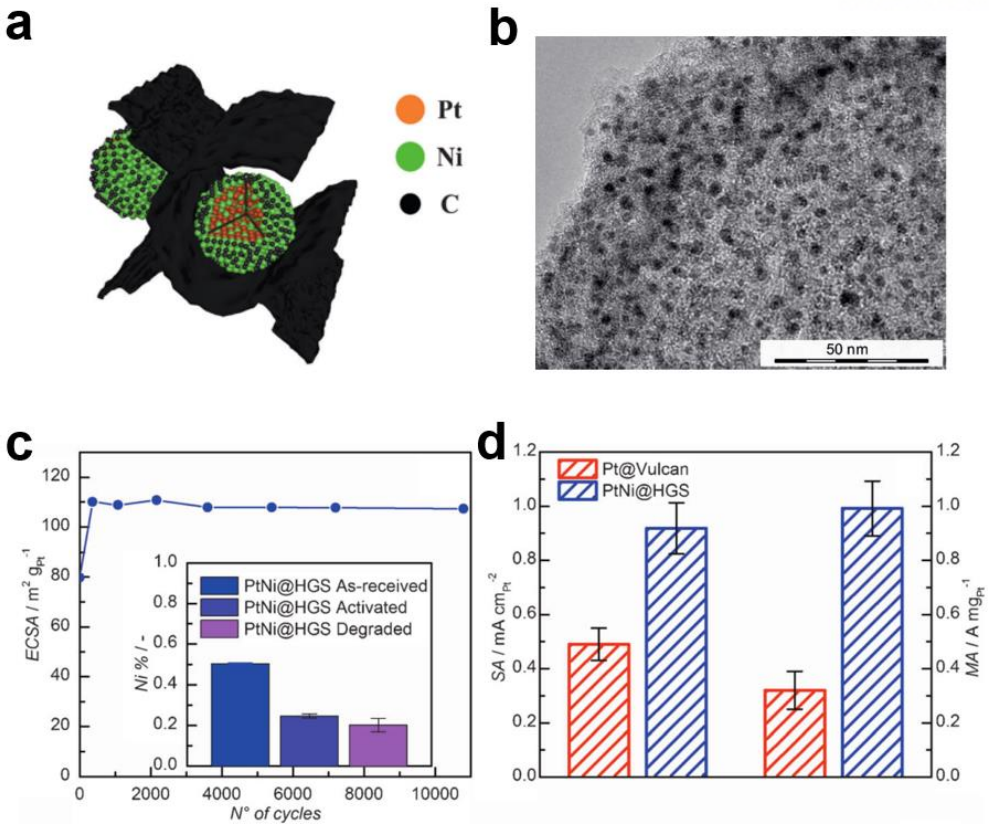


**Figure 1.5. Structural study and assessment of the electrochemical stability of PtNi@HGS.** (a) 3D structural model of PtNi@HGS after annealing with the metal nanoparticles confined inside the carbon matrix. (b) TEM image of PtNi@HGS. (c) evolution of the ECSA over time and Ni ratio for the as-received, activated, and aged catalyst. (d) specific activity (left axis) and mass activity (right axis) of PtNi@HGS and a standard Pt/Vulcan at 0.9 $V_{RHE}$ from ref. 13.

Another method for securing the durability of existing commercial catalysts is to control the size or shape of the metal catalyst or to coat the metal catalyst with thin carbon such as graphene. Both these methods and described above methods have improved durability through changes in the metal catalyst. However, such a novel metal catalyst also composes a complex with a carbon support. Although research and development of metal catalysts are also important, research on carbon supports for durability and research on the relationship between carbon supports and metal catalysts are also important. In the following section, I am going to discuss the importance and types of carbon supports for improving catalyst durability.

### 1.4. The factor of carbon support

It is important to select the support that is suitable for the support. Above all, it is necessary to have a large specific surface area because platinum particles must be evenly distributed. It is preferable that the material has a size of at least 100 - 300 $m^2/g$ and preferably has a value of 400 - 1000 $m^2/g$ or more. In terms of porosity of carbon, carbon material of mesoporous structure is preferred. 10-100 nm pore size is preferred as carbon support material. The basic fuel cell operates in an acidic atmosphere. Therefore, carbon support having high durability even in acidic conditions is a necessary condition. This is an important factor affecting impurity formation and proton conductor poisoning. The most important factor that a carbon support should have is its strong corrosion resistance in electrochemical conditions. It depends on the degree of carbonization and can be improved by heat treatment at high temperatures or surface modification. However, the degree of high carbonization reduces initial catalytic performance by reducing the distribution of platinum catalysts. On the other hand, carbon having a low carbonization degree is easily oxidized, making it difficult to produce a catalyst having high durability. The relationship between the structure and the characteristics of the carbon support according to the degree of carbonization is shown in the **figure1.6**.

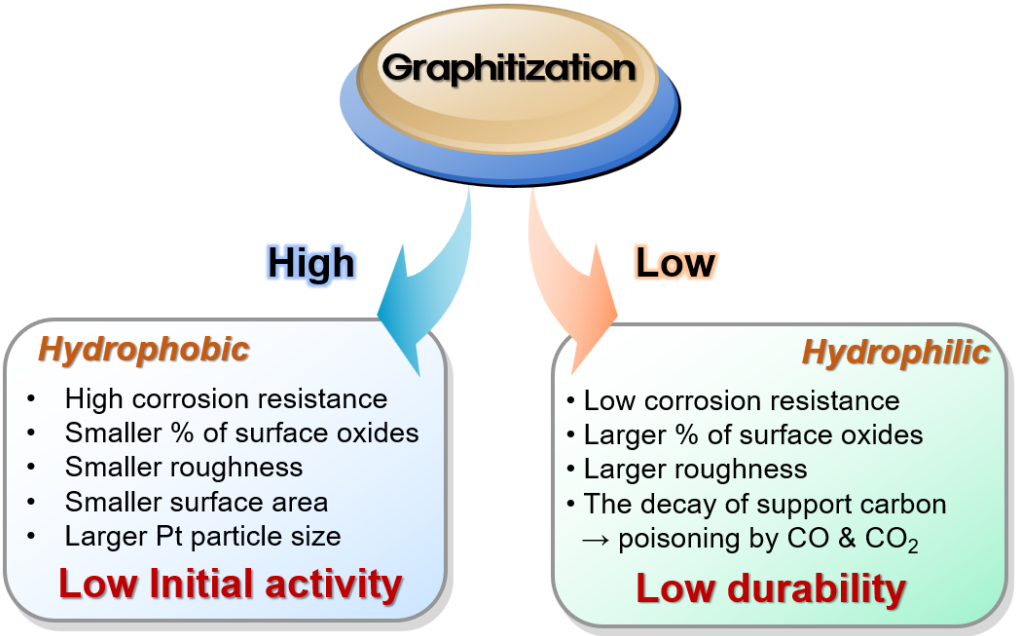


**Figure 1.6.** Relationship between structure and properties of carbon supports by carbonization

Catalyst-support interaction has been considered as one of the important factor to affect catalytic activities and stability of classical *chemo*-catalysts. Recently, the catalyst-support interaction was revisited as the important factor to affect catalytic activities and stability.[15,16] In

**figure 1.7** indicate the electronic and physical interactions are the two aspects of the catalyst support interaction. Support materials could donate or accept electrons to or from catalysts, changing the electronic structure of catalysts and moreover their electroactivities. Physical interaction is based on the binding force defining the adhesion strength of catalyst molecules or elements to the surface of support materials. For example, when physical catalyst-support interaction is strong, the catalyst is bound to the support strongly. Dissolution and surface migration of Pt are suppressed with catalyst stability increasing.

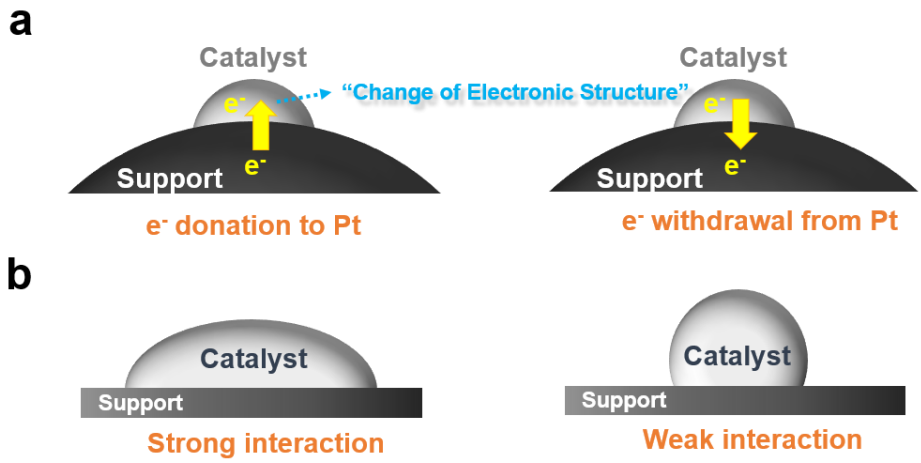


**Figure 1.7.** The relationship of catalyst support interaction. (a) Electronic interaction. (b) Physical interaction.

## 1.5. The kind of carbon support materials

### *1.5.1. Commonly used carbon black*

As mentioned in 1.3, the material that is commonly used while satisfying the elements that the platinum support should have are Vulcan XC-72R, Shawinigan Acetylene Black and Black Pearl 2000. And also, E-Tek, Johnson-Matthey, and Tanaka sell 10 to 60 wt.% Pt/C or Pt based alloy/C, and non-supported catalysts are also commercially available. In general, it still has organic-sulfur impurities. And, it has problems such as nanopores that trap catalyst nanoparticles, thereby reducing the activity of the reactants by making them inaccessible to the catalyst particles. Above all thing, CB has the big disadvantage of being easily oxidized at high voltage and reducing durability. In order to secure this problem, a method of increasing the crystallinity of carbon by using Vulcite which is heat-treated at high temperature of Vulcan XC-72R to secure durability is also commonly used. **Figure 1.8** shows the structural change of the Vulcan XC-72R before and after the heat treatment.

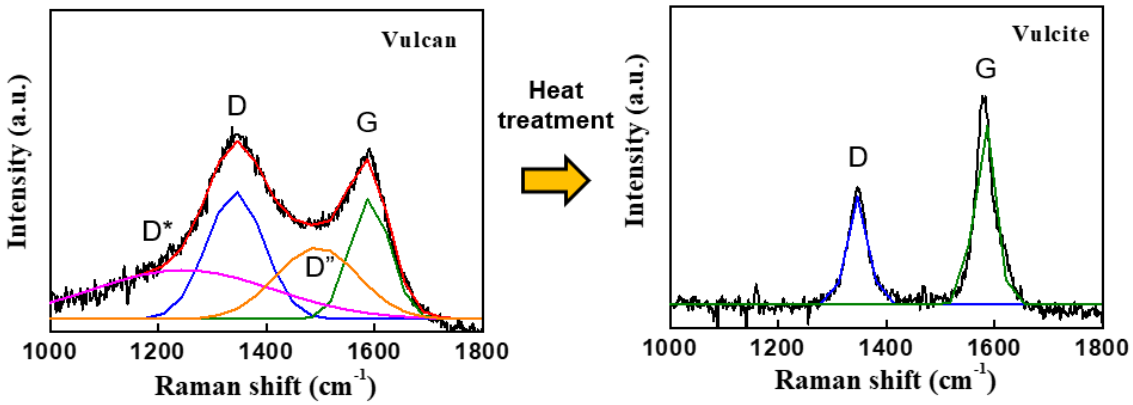


**Figure 1.8. Vulcan versus Vulcite.** The two main bands are the D (defect) band and the G (Graphite) band. Additional bands are attributed to (i)amorphous carbon D", (ii) $sp^3$ carbon band or disordered graphitic lattice by $sp^2$-$sp^3$ bonds at the edges of networks (D*)

Recently, carbon allotrope that can replace existing carbon black (CB) have been studied. These materials are shown in a simple table before being explained.

| Support material | Pros | Cons | Note |
|---|---|---|---|
| CNT 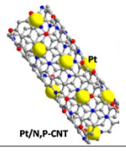  | • Appropriate surface area<br>• High conductivity<br>• Good stability | • Poor dispersion of Pt<br>• Poor pore of electrode → limited movement of gas, water | Toyota – Pt/CNT |
| MC 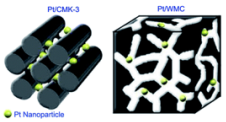  | • Large surface area<br>• Good dispersion of Pt<br>• Good conductivity<br>• Good adsorption of electrolyte by Capillarity | • Expensive than other carbon<br>• Complex manufacturing process | |
| Graphene 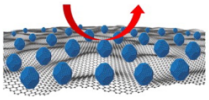 | • Large surface area<br>• High conductivity<br>• Mass production<br>• Good dispersion in variety solvent | • Amorphous carbon & oxygen functional group from oxidation process with strong acid | |
| CNF 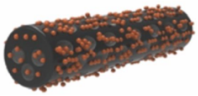 | • High graphitization<br>• Easy process<br>• Easy control of pore and surface area | • Carbon coating problem → Selective removal of carbon on metal catalyst | |

**Table 1.1.** Various kinds of Pt supported carbon materials.

*1.5.2. Carbon nanotubes*

Carbon nanotubes (CNTs) are synthesized by using metal catalyst particles such as iron, copper, and nickel. Therefore, they can be synthesized at a relatively low temperature as compared with conventional carbon materials. And CNT has a high electrical conductivity, good crystallinity and high surface area. CNTs are very close to commercialization as a fuel cell electrode support. Toyota, Japan's leading company in the fuel cell automobile market, is developing new catalyst and membrane electrode assembly (MEA) based on highly crystalline CNTs for durability improvement. Murata et. al. has developed a technique to uniformly disperse the Pt nanoparticles in a multiwall CNT with a surface area of 200 $m^2$ $g^{-1}$ similar to the surface area of conventional carbon black (**Figure 1.9**).[17] In addition, the CNT-based Pt catalyst exhibited higher performance, Pt utilization and long-term stability than the conventional carbon black. Based on these results, Toyota has selected multiwalled carbon nanotubes as a next-generation catalyst support for fuel cells and continues to carry out related research. However, carbon nanotubes have a problem that it is difficult to uniformly carry platinum particles by a general catalyst production method due to low curvature and chemical stability. CNTs have a high packing density. This being so, the pores of the electrodes are not developed when CNT based catalyst are used to fabricate MEA. As a result, there is a problem that the movement of water which is a product and a gas required for a fuel cell reaction is limited. Many researchers have been working on solving these problems and developing a surface treatment technique using a surfactant or strong acid to control the crystallinity of carbon nanotubes. However, these approaches are also

disadvantageous in that the durability of the carbon support is deteriorated It is difficult to solve the problem. Therefore, in order to develop a highly durable catalyst based on a carbon nanotube, it is necessary to develop a non-destructive surface treatment technique and a catalyst synthesis technique capable of maintaining the characteristics of carbon nanotubes having high crystallinity and uniformly supporting platinum particles.

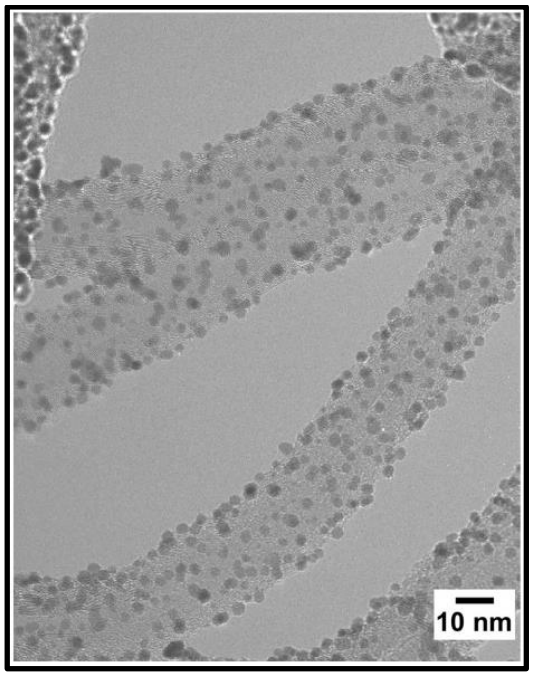


**Figure 1.9.** TEM image of Pt nanoparticles on CNTs from ref. 17.

*1.5.3. Carbon nanofiber*

Carbon nanofibers (CNFs) are in the form of fibers having a diameter of several tens to one hundred nanometers. Polymers are mainly used as raw materials for producing carbon nanofibers. Generally, CNFs produce polymer fibers by using polymer solution and electrospinning method and induce stabilization reaction to maintain fiber shape at high temperature. CNFs have a high crystallinity due to high temperature heat treatment and are easy to composite with metals catalyst in the manufacturing process. And, it is easy to control the fine pores and surface area. The electrospinning method is advantageous in that a polymer solution can be prepared singly or mixed with a metal precursor solution to produce a polymer fiber. Particularly, the polymer fiber produced by using the mixed solution is able to synthesize a mixed catalyst with CNFs and metal precursor. After carbonization process, the metal precursor present in the polymer fibers is reduced at high temperatures to form metal particles. It is possible to produce catalyst particles having a relatively small size even in a high-temperature heat treatment because they are limited by growth or migration by the surrounding molecules or carbon

surrounding the metal particles. **Figure 1.10** compared the long-term stability of Pt/CNFs prepared by electrospinning with commercial Pt/C. Carbon nanofibers prepared by high temperature heat treatment have high crystallinity. Therefore, it shows corrosion resistance and suppresses the agglomeration of Pt particles due to the carbon coating on Pt particles, thus exhibiting a long-term stability higher than that of the commercial Pt/C.[18] However, metal particles present inside the carbon nanofibers do not participate in the electrochemical reaction. As a result, there is a problem that activity per mass is decreased. Therefore, a technique must be developed that can easily transfer the metal particles to the surface of the carbon nanofibers or maximize the exposure of the metal particles with the crystallinity of the CNFs.

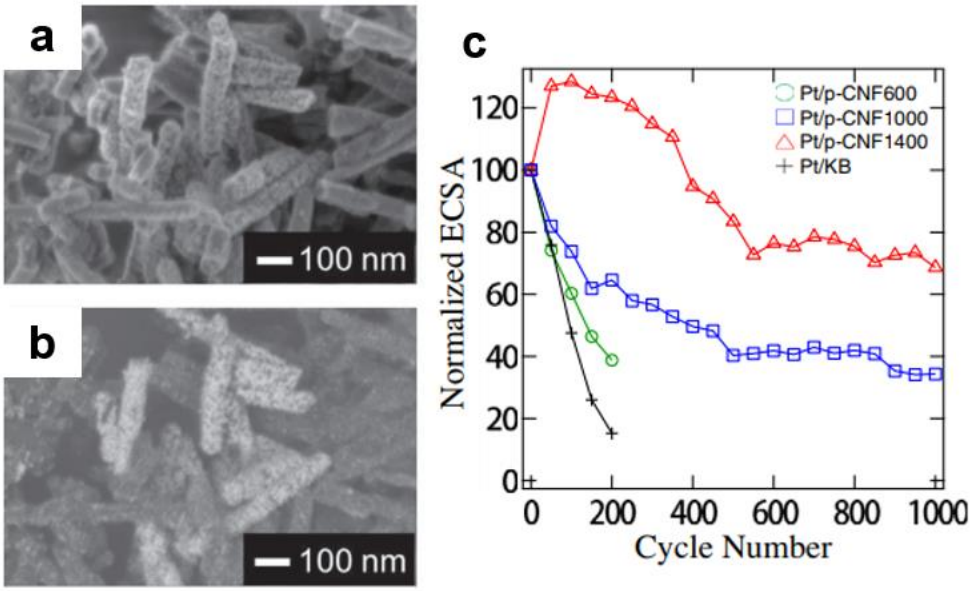


**Figure 1.10.** (a,b) SEM image of Pt/carbon nanofiber electrocatalyst. (c) Change of ECSA of the e Pt/p-CNF600, Pt/p-CNF1000, Pt/pCNF1400, and Pt/KB during the accelerated durability test for 200 and 1000 cycles from ref. 18.

*1.5.4. Graphene*

Graphene is a two-dimensional carbon material with carbon bonded in a hexagonal honeycomb structure. Graphene has a high specific surface area (2600 $m^2g^{-1}$), electrical conductivity (200,000 $cm^3V^{-1}•s^{-1}$, light transmittance (about 98%), and excellent chemical stability, so much research is being done as a next generation carbon support. The manufacturing method of graphene can be roughly divided into a growth method and a peeling method. The growth method is chemical vapor deposition (CVD) in which a gas containing a carbon atom such as methane is injected into the surface of a metal similar to the growth of carbon nanotubes. There

is an epitaxial growth method in which carbon-containing substrates such as silicon carbide (SiC) are grown by high temperature heat treatment. Among various methods, the material that can be used as a fuel cell catalyst support is an oxide graphene oxide (GO) produced by a chemical stripping method which is easy to mass-synthesize and chemically modify and can be prepared in powder form. GO can easily control the oxygen function of the graphene surface using a reducing agent to suit the application. Such graphene is called reduced graphene oxide. Chemically stripped graphene has the advantage of a large specific surface area and uniform dispersion in various solutions. As a result, it has been reported that platinum particles are uniformly supported on the surface of graphene and thus the performance of the fuel cell catalyst is high. In particular, studies on improving the durability of graphene-based catalysts have focused on enhancing the durability of graphene itself by doping the graphene oxide with a different element such as nitrogen, boron, sulfur. **Figure 1.11b** shows the stability of the fuel cell after the growth of nitrogen-doped graphene with platinum nanotubes. Nitrogen-doped graphene has higher bonding strength between platinum and carbon support than pure graphene and conventional carbon materials, and it can improve long-term stability by suppressing aggregation of platinum particles due to bending on the surface of graphene.[19]

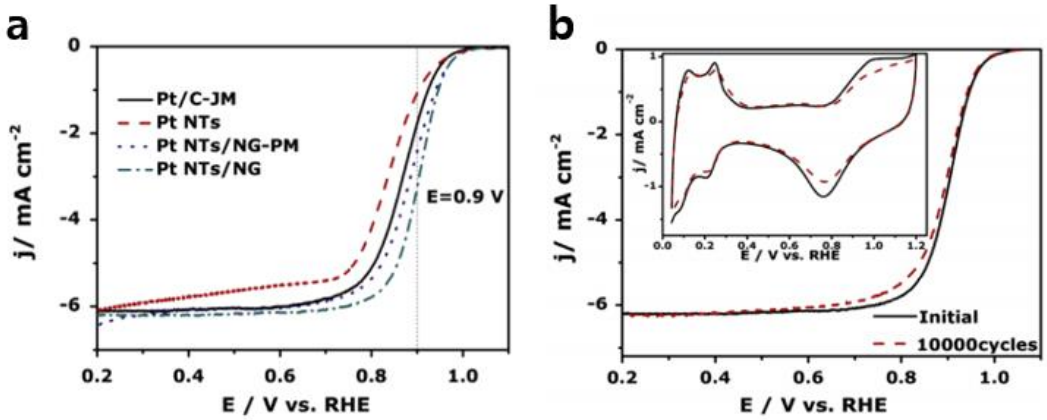


**Figure 1.11.** (a) The ORR polarization curves of the Pt nanotube/n-doped graphene (Pt NTs/NG; green) catalysts in 0.1 M $HClO_4$. (b) Before and after 10,000 cycles durability testing of Pt NTs/NG catalysts. The insets are the CVs of each catalyst in $N_2$-saturated 0.1 M $HClO_4$ solutions before and after degradation tests from ref. 19.

However, the GO is produced through an oxidation process under a strong acid condition in order to minimize the Van deer Waals Force between the graphene layers. As a result, there are various oxygen functional groups and amorphous carbon materials on the surface of graphene. Oxygen functionalities and amorphous carbon will serve as a starting point for long-term corrosion of the carbon support in the form of carbon monoxide or carbon dioxide. Therefore, it

is necessary to develop a surface graphene oxide graphene and a technique capable of easily controlling amorphous carbon.

*1.5.5. Mesoporous carbon*

Mesoporous carbon is a carbon material with regular and constant size pores. It has a relatively high specific surface area and electrical conductivity. Generally, mesoporous carbon is produced by using a pore structure of a template such as mesoporous silica. After the raw material of carbon material is put into the template, the template is selectively removed after heat treatment at a high temperature to remove the mesoporous carbon. Mesoporous carbon is easy to control the size, density, and shape of pores according to the type and amount of template, so it is easy to design optimal condition as electrochemical electrode. However, the manufacturing process is complicated, and the price is higher than other carbon materials. Mesoporous carbon is known to exhibit relatively good stability compared to other carbon materials under fuel cell operating conditions. Particularly, in the case of mesoporous carbon having selectively micropores even under an electrolyte poor operating condition, the capillary phenomenon causes the electrolyte to be absorbed more quickly than the carbon black in the initial state, it is known to remain in the pores and to be effective in preventing the electrode from drying or corroding.[20] In order to widely utilize the mesoporous carbon material having these advantages as a support for a fuel cell electrode catalyst, it is necessary to develop a technology capable of mass production in addition to cost reduction of the material.

*1.5.6. Carbon nano onion*

Carbon nano-onions (CNOs) are an emerging, novel class of carbon materials. CNO is 0-D carbon analogue of 1-D CNT and 2-D graphene. CNO is composed of $sp^2$-bonded, concentric carbon shell surrounding a hollow core.[21-25] The curved morphology of CNO loosens the conjugation along the graphene sheet and result in the change in electronic structure and the band-gap. This unique structure of CNO will have a significant effect on the physicochemical, electronic, and electrochemical property and reactivity. Besides the structure, structural order and surface chemistry are also important factors to influence the properties. Due to several unique and interesting properties, CNO is recently getting a significant attention, particularly in the area of energy storage device application. Among others, the important properties of CNO include high BET surface area (500 $m^2/g$), high electrical conductivity (2-4 S/cm), and high thermal stability and appropriate mesoporous structure.[26,27] Currently two structurally distinct CNO are synthesized by arc-discharge method and CNO derived from nano-diamond. First, nanodiamond-driven CNOs (N-CNOs) are produced by placing detonation nanodiamond powders (3-5 nm in

diameter) in the furnace and annealing them at high temperature (1400-1900 °C) under Ar gas flow (**Figure 1.12b**). In the process of annealing, a tetrahedral, $sp^3$-bonded carbon network in nanodiamond is rearranged to form thermodynamically more stable $sp^2$- carbon-onion structure. The annealing temperature around 1650 °C produces N-CNOs with high quality and optimal characteristics in terms of electrical conductivity (2 S/cm) and BET surface area (~500 $m^2/g$). The produced N-CNO is 3-5 nm in diameter and consists of 4-6 concentric carbon layers. In N-CNOs, the concentric carbon shells deviate from perfect spheres and include amorphous phase/defects. Overall, N-CNO contains the significant structural disorder. The second type of CNO we synthesize is driven by arc-discharge (A-CNOs) (**Figure 1.12a**). A-CNOs are synthesized in a large quantity (3 mg/min) by producing arc between two pure graphite electrodes submerged in deionized water. This method was found to produce spherical carbon nano-onions as well as polyhedral and nested onion-like particles. I optimized growth condition to produce the materials with higher purity and narrow polydispersity in previous work. These include the control over many growth parameters by choosing appropriate power, maintaining optimal gap between two electrodes, and their proper alignment, and optimal temperature of the surrounding water. At the typical growth condition (50-70 A, 17 V) we employed, we found that the produced A-CNOs are ~20-40 nm in diameter and contains 30-40 concentric carbon layers surrounding a hollow core.

The results of the study using CNO as a support will be described in the next section.

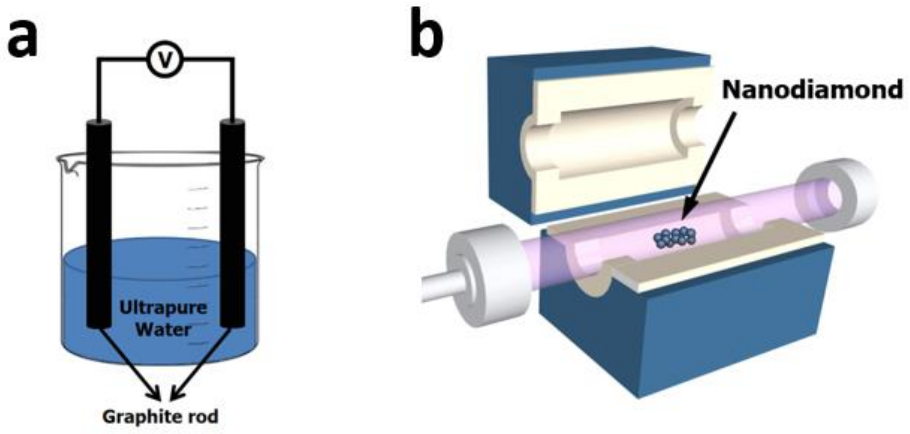


**Figure 1.12. Schematic representation of synthesis method about carbon nano onions.** (a) Arc - discharge method (b) Nanodiamond Derived CNOs.

### 1.6. Representative evaluation method

*1.6.1. Oxygen reduction reaction*

The catalytic activity for oxygen reduction reaction (ORR) is evaluated using a rotating disk electrode by linear sweep voltammetry (LSV). This method is the most effective and well-known method for studying the reaction rate of electrodes. The RRDE can control the supply rate of the solution to the electrode, so that the limiting current due to the limitation of the supply rate appears, which can be used to know the reaction rate at the electrode. The ORR equation according to the type of electrolyte is as follows.

Alkaline media:

$O_2 + 2H_2O + 4e^- \rightarrow 4OH^-$ (4 electron reaction) (5)

$O_2 + H_2O + 2e^- \rightarrow HO_2^- + OH^-$ (2 electron reaction) (6)

$H_2O + HO_2^- + 2e^- \rightarrow 3OH^-$

Acid media:

$O_2 + 4H^+ + 4e^- \rightarrow 2H_2O$ (4 electron reaction) (7)

$O_2 + 2H^+ + 2e^- \rightarrow H_2O_2$ (2 electron reaction) (8)

$H_2O_2 + 2H^+ + 2e^- \rightarrow 2H_2O$

Important factors which are the charge transfer number, current density and onset potential are able to be found by using RRDE method for ORR. Onset potential indicates the potential at which current starts to rise from the baseline in the voltammogram. It is interpreted that the reaction rate and catalytic performance are good with high initiation potential. The current density is normalized by the geometric area of the catalyst. The current density is related with consumption or production rate of oxygen or hydrogen. Therefore, this value is also closely related to the charge transfer number (n). The ORR is able to be roughly classified into two types. One is a direct four electrons reaction with no side reactions, and the other is a two electrons reaction that produces peroxide. The n value can be obtained from the RRED experiment along with the following equation. As the value of n approaches 4, it can be regarded as a complete oxygen reduction reaction.

$$\frac{4\times i_d}{i_d+\frac{i_r}{N}} \quad (9)$$

$i_d$: disk current

$i_r$: ring current

N: collection efficiency

*1.6.2. Tafel slope*

The Tafel slope can be explained as follows. The potential for further electrochemical reactions is called overpotential. This is related to the Tafel equation, and the slope value derived from this equation is called the Tafel slope.

$$\eta = a + b \log i \quad (10)$$

η: overpotential

b: Tafel slope

i: current density

a: Tafel constants

That is, the lower the Tafel slope, the less overpotential is required, which can be roughly seen as the catalyst exhibits high activity. The interpretation from the Tafel slope is important because the performances of ORR are similar in the platinum catalyst experiments.

*1.6.3. Durability test*

In the cyclic voltammetry (CV) method, the potential is varied at a constant rate in a given potential range, it is a method to analyze the current response characteristic. The cycle from the start of a specific potential to its return to its original potential at the inflection point is seen as a cycle. This CV method is mainly used for analyzing electrochemical active surface area in fuel cells. **Figure 1.13** shows the CV results of platinum on aqueous perchloric acid solution with nitrogen purging. In the **figure 1.13**, the part denoted by ECSA represents the amount of charge required for the adsorption of hydrogen on the platinum surface (current x time: potential on x axis can be converted into time when the circulation rate is known). Since the amount of charge used for hydrogen adsorption of atomically smooth platinum is fixed, the active area of the platinum catalyst synthesized from this relative charge amount can be obtained.

$$\text{ECSA} = \frac{Q_H}{L \times q_H} \qquad (11)$$

$Q_H$: The charge for the hydrogen adsorption

L: The weight of the Pt loading

$q_H$: The charge required for monolayer adsorption of hydrogen on a Pt surface (210 μC/cm$^2$)

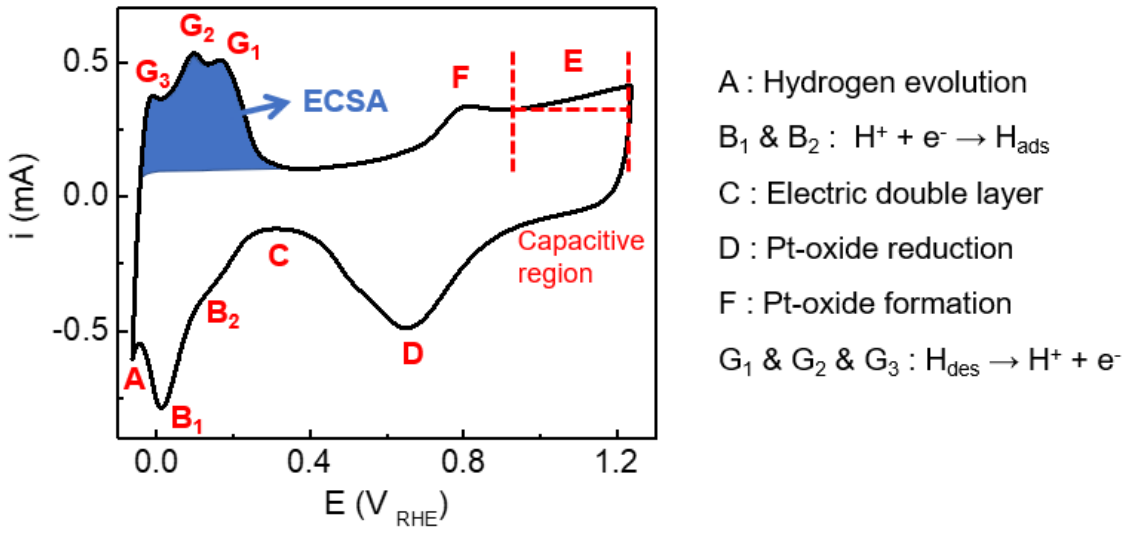


**Figure 1.13.** The CV curve of commercial Pt/C electrocatalyst in nitrogen saturated 0.1 M $HClO_4$.

As shown in the box in **figure 1.14**, it can also be applied to the analysis of the type of catalyst support and the deterioration of the catalyst. In the **figure 1.14**, A is a carbon nanoparticle as a support and B is a carbon nanotube as a carrier. The solid line is the result of CV performed immediately after synthesizing the catalyst, and the dotted line is the CV result after leaving the synthesized catalyst at 1.2 V for 192 hours (accelerated durability test; ADT). As can be seen from the CV results, when the carbon nanotubes are used as the support for Pt, there is no significant difference in the active area of the CV results even after ADT of the catalyst compared to the carbon nanoparticles. This means that the carbon nanotube carrier is superior in durability.[28]

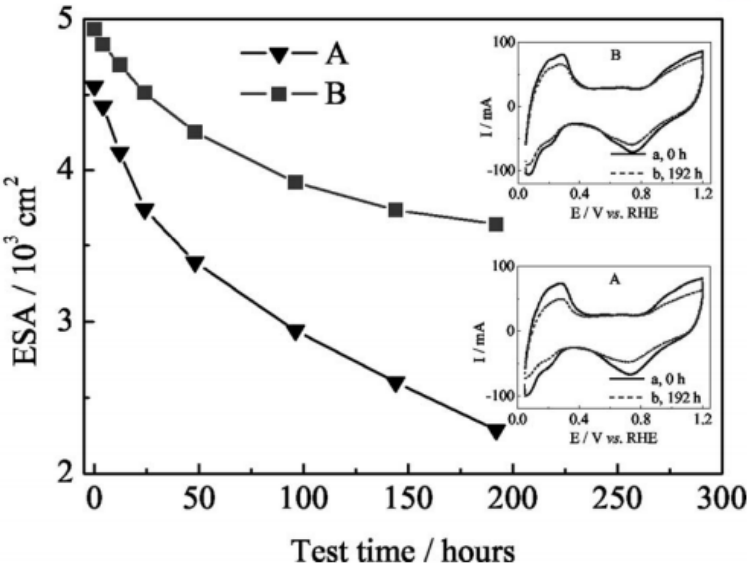


**Figure 1.14. ECSA vs. test time plots.** Inset CVs of Pt/C electrode (A) and Pt/CNT electrode (B) before (a) and after (b) holding at 1.2 V (vs. RHE) for 192 hours in 0.5 mol $L^{-1}$ $H_2SO_4$, scan rate 0.01 V $s^{-1}$. Electrode area 2.3 by 2.3 $cm^2$ from ref. 28.

Electrochemical durability test for electrocatalyst normally is carried out by continuously applying linear potential sweeps in fixed potential range for ORR. It is also possible to measure the change in catalytic durability over a certain period of time by fixing a constant voltage or current.

*1.6.4. Methanol oxidation reaction*

PEM fuel cells have been running on pure hydrogen gas as a fuel and air as an oxidant. This is going to be the small system case. But, in large systems the hydrogen fuel will come from some kind of fuel reforming system. Current hydrogen production methods are obtained by reforming fossil fuels due to low economic efficiency of water electrolysis, and poisoning of platinum catalyst due to impurities generated at this time is pointed out as a problem. The deterioration of fuel cell performance due to the carbon monoxide (CO) poison on the site of platinum catalyst is a serious problem. It is essential to develop a tolerant catalyst capable of preventing the degradation of the anode catalyst due to the poisoning of the CO contained in the reformed hydrogen. Through the methanol oxidation experiments, the tolerance of the catalyst can be checked by confirming the absence of CO through complete oxidation and the resistance to oxidation by low methanol oxidation reaction. In addition, the tolerance of carbon monoxide can be calculated through the relationship between methanol oxidation reaction and the oxidation of CO like species. This is explained on the next chapter.

**1.7. Reference**

(1) Ohayre, R. P. Cha, S. W.; Colella, W.; Prinz, F. B. Fuel Cell Fundamentals, John Wiley & Sons (Korean: Hanteemedia), 2008.

(2) Greeley, J.; Stephens, I. E. L.; Bondarenko, A. S.; Johansson, T. P.; Hansen, H. A.; Jaramillo, T. F.; Rossmeisl, J.; Chorkendorff, I.; Nørskov, J. K. Alloys of platinum and early transition metals as oxygen reduction electrocatalysts. *Nature Chemistry* **2009,** *1*, 552.

(3) Nørskov, J. K.; Rossmeisl, J.; Logadottir, A.; Lindqvist, L.; Kitchin, J. R.; Bligaard, T.; Jónsson, H. Origin of the Overpotential for Oxygen Reduction at a Fuel-Cell Cathode. *The Journal of Physical Chemistry B* **2004,** *108*, (46), 17886-17892.

(4) Ramaker, D. E.; Korovina, A.; Croze, V.; Melke, J.; Roth, C. Following ORR intermediates adsorbed on a Pt cathode catalyst during break-in of a PEM fuel cell by in operando X-ray absorption spectroscopy. *Physical Chemistry Chemical Physics* **2014,** *16*, (27), 13645-13653.

(5) Stamenkovic, V. R.; Mun, B. S.; Arenz, M.; Mayrhofer, K. J. J.; Lucas, C. A.; Wang, G.; Ross, P. N.; Markovic, N. M. Trends in electrocatalysis on extended and nanoscale Pt-bimetallic alloy surfaces. *Nature Materials* **2007,** *6*, 241.

(6) Mayrhofer, K. J. J.; Ashton, S. J.; Meier, J. C.; Wiberg, G. K. H.; Hanzlik, M.; Arenz, M. Non-destructive transmission electron microscopy study of catalyst degradation under electrochemical treatment. *Journal of Power Sources* **2008,** *185*, (2), 734-739.

(7) Mayrhofer, K. J. J.; Meier, J. C.; Ashton, S. J.; Wiberg, G. K. H.; Kraus, F.; Hanzlik, M.; Arenz, M. Fuel cell catalyst degradation on the nanoscale. *Electrochemistry Communications* **2008,** *10*, (8), 1144-1147.

(8) Shao-Horn, Y.; Sheng, W. C.; Chen, S.; Ferreira, P. J.; Holby, E. F.; Morgan, D. Instability of Supported Platinum Nanoparticles in Low-Temperature Fuel Cells. *Topics in Catalysis* **2007,** *46*, (3), 285-305.

(9) Schlögl, K.; Mayrhofer, K. J. J.; Hanzlik, M.; Arenz, M. Identical-location TEM investigations of Pt/C electrocatalyst degradation at elevated temperatures. *Journal of Electroanalytical Chemistry* **2011,** *662*, (2), 355-360.

(10) Borup, R.; Meyers, J.; Pivovar, B.; Kim, Y. S.; Mukundan, R.; Garland, N.; Myers, D.; Wilson, M.; Garzon, F. Scientific aspects of polymer electrolyte fuel cell durability and degradation. *Chemical Reviews* **2007**, *107*, 3904-3951.

(11) Gasteiger, H. A.; Kocha, S. S.; Sompalli, B.; Wagner, F. T. Activity benchmarks and requirements for Pt, Pt-alloy, and non-Pt oxygen reduction catalysts for PEMFCs. *Applied Catalysis B: Environmental* **2005**, *56*, 9-35.

(12) Galeano, C.; Meier, J. C.; Peinecke, V.; Bongard, H.; Katsounaros, I.; Topalov, A. A.; Lu, A.; Mayrhofer, K. J. J.; Schüth, F., Toward highly stable electrocatalysts via nanoparticle pore confinement. *Journal of the American Chemical Society* **2012**, *134*, (50), 20457-20465.

(13) Claudio, B.; Stefano, M.; P., C. H. W.; Christian, M. J.; K., S. A.; Marc, H.; Carolina, G.; Jan-Dierk, G.; Ferdi, S.; J., M. K. J., Confined-space alloying of nanoparticles for the synthesis of efficient PtNi fuel-cell catalysts. *Angewandte Chemie International Edition* **2014**, *53*, (51), 14250-14254.

(14) Mezzavilla, S.; Baldizzone, C.; Swertz, A.-C.; Hodnik, N.; Pizzutilo, E.; Polymeros, G.; Keeley, G. P.; Knossalla, J.; Heggen, M.; Mayrhofer, K. J. J.; Schüth, F., Structure–activity–stability relationships for space-confined $Pt_xNi_y$ nanoparticles in the oxygen reduction reaction. *ACS Catalysis* **2016**, *6*, (12), 8058-8068.

(15) Junliang, Z.; B., V. M.; Ye, X.; Manos, M.; R., A. R. Controlling the catalytic activity of platinum-monolayer electrocatalysts for oxygen reduction with different substrates. *Angewandte Chemie International Edition* **2005,** *44*, (14), 2132-2135.

(16) Xie, X.; Chen, S.; Ding, W.; Nie, Y.; Wei, Z. An extraordinarily stable catalyst: Pt NPs supported on two-dimensional $Ti_3C_2X_2$ (X = OH, F) nanosheets for oxygen reduction reaction. *Chemical Communications* **2013,** *49*, (86), 10112-10114.

(17) Murata, S.; Imanishi, M.; Hasegawa, S.; Namba, R. Vertically aligned carbon nanotube electrodes for high current density operating proton exchange membrane fuel cells. *Journal of Power Sources* **2014,** *253*, 104-113.

(18) Tsuji, E.; Yamasaki, T.; Aoki, Y.; Park, S.-G.; Shimizu, K.-i.; Habazaki, H. Highly durable platelet carbon nanofiber-supported platinum catalysts for the oxygen reduction reaction. *Carbon* **2015,** *87*, 1-9.

(19) Zhu, J.; Xiao, M.; Zhao, X.; Liu, C.; Ge, J.; Xing, W. Strongly coupled Pt nanotubes/N-doped graphene as highly active and durable electrocatalysts for oxygen reduction reaction. *Nano Energy* **2015,** *13*, 318-326.

(20) Hwang, S.-M.; Lee, S.; Sohn, Y.-J.; Yang, T.-H.; Park, G.-G. Durable and Water Manageable Ordered Mesoporous Supports for Polymer Electrolyte Fuel Cells. *ECS Transactions* **2013,** *58*, (1), 1763-1766.

(21) Pech, D.; Brunet, M.; Durou, H.; Huang, P.; Mochalin, V.; Gogotsi, Y.; Taberna, P.-L.; Simon, P. Ultrahigh-power micrometre-sized supercapacitors based on onion-like carbon. *Nature Nanotechnology* **2010,** *5*, 651.

(22) Amit, P.; Frederic, M.; M., C. C.; Bevan, E.; K., N. A.; D., E. D.; Amar, K.; Luis, E. Reactivity Differences between Carbon Nano Onions (CNOs) Prepared by Different

Methods. *Chemistry – An Asian Journal* **2007,** *2*, (5), 625-633.

(23) S., R. A.; Bevan, E.; S., H. J.; Armen, A.; Luis, E. Preparation and Functionalization of Multilayer Fullerenes (Carbon Nano-Onions). *Chemistry – A European Journal* **2006,** *12*, (2), 376-387.

(24) Sano, N.; Wang, H.; Chhowalla, M.; Alexandrou, I.; Amaratunga, G. A. J. Synthesis of carbon 'onions' in water. *Nature* **2001,** *414*, 506.

(25) Banhart, F.; Füller, T.; Redlich, P.; Ajayan, P. M. The formation, annealing and self-compression of carbon onions under electron irradiation. *Chemical Physics Letters* **1997,** *269*, (3), 349-355.

(26) McDonough, J. K.; Frolov, A. I.; Presser, V.; Niu, J.; Miller, C. H.; Ubieto, T.; Fedorov, M. V.; Gogotsi, Y. Influence of the structure of carbon onions on their electrochemical performance in supercapacitor electrodes. *Carbon* **2012,** *50*, (9), 3298-3309.

(27) Portet, C.; Yushin, G.; Gogotsi, Y. Electrochemical performance of carbon onions, nanodiamonds, carbon black and multiwalled nanotubes in electrical double layer capacitors. *Carbon* **2007,** *45*, (13), 2511-2518.

(28) Shao, Y.; Yin, G.; Gao, Y.; Shi, P. Durability Study of Pt/C and Pt/CNTs Catalysts under Simulated PEM Fuel Cell Conditions. *Journal of The Electrochemical Society* **2006,** *153*, (6), A1093-A1097.

# Chapter 2: Curvature-induced metal-support interaction of an islands-by-islands composite of platinum catalyst and carbon nano-onion for durable oxygen reduction

## 2.1. Introduction

Platinum supported by carbon (Pt/C) is the most representative catalysts for oxygen reduction reaction (ORR) for fuel cells and metal air batteries. However, the electrocatalytic performances of the catalysts are not durable during long-term operation due to (i) loss of active Pt mass caused by carbon corrosion[1, 2] and (ii) Pt particle agglomeration.[3] Since carbon atoms at edges, defects and dislocations are susceptible to oxidation,[4, 5] graphitization[6] and surface passivation[4, 5] improve the corrosion resistivity of carbons. Non-carbon materials[7] are alternative to carbon blacks for the same purpose. Pt is agglomerated via Ostwald ripening (dissolution and re-deposition) and/or surface migration.[3] Nanostructured carbon supports having voids in which catalyst islands are trapped would be useful for suppressing Pt agglomeration. Ostwald ripening as well as surface diffusion is limited geometrically and confined locally in the nanostructured matrix. The examples include mesoporous carbon materials,[8-11] carbon nanotubes,[12] graphite nanoplatelets,[13] carbon nanofibers,[14] carbon aerogels[15], graphene[16] and carbon nanocage.[17] As other strategies to suppress Ostwald ripening and surface migration of Pt particles, non-carbon support materials characterized by strong metal-substrate interaction also improved the stability of Pt dispersion on them.[18-20]

To address the issues of the conventional carbon supports and guarantee the durability of catalysts, here we present carbon nano-onion (CNO), a new class of carbon allotrope, as a support for Pt catalysts. The CNO is spherical particles composed of concentric shells of $sp^2$-bonded carbon planes surrounding a hollow core. The CNO was characterized by:[21] (1) high electric conductivities and (2) large ionically accessible surface area originating *not* from micropores *but* from its small particle dimension in several nanometer. In this work, we demonstrate the use of CNO as a catalyst support for ORR. A limited number of works have been reported for the Pt/CNO systems where Pt nanoparticles are supported by CNO in the conventional *islands-on-a-particle* configuration (islands = Pt; particle = CNO).[22-24] Previously, a very small particle (<< 1 nm) of Pt (which is not clearly identified) was electrodeposited on ~6 nm CNO[22] or Pt particles of 2 to 4 nm was loaded on non-spherical irregularly-shaped nitrogen-doped CNO (6 nm to several tens of nm).[23] On the other hand, here, we developed the composite consisting of Pt

and CNO of a similar size in the *islands-to-islands* configuration with an electronic interaction between them (the former and the latter islands in the *islands-to-islands* are Pt and CNO, respectively). Long-term durability and methanol durability of Pt was significantly improved by the CNO. Three key factors discouraging Pt agglomeration and carbon corrosion were suggested: (1) the *islands-to-islands* configuration of Pt/CNO, (2) the curvature-induced electron donation from CNO to Pt and (3) the graphitic concentric layers of CNO.

## 2.2. Experimental section

### 2.2.1. Chemical

The following reagents were purchased from Sigma-Aldrich: platinum (II) acetylacetonate (powder, 99.99 %) for loading Pt nanoparticles on supports; perchloric acid (70% in water) and potassium hydroxide (ACS reagent, pellet) for electrolytes; and nafion (5 wt.% in lower aliphatic alcohols and water). Commercial Pt/C (20 wt. % of Pt on Vulcan XC-72R; denoted as Pt/CB in this work) was purchased from Etek.

### 2.2.2. Synthesis of CNOs

CNOs were prepared by annealing nano-diamond powders of 3 to 5 nm in diameter (Dynalene NB50) at 1650 °C for 1.0 h under helium flow at 500 sccm in a furnace. As-produced CNO powders were cleaned by thermal treatment in the same furnace at 400 °C for 4 h under air for removing amorphous carbon impurities.

### 2.2.3. Preparation of Pt/CNO

5 mg of platinum (II) acetylacetonate was dissolved in a mixture of 2mL of acetic acid and 3 ml of ethanol by sonication for 30 min. After introducing 10 mg of CNO, the solution was stirred at 120 °C for 6 h. The suspension of CNO was stable for more than one day. The oxygen-containing surface functional groups are responsible for the stability of the suspension. During the thermal treatment, solvents were completely evaporated and the remaining dry powders were additionally baked. The Pt amount on Pt/CNO was estimated at 12.7 wt. % by thermogravimetric analysis (TA Q500). For comparison, the Pt amount on the commercially available Pt/CB was estimated at 18.5 wt. %.

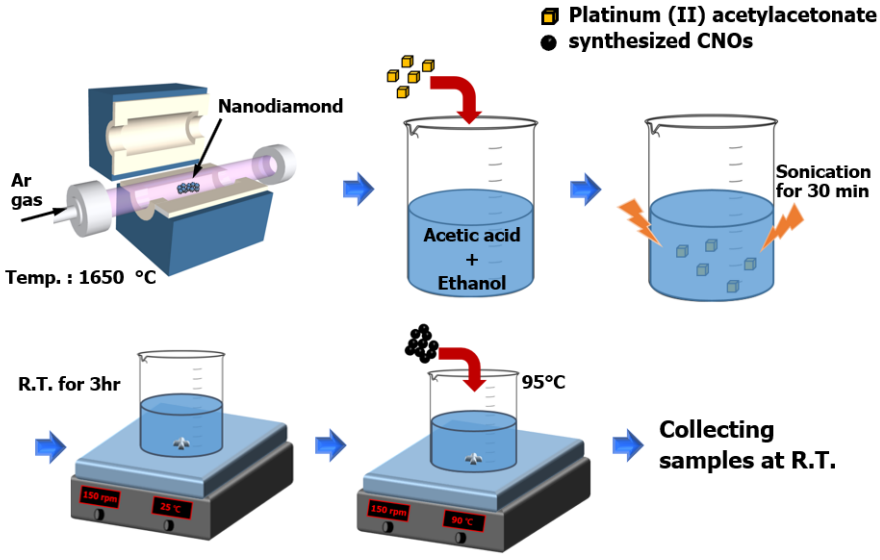


**Figure 2.1.** The preparation steps of the Pt/CNO electrocatalyst.

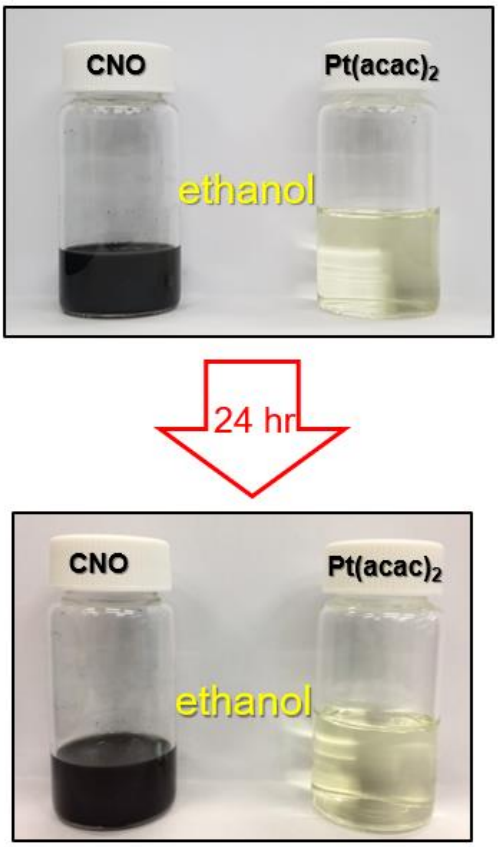


**Figure 2.2.** Stable ethanolic solution of CNO and $Pt(acac)_2$ for 24hr.

2.2.4. Physicochemical characterization

Change in binding energy of Pt after ORR operations was investigated by X-ray photoelectron spectroscopy (XPS; Thermo Scientific K-Alpha using a monochromic Al K α X-ray source). Carbon defects were detected by Raman spectroscopy (WITec alpha 30 0R) with He/Ne laser at 532 nm. The laser was focused on the surface of all samples by using a 50x objective lens. Diffraction patterns were obtained by X-ray diffractomete r (Bruker D8 advance diffractometer by using Cu-Kα radiation). All samples were scann ed from 2θ = 20 to 60 degree in a step scan at 0.05 degree $step^{-1}$. Electrical conductivi ties of pressed pellets of CNO were measured. 20 mg of powder was pressed between t wo steel pistons by applying pressures at 236 kPa. Voltages ($V$) applied between the tw o steel pistons were swept while currents ($I$) were measured. Resistances ($R$) were read from the slopes of current-voltage curves: $R = V / I$. Conductivities ($\kappa$) were calculated from the values of resistances by using geometric dimensions of the thickness of compr essed sample ($l$) and the cross-sectional area of compressed sample ($A$): $R = \kappa^{-1} (l / A)$. X-ray absorption fine spectra (XAFS) were measured by the Beamline 6D of the Pohan g Accelerator Laboratory (PAL) at 3GeV beam energy and 300 mA current.

2.2.5. Electrochemical characterization.

Cyclic voltammetry (CV) as well as linear sweep voltammetry (LSV) for ORR measurements were conducted by a potentiostat (BioLogic VMP 3). Three-electrode systems were configured with Pt wire as a counter electrode and a commercial Hg/HgO for alkaline media or a commercial Ag/AgCl (3 M KCl) for acid media as a reference electrode. Aqueous solution of 0.1 M KOH or $HClO_4$ was used as electrolyte. Rotating ring disk electrodes (RRDE) of glassy carbon disk and platinum ring were used as working electrodes. The RRDEs were polished consecutively with two different alumina powders (0.3 and 0.05 μm) and cleaned by sonication for 20 min with deionized water for removing alumina powders on electrodes. 20 mg of catalyst powders was dispersed in a mixture of 900 μl of ethanol and 100 μl of 5 wt.% Nafion suspension in alcohol (Sigma-Aldrich) by sonication for 30 min. 6 μl droplet of the catalyst ink placed on disk of polished RRDEs was dried in an oven at 80 °C for 5 min to evaporate solvent (loading = 955 μg catalyst $cm^{-2}$). Electrolytes were purged with nitrogen for measuring background currents while they were saturated with oxygen for measuring ORR currents. All potentials were reported versus the reversible hydrogen electrode (RHE) ($V_{RHE}$ = V versus RHE).

## 2.3. Results and discussion

### *2.3.1. The structure of Pt/CNO*

The CNO powders were produced by annealing nano-diamond powders of ~ 5 nm in diameter at 1650 °C under Ar gas flow in furnace. Surface area was estimated at 404 $m^2$ $g^{-1}$ by nitrogen adsorption via Brunauer-Emmet-Teller equation (**Figure 2.3**). The electric conductivity of its pressed pellets was estimated at 4 S $cm^{-1}$, which is consistent with the previously reported value of CNO[25] and equal to the value of pressed pellets of carbon black.[26] The size of the CNO particles (5 nm ± 1nm) were identical to that of the nano-diamond particles as their precursors while their onion-like lamination of multiple graphitic layers were distinguished from the nano-diamond structure (**Figure 2.4** for CNO versus **Figure 2.5** for nano-diamond). Each CNO particle was interpreted as a single crystallite of 4 to 6 spherical graphitic layers by XRD patterns in terms of its interlayer spacing ($d_{002}$) and crystallite size in the [002] direction ($L_c$) (**Figure 2.6a**). The strong single-graphene characteristics distinguishing CNO from conventional carbon black support (Vulcan XC-72R, here) was supported by 2D (more accurately $2D_{1A}$) peak of Raman spectra (**Figure 2.6b**).

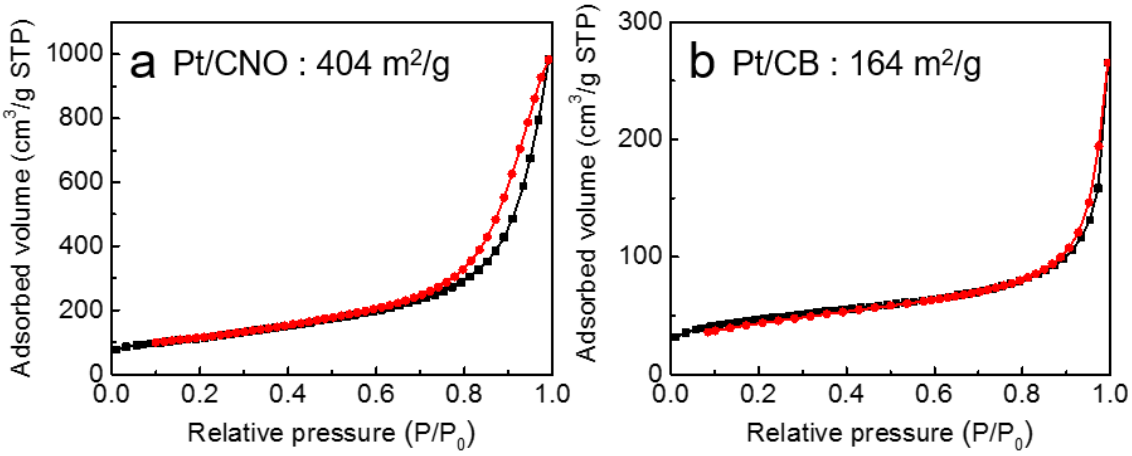


**Figure 2.3. Nitrogen adsorption/desorption isotherm at 77 K.** (a) Pt/CNO. (b) Pt/CB. Surface areas were calculated by using the Brunauer, Emmet and Teller (BET) model: 404 $m^2$ $g^{-1}$ for Pt/CNO and 164 $m^2$ $g^{-1}$ for Pt/CB.

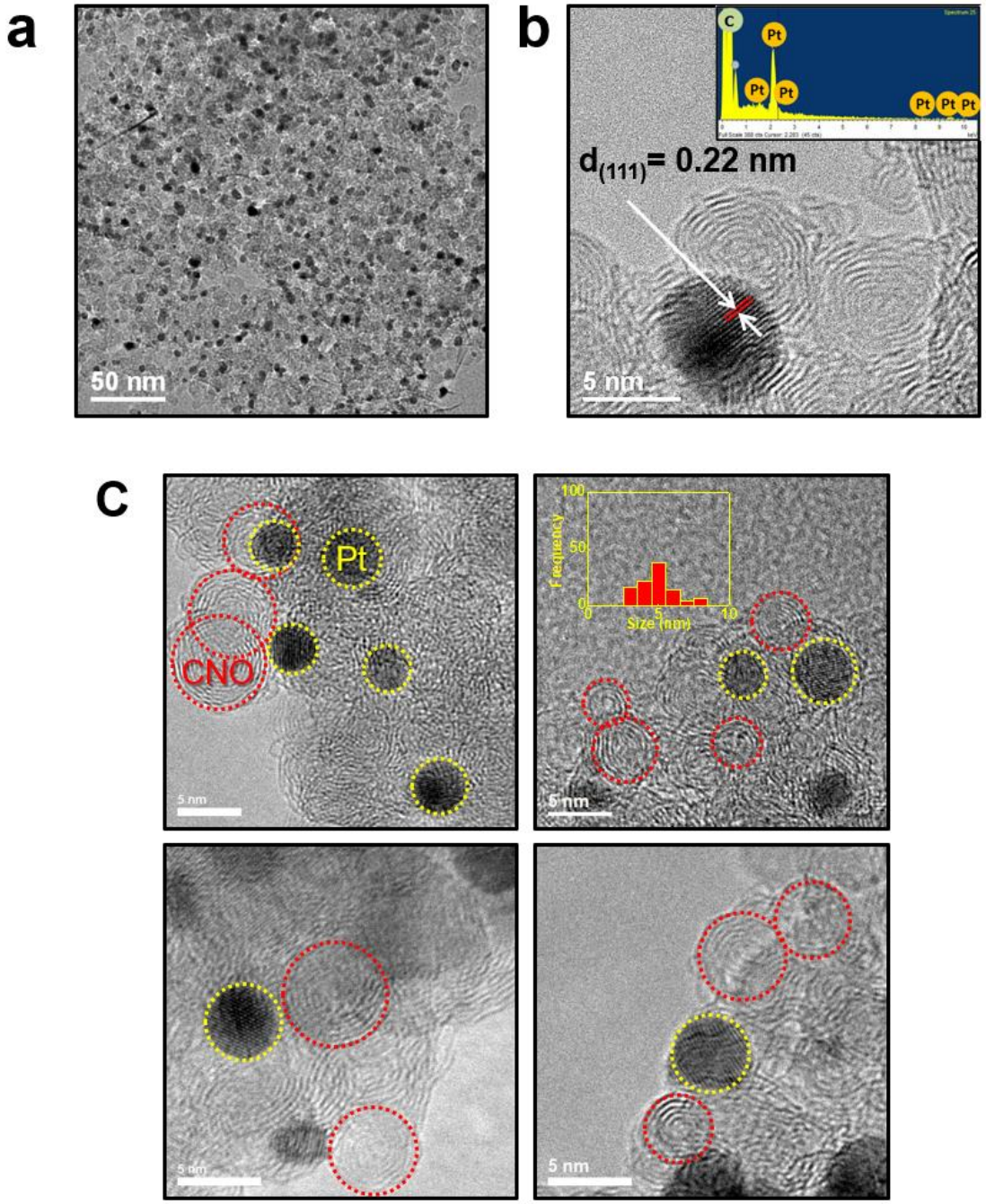


**Figure 2.4. TEM image of Pt/CNO.** (a-c) Transmission electron microscopic (TEM) images of Pt/CNO (inset: energy dispersive spectra in b). The sizes of the CNO particles that is clearly identified as concentrically graphene-layered objects. More than 50 particles were counted.

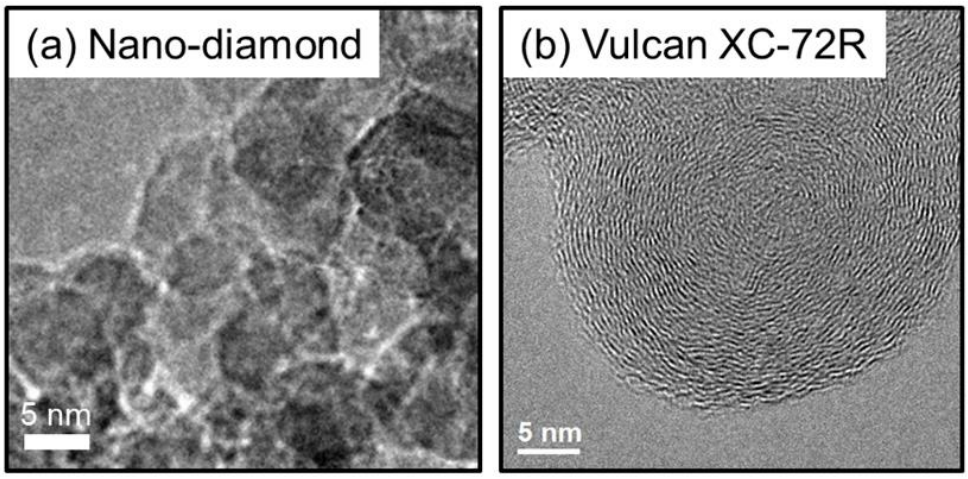


**Figure 2.5. TEM images.** (a) Nano-diamond. (b) Vulcan XC-72R

The peaks at 2θ = 25.6 and 43.3 degree in XRD patterns (**Figure 2.6a**), assigned to (002) and (100) planes of graphite respectively, indicate that the $sp^3$-carbon network of nano-diamond particles were rearranged to form thermodynamically more stable $sp^2$-carbon layers in the onion shape during the annealing step. The interlayer spacing between graphene sheets of the CNO ($d_{002}$), calculated from the (002) peak by Bragg's law, was estimated closer to $d_{002}$ of graphite rather than carbon black: graphite (0.337 nm from our measurement but 0.335 nm as the ideal value) < CNO (0.345 nm) << Vulcan XC-72R as a carbon black (0.362 nm). The crystallite size of CNO in the [002] direction ($L_c$), calculated from peak widths of (002) peak by Scherer equation, was 1.5 nm (c.f. $L_c$ for Vulcan XC-72R = 1.2 nm), indicating four to six spherical layers in average. The crystallite size and the number of layers expected from XRD patterns corresponded to the particle sizes and the numbers of layers shown in the electron-microscopic images (**Figure 2.4b**) so that each single particle of CNO is considered as a crystallite.

The G-band peak at 1580 $cm^{-1}$ for the lattice phonon and the D-band peak at 1350 $cm^{-1}$ from scattering by disorder-activated edge phonon were observed for both CNO and CB in Raman spectra (**Figure 2.6b**). The D/G ratios (the peak intensity ratios of D to G) of both of the carbon materials (1.1 for Vulcan XC-72R and 1.3 for CNO) were higher than that of graphite (0.05). The clear difference between CNO and Vulcan XC-72R was observed at the 2D-band peak at 2680 $cm^{-1}$.[56] The peak was detected only in CNO. The 2D band is the second order of the D band and the second most prominent band of graphite so that it was formerly named G'.[57,58] The 2D peak position of CNO (2680 $cm^{-1}$) coincided with that of a single layer graphene. The full width at half maximum of CNO (FWHM, ~60 $cm^{-1}$) was larger than that of the single layer graphene (~30 $cm^{-1}$), closer to the FWHM of 2 or 3 layers graphene (~55 $cm^{-1}$) and smaller than the FWHM of glassy

carbon (77.1 $cm^{-1}$) and carbon paper (69.4$cm^{-1}$). The shape of the 2D peak of CNO was identical to that of the single layer graphene in that the peaks consist of only one component $2D_{1A}$. On the contrary, the 2D peaks of a-few layer graphenes are deconvoluted by four components ($2D_{1B}$, $2D_{1A}$, $2D_{2A}$ and $2D_{2B}$ in the ascending order of peak position) and graphite has a two-component 2D peak. Therefore, the CNO is supposed to have strong graphitic characteristics when compared with the Vulcan XC-72R.

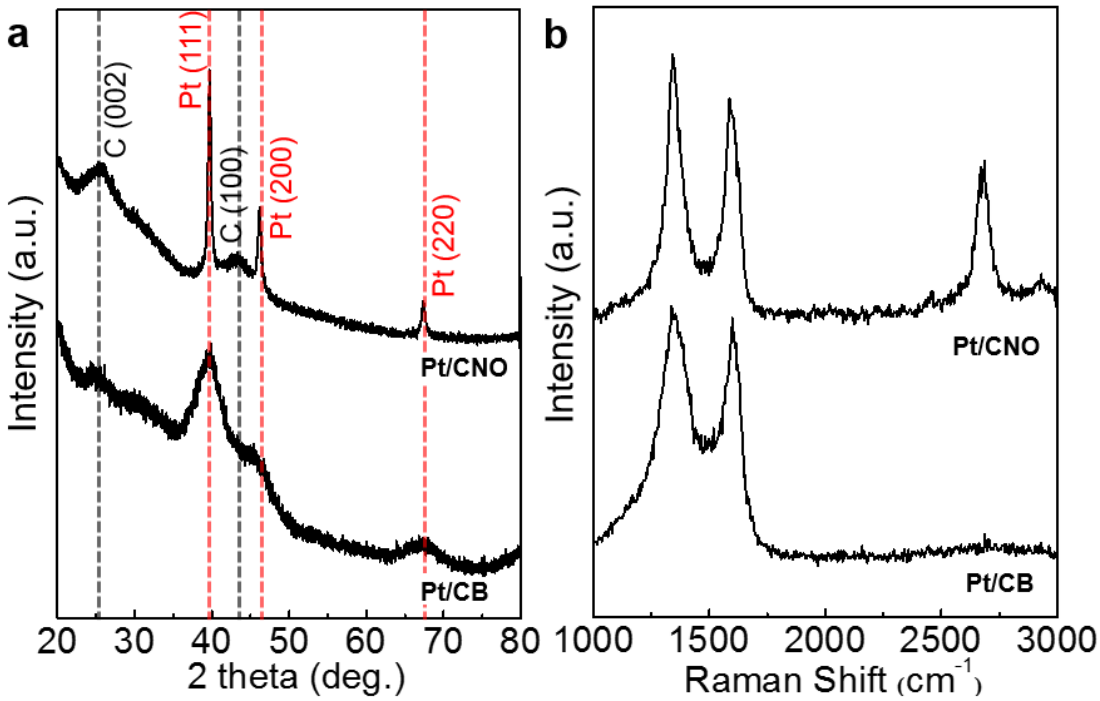


**Figure 2.6. Pt/CNO versus Pt/CB.** (a) X-ray diffraction (XRD) patterns. (b) Raman spectra.

*2.3.2. islands-by-islands structure of Pt/CNO*

Pt catalyst nanoparticles were well mixed with (rather than dispersed on) CNO particles because the constituent particles (Pt and CNO) are of the similar size (5.3 ± 1.3 nm for CNO versus 2.8 ± 0.83 nm for Pt in **Figure 2.4a** and **b**). Pt particles were surrounded or pocketed by CNO particles so that each Pt particle is physically isolated from other Pt particles (**Figure 2.7b**). The *islands-by-islands* configuration of Pt/CNO is different from the *islands-on-a-particle* configuration of the conventional Pt/CB (CB = Vulcan XC-72R; size = 20 to 30 nm, 28 nm in average) where the catalyst particles sit on a larger particle of carbon black (**Figure 2.7a**). We expected the catalyst stability in the presence of CNO because the *islands-by-islands* configuration possibly blocked Pt agglomeration. The effects of carbon corrosion would be insignificant in ORR at room temperature and at the reductive potential range of the electrochemical experiments. Both of two major routes for Pt agglomeration (Ostwald ripening

and surface migration) are blocked by the *islands-by-islands* configuration of Pt/CNO. Highly tortuous void structure developed from packing of small CNO particles limits the distance between dissolution points and re-precipitation points (Ostwald ripening suppression in **Figure 2.7c** and **d**). The local radii of curvature of the surface of CNO packing matrices are similar to the Pt particle radii so that Pt atoms from a Pt particle cannot help but travel along longer ways via more tortuous and discontinuous carbon phase consisting of the CNO before meeting another Pt particles (surface migration suppression in Figure 1e and f; $\boldsymbol{l_1} < \boldsymbol{l_2}$ at $\boldsymbol{d_1} = \boldsymbol{d_2}$). Therefore, it might be less possible for Pt particles to be agglomerated during long-term fuel cell operations in Pt/CNO catalyst composites.

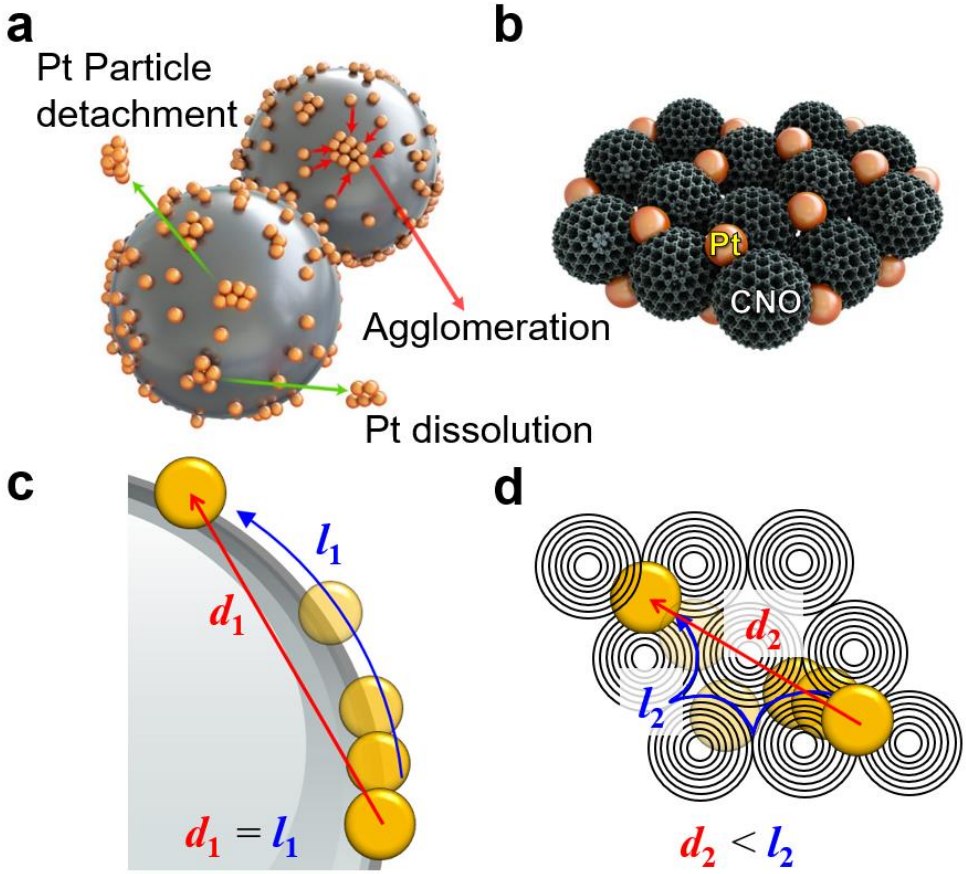


**Figure 2.7.** (a) *Islands on a particle* for Pt/CB. (b) *Islands by islands* for Pt/CNO. The sizes of Pt particles (orange spheres) in c and d are identical. Pt particles were drawn smaller than CNO particles for the best view to emphasize Pt particles entrapped between CNOs even if both particles are similar in size (5.3 ± 1.3 nm for CNO versus 2.8 ± 0.83 nm for Pt). (c, d) Oswald ripening or surface migration in Pt/CB (e) and Pt/CNO (f). ***d*** = particle-to-particle distance. ***l*** = pathways of dissolved ions in Ostwald ripening or atoms in surface migration.

*2.3.3. ORR activity of Pt/CNO*

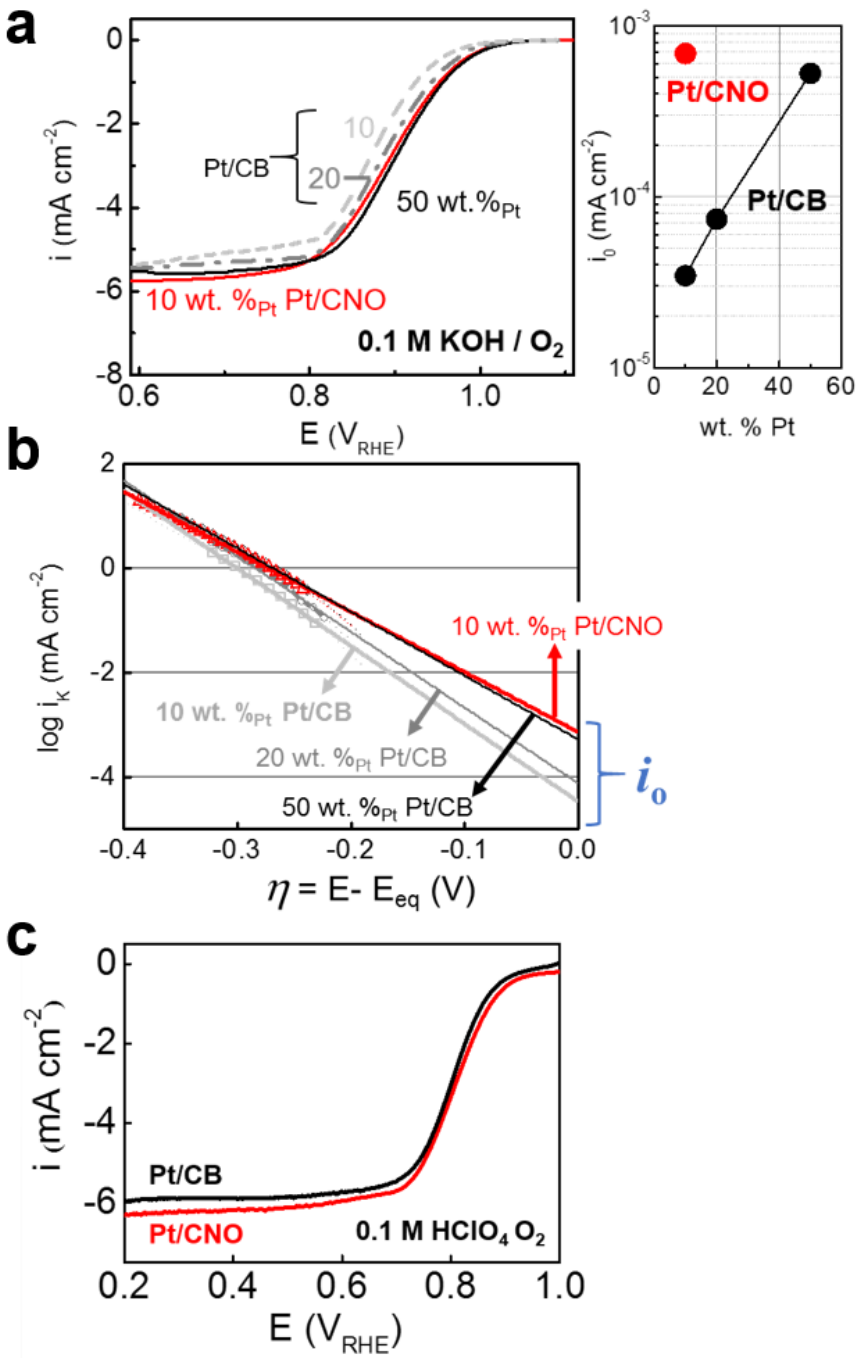


**Figure 2.8. ORR**. Aqueous solution of 0.1 M KOH and $HClO_4$ were used as the alkaline and acid media, respectively. 10 and 20 wt. % Pt were used in Pt/CNO and Pt/CB respectively unless indicated otherwise. (a) ORR polarization in oxygen-saturated alkaline media (Figure S5 for acid media) at 10 mV $s^{-1}$ with 1600 rpm. Three different Pt amounts (10, 20 and 50 wt. % Pt) were loaded on CB while 10 wt. % Pt was loaded on CNO. (b) Corresponding Tafel plots for Pt/CNO and Pt/CB in 0.1 M KOH. (c) ORR polarization curve in oxygen-saturated acid media (Figure 2a for alkaline media) at 10 mV $s^{-1}$ with 1600 rpm.

The ORR electroactivities of Pt/CNO in comparison with their conventional counterpart Pt/CB were studied in both alkaline and acidic electrolytes (0.1 M aqueous solutions of KOH and $HClO_4$ respectively). Interestingly, Pt/CNO was superior to Pt/CB at 10 wt. % Pt loading in terms of onset potential and exchange current while 10 wt. % Pt/CNO was equivalent or still superior to 50 wt. % Pt/CB (**Figure 2.8a** and **b** for alkaline media and **Figure 2.8c** for acid media). At the fixed loading in 10 wt. % Pt, the exchange current ($i_o$) of Pt/CNO was 20 times higher than that of its Pt/CB counterpart: $69 \times 10^{-5}$ mA/cm$^2$ for Pt/CNO versus $3.5 \times 10^{-5}$ mA/cm$^2$ for Pt/CNO. The improved ORR electroactivity of Pt/CNO could not be explained by the *islands-by-islands* configuration. The strong Pt-carbon interaction induced by high-curvature surface of CNO is thought to be the main reason for the improvement (discussed below).

*2.3.4. The durability test of Pt/CNO*

As expected from the geometric advantages of the *islands-by-islands* configuration, the electrochemical stability was guaranteed by the Pt/CNO composite catalysts. There was insignificant change in ORR current for Pt/CNO in alkaline media at 0.329 $V_{RHE}$ for > 4 h (**Figure 2.9**). On the contrary, Pt/CB showed a serious decrease in current during the initial half hour followed by slow but continuous decrease. Little change in currents of cyclic voltammograms (CVs) in nitrogen-purged acid media or electrochemical surface area (ECSA) of Pt/CNO was clearly contrast to the serious decrease in those of Pt/CB (**Figure 2.10a** and **b** for CVs and **Figure 2.11** for ECSA).

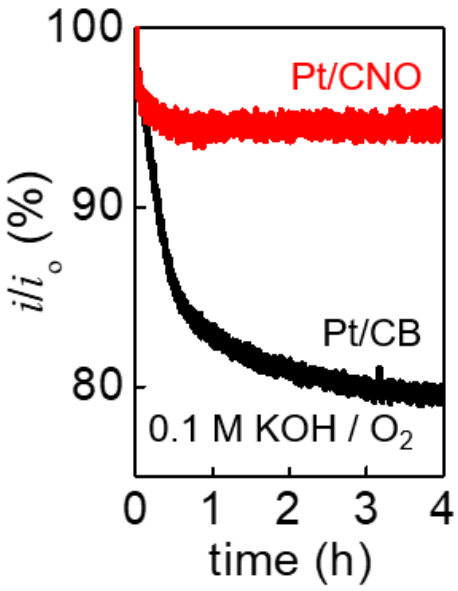


**Figure 2.9.** Chronoamperometric responses in the alkaline media saturated by oxygen at 0.329 $V_{RHE}$ with 1600 rpm.

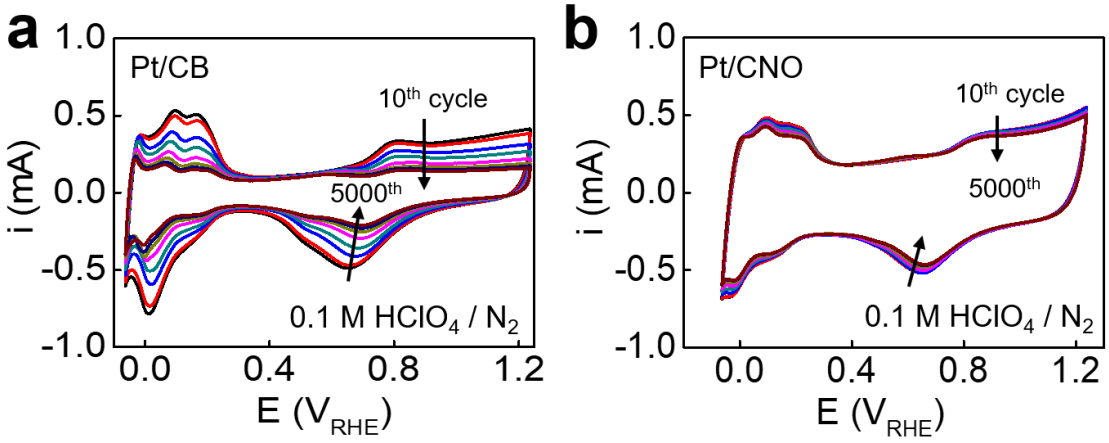


**Figure 2.10.** (a, b) 5000 times repeated cyclic voltammograms at 50 mV $s^{-1}$ in the acid media purged by nitrogen: Pt/CB in a and Pt/CNO in b.

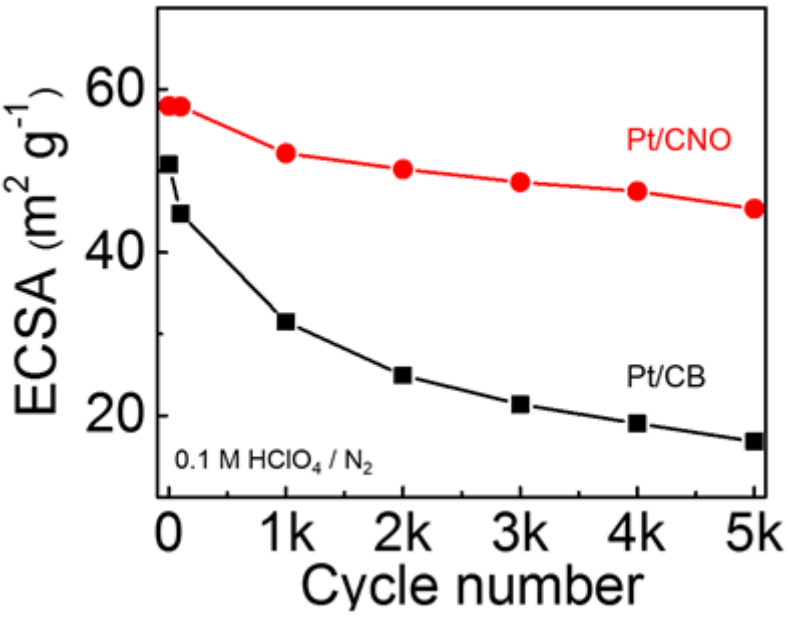


**Figure 2.11.** The change in the electrochemical surface area (ECSA) of Pt/CNO and Pt/CB along voltammetric cycles**.**

Suppression of Pt agglomeration in the presence of CNO was clearly shown by analysing transmission electron microscope images before and after an accelerated durability test by sweeping potential between -0.1 $V_{RHE}$ and +1.2 $V_{RHE}$ for 5000 cycles (**Figure 2.12a-d**). Initially, both Pt/CB and Pt/CNO showed the identical particle size distribution of Pt on supports: mean diameters were 3.0 ± 0.77 nm for Pt/CB and 2.8 ± 0.83 nm for Pt/CNO. After experiencing ORR, Pt particles on CB agglomerated considerably to the size at 7.0 ± 4.0 nm (more than two times larger than the original particles) while the size of Pt on CNO increased slightly to 4.1±1.4 nm for Pt/CNO. The insignificant change in Pt particle size between before and after the durability test clearly confirms that the geometry of Pt/CNO composites in the *islands-by-islands* configuration are effective in suppressing Pt agglomeration. Changes in oxidation states of Pt during ORR, investigated by X-ray photoelectron spectroscopy (XPS), also supported that Pt agglomeration was suppressed in Pt/CNO.[19] Doublet peaks were observed in Pt 4f spectra (**Figure 2.12e**), each of which consists of three sub-peaks responsible for different oxidation states including Pt(0), Pt(II) and Pt(IV). Peak shifts to lower binding energy were observed for Pt/CB after the durability test. That is to say, more reduced states such as Pt(0) were dominantly developed during the repeated potential sweep. It indicates the possibility of Pt agglomeration because Pt agglomeration reduces the exposed surface of Pt particles and therefore the surface oxide of Pt. On the contrary, no difference in peak positions of Pt 4f spectra of Pt/CNO was observed between before and after the durability test.

*2.3.5. The metal-support interaction*

In addition to the geometric factor, the metal-support interaction possibly affects (1) the electroactivities of Pt catalysts and (2) the stability in Pt particle dispersion on supports. The possibility of electron transfer from CNO to Pt was observed experimentally from XPS and X-ray absorption near edge structure (XANES) spectra. The Pt 4f peaks of Pt/CNO in XPS spectra was observed at more negative binding energies than those of Pt/CB before the durability test: 70.78 eV for Pt/CNO versus 71.28 eV for Pt/CB (**Figure 2.12e**). The negative shift of Pt 4f in binding energy represents the electron transfer from carbon support to platinum[19] occurring more in Pt/CNO than Pt/CB. White line intensity of Pt/CNO in Pt L3-edge XANES spectra was much smaller than that of Pt/CB (**Figure 2.12f**). It indicates dramatic decrease in d-band vacancies of Pt when the support changes from CB to CNO. The d-band vacancies are most probably filled with electrons donated from CNO.

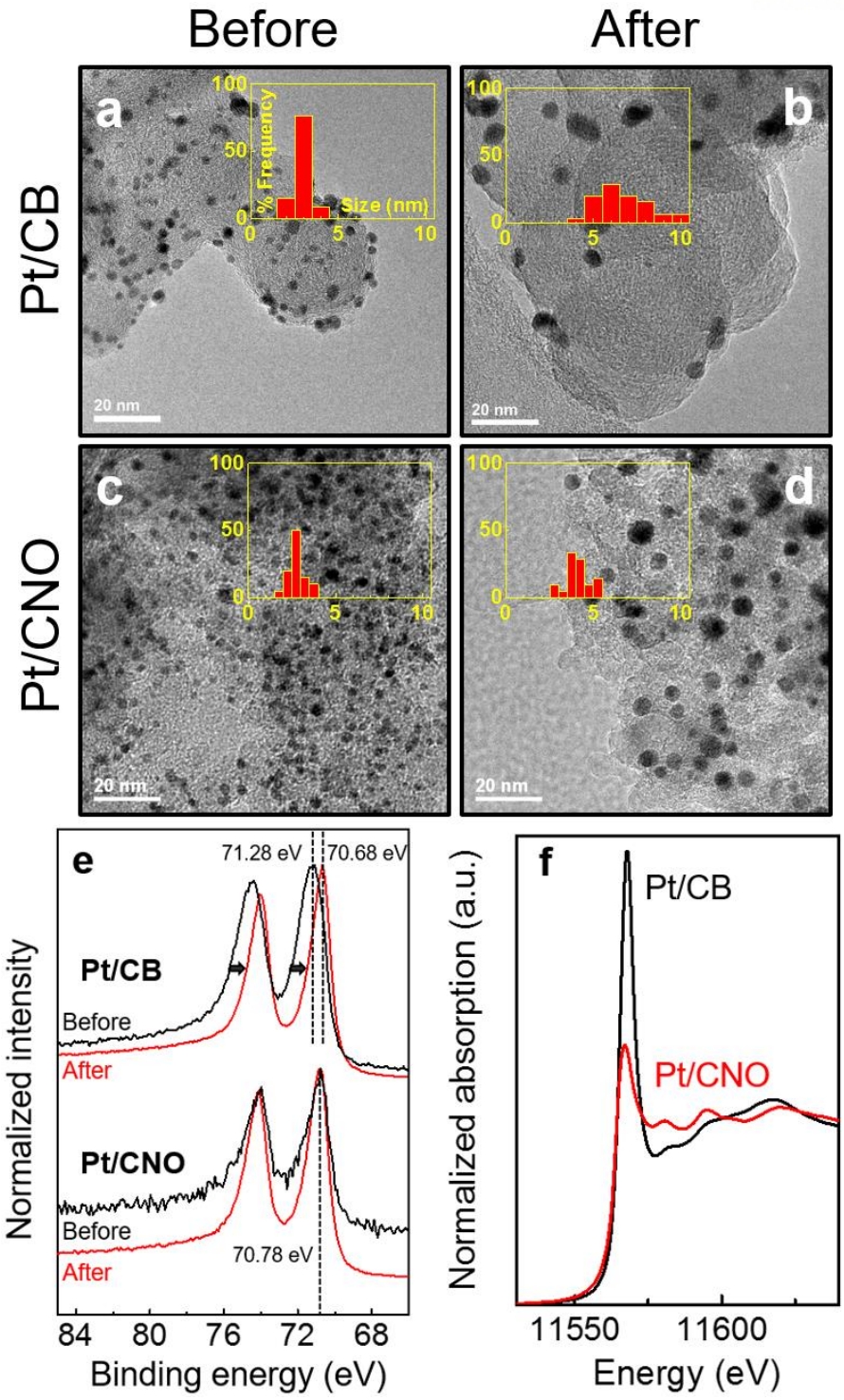


**Figure 2.12. Durability.** (a to d) TEM images (inset = size distribution) of Pt/CB (a, b) and Pt/CNO (c, d) before durability test (a, c) and after durability test (b, d). (e) X-ray photoelectron Pt 4f spectra of Pt/CB and Pt/CNO before and after durability test. The accelerated durability tests (ADT) were performed by sweeping potential between -0.1 $V_{RHE}$ and 1.2 $V_{RHE}$ for 5000 cycles. Nitrogen-saturated 0.1M $HClO_4$ solution was used as the electrolyte. (f) Pt L3-edge XANES spectra by a synchrotron light source.

The interaction between Pt and carbon supports was investigated by using density function theory (DFT) calculation (**Figure 2.13, Figure 2.15** to **2.18** and **Table 2.1**). Carbon nanoribbon models consisting of $sp^2$-carbon atoms have been widely used to represent amorphous and graphitic carbon support systems in DFT calculations.[27-29] The difference of planar and curved nanoribbons were recognized (**Figure 2.14**). The planar configuration did not show no hybridization between σ and π orbitals in carbon-carbon bonds.[30] On the other hand, the radial deformation of curved carbon nanoribbon systems broke the bond symmetry of graphene, leading to the $p_z$-orbital rotation and then the strong σ-π hybridization.[31] Therefore, the carbon nanoribbon models were adopted to describe (1) flat facets for describing less-curvature Vulcan XC-72R (size = 28 nm in average) and (2) curved facets of high-curvature CNO (size = 4 nm in average) (**Figure 2.15**). The lowest adsorption energy was achieved when the triangular facet of the $Pt_7$ nanoparticle was adsorbed on the carbon substrates (**Figure 2.16**). Each Pt atom in triangular facet was adsorbed on the π-bond of carbon substrates for strong interaction.[22] Interestingly and importantly, the adsorption energy of $Pt_7$ on $sp^2$ carbon nanoribbons ($\Delta E_{ads}^{Pt}$) decreased to more negative values when the nanoribbons were curved (**Figure 2.13** and **Figure 2.18**): e.g., $\Delta E_{ads}^{Pt}$ = -4.521 eV for zigzag nanoribbon (ZZNR) to -5.223 eV for curved ZZNR (c-ZZNR); $\Delta E_{ads}^{Pt}$ = -4.845 eV for armchair nanoribbon (ACNR) to -4.999 eV for curved ACNR (c-ACNR). It means that the Pt-carbon interaction increases by curving the nanoribbons or by replacing the large and less-curvature Vulcan XC-72R with the small and high-curvature CNO in this case. The strong interaction between Pt and the curved supports (or CNO) possibly suppresses the surface migration to edge sites that are thermodynamically most favored for $Pt_7$ adsorption (e.g., $\Delta E_{ads}$ = -5.956 eV for ZZNR edge).[23,32,33] On Vulcan XC-72R, however, Pt is agglomerated at the edge sites while Pt nanoparticles adsorbed on the flat facet are less likely found after durability test.

In addition to the Pt adsorption behaviour, the electron transfer from carbon substrate to Pt was estimated by the amount of atomic charge transfer ($\Delta q$) by using DFT calculations. For all cases, electrons were transferred from nanoribbons to $Pt_7$ nanoparticles (**Figure 2.13** and **Figure 2.18**).[22] More electrons were transferred to Pt (indicated by more negative values of $\Delta q$) when the flat $sp^2$ carbon nanoribbons were curved: $\Delta q$ = -0.672 e for c-ZZNR < -0.632 e for ZZNR facet; $\Delta q$ = -0.655 e for c-ACNR < -0.647 e for ACNR facet. The $\Delta q$ can be also estimated by the Fermi level change ($\Delta E_F$) of Pt induced by the adsorption of Pt nanoparticle.[22] The curved facet of the $sp^2$ carbon nanoribbon induced the larger increase in $E_F$ of $Pt_7$ than the flat facet did when the $Pt_7$ was adsorbed on the nanoribbons: $\Delta E_F$ = +0.401 and +0.385 eV for the curved facets versus +0.282 and +0.307 eV for the flat facets of ZZNR and ACNR systems, respectively (**Figure 2.13a** and **Figure 2.17**). The more electronic states are occupied by electrons with the Fermi level increasing so that the higher $\Delta E_F$ directly increases $|\Delta q|$. Well-developed basal planes existing on

the surface of the CNO, as an another cause for electron transfer in addition to curved geometry, possibly donate their π-electrons to Pt metal particles.[17,34] To this end, the strong Pt-CNO interaction is possibly helpful in stabilizing Pt against oxidation, preventing Pt dissolution and impeding the surface migration of Pt atoms, resulting in improving dispersion stability of Pt particles on CNO.

| | ZZNR | ACNR | c-ZZNR | c-ACNR |
|---|---|---|---|---|
| **Lattice A (Å)** | 50 | 50 | 50 | 50 |
| **Lattice B (Å)** | 12.3 | 12.7824 | 12.298 | 12.78 |
| **Lattice C (Å)** | 20 | 20 | 50 | 50 |
| **Composition** | $C_{160}H_{10}$ | $C_{162}H_{12}$ | $C_{160}H_{10}$ | $C_{156}H_{12}$ |

**Table 2.1.** Dimension of ZZNR, ACNR, c-ZZNR and c-ACNR. Lattice A, B and C correspond to the lattice in x, y and z-axis.

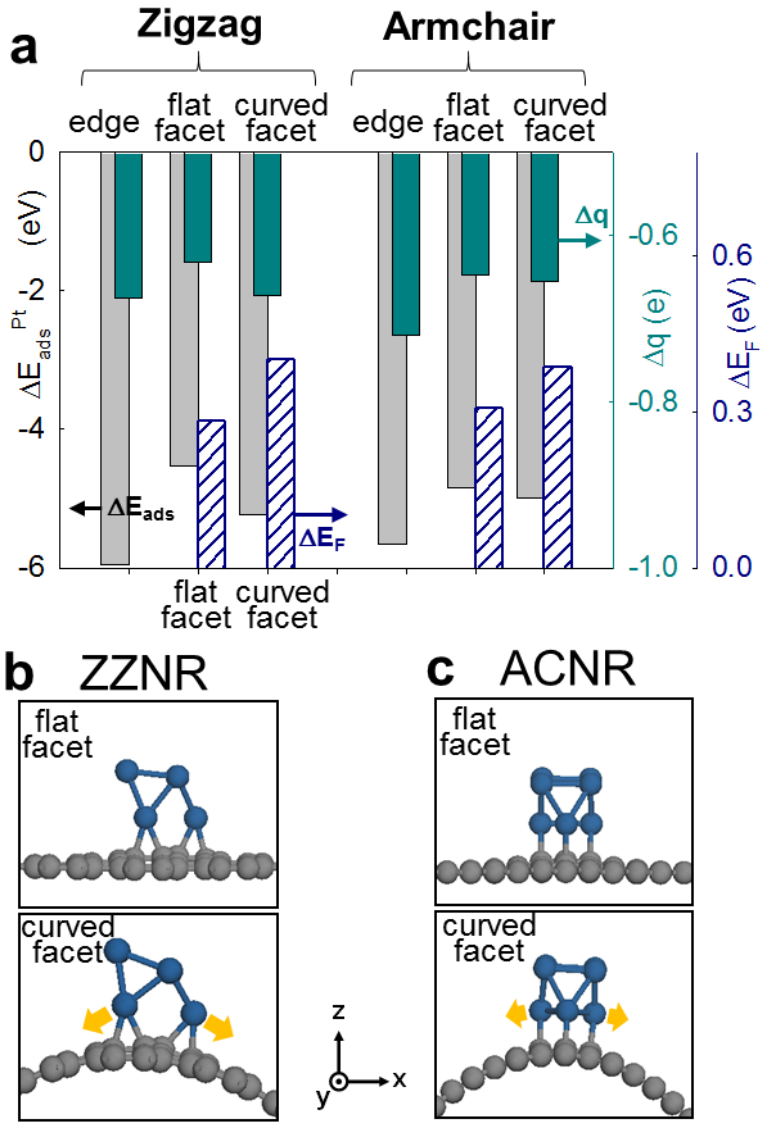


**Figure 2.13. Pt-support interaction.** (a) Adsorption energy ($\Delta E_{ads}^{Pt}$), the amount of atomic charge transfer ($\Delta q$) and Fermi level change ($\Delta E_F$) of Pt nanoparticles on carbon supports. Density function theory (DFT) was used. $Pt_7$ was used for representing Pt nanoparticles while $sp^2$ carbon nanoribbons of zigzag or armchair structures were modelled for the carbon supports. Flat facet and edge represented the low-curvature Vulcan XC-72R (CB) while curved facet was used for describing the high-curvature CNO. (b and c) The optimized structures of a $Pt_7$ cluster adsorbed on flat and curved $sp^2$ carbon nanoribbons. $Pt_7$ nanoparticles on zigzag and armchair nanoribbons (ZZNR and ACNR) were shown in b and c, respectively. The curved nanoribbons were made by curving the corresponding flat nanoribbons along the x-axis. The structures were viewed from the y-axis.

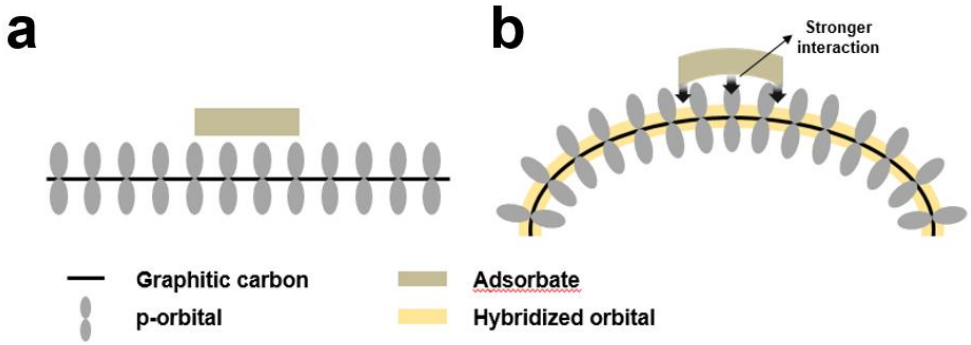


**Figure 2.14**. The schematic representation of the effect of curvature on the adsorption affinity. (A) Planar graphitic carbon system. (B) Curved graphitic carbon system.

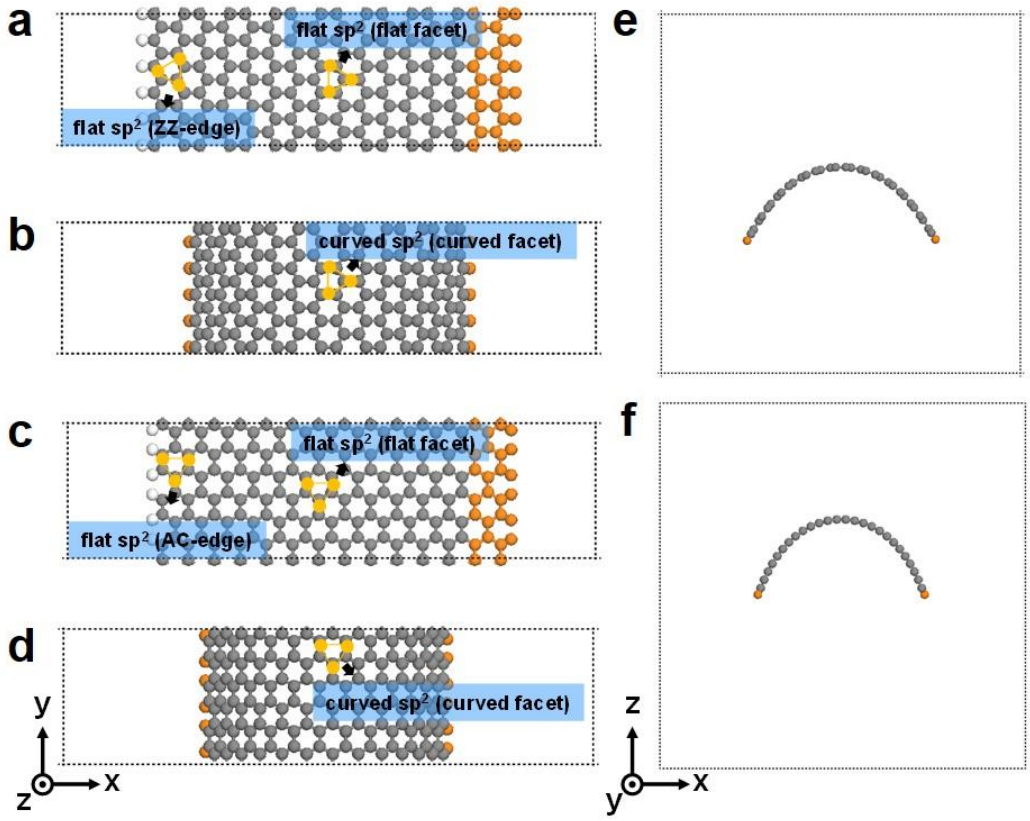


**Figure 2.15.** The optimized structure of carbon nanoribbons. Top views of (a) ZZNR, (b) c-ZZNR, (c) ACNR and (d) c-ACNR, and side views of (e) c-ZZNR and (f) c-ACNR. Note that in (a) and (c) the orange colored atoms were fixed to reduce the distortion of $sp^2$ carbon nanoribbons during the $Pt_7$ adsorption on the other edge. Gray and white spheres indicate carbon and hydrogen atoms, respectively. The orange triangles indicate the adsorption sites for the $Pt_7$ nanoparticle.

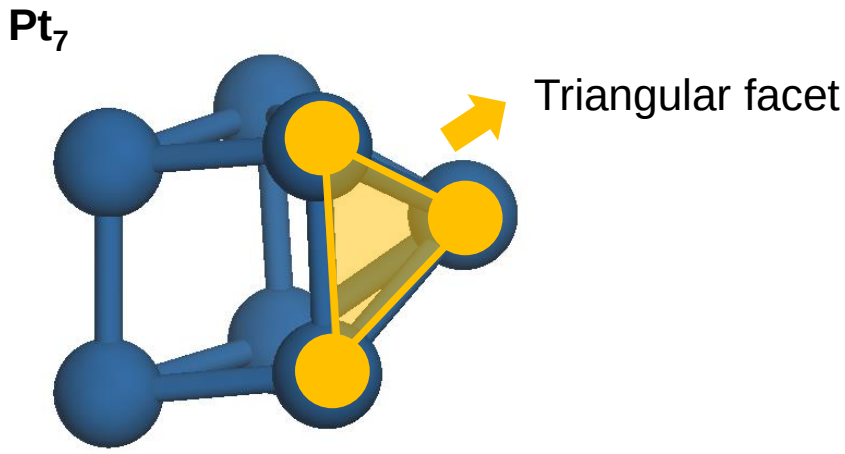


**Figure 2.16.** The optimized structure of $Pt_7$ nanoparticle. Pt atoms were colored navy and the triangular facet, which is the adsorption site of the nanoparticle, was colored orange.

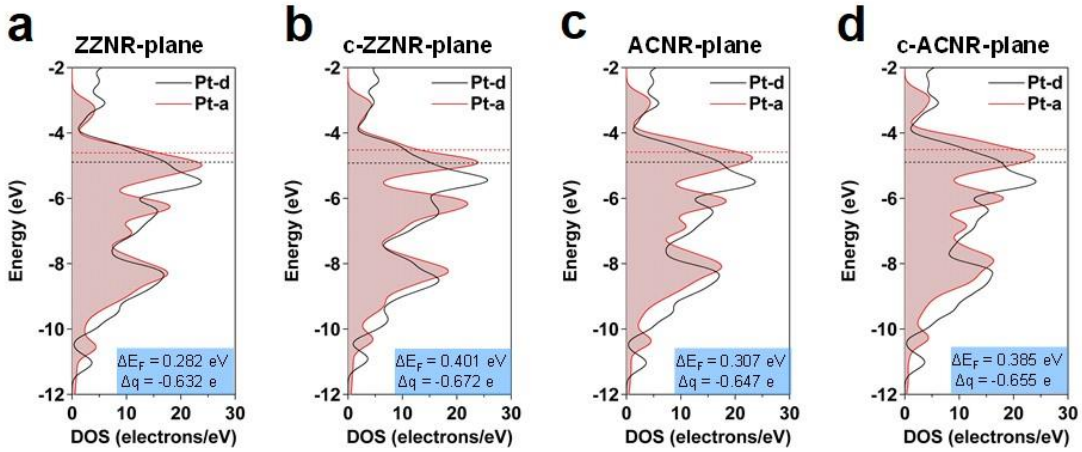


**Figure 2.17.** Density of states (DOS) of $Pt_7$ in adsorbed (Pt-a) and deformed (Pt-d) states. The deformed states were synthesized by removing nanoribbons from $Pt_7$-adsorbed states. (a) ZZNR. (b) c-ZZNR. (c) ACNR. (d) c-ACNR. The dashed lines indicate the Fermi levels ($E_F$) of the states of $Pt_7$. $\Delta E_F$ is difference of Fermi energies between adsorbed and deformed states. $\Delta q$ is the amount of atomic charge transfer from $sp^2$ carbon nanoribbon to $Pt_7$.

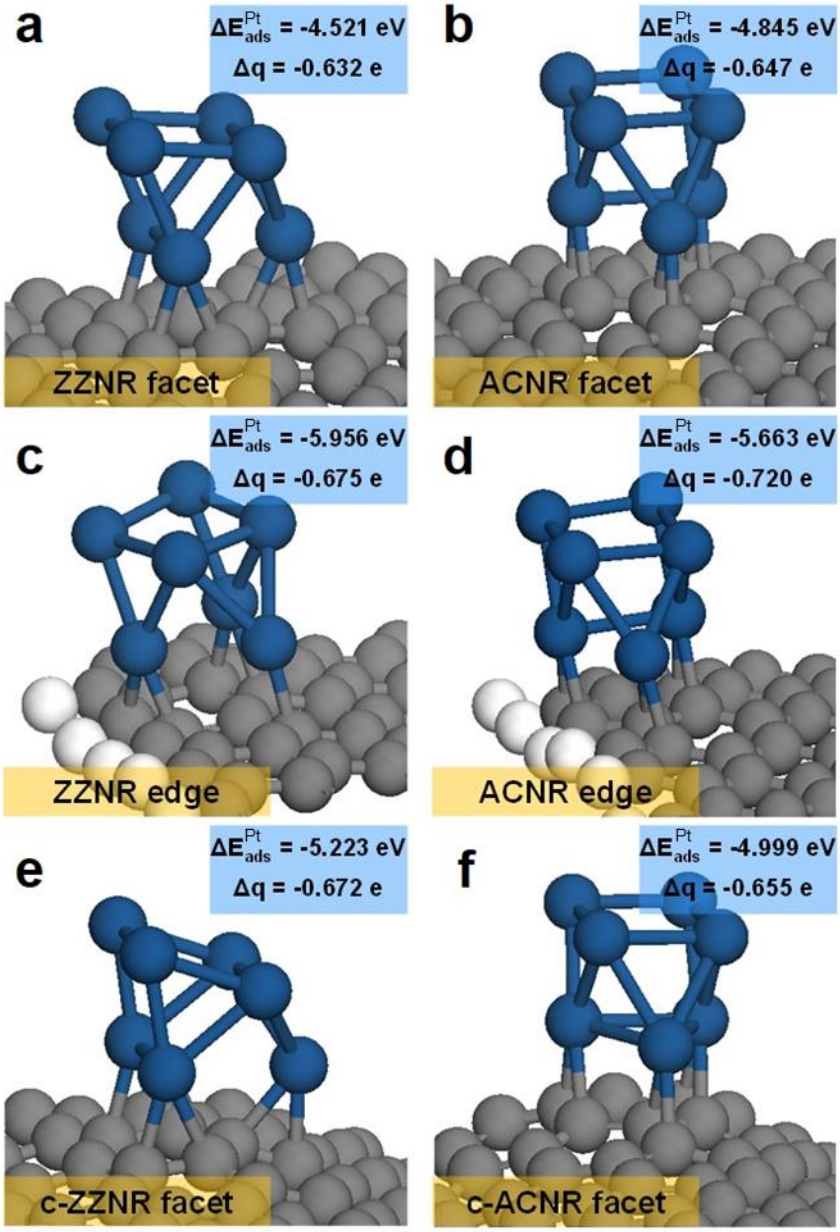


**Figure 2.18.** The optimized structure of adsorbed $Pt_7$ nanoparticle on (a) ZZNR facet, (b) ACNR facet, (c) ZZNR edge, (d) ACNR edge, (e) c-ZZNR facet and (f) c-ACNR facet. $\Delta E_{ads}^{Pt}$ is the adsorption energy of $Pt_7$ nanoparticle and $\Delta q$ is the amount of atomic charge transfer from $sp^2$ carbon nanoribbon to $Pt_7$ nanoparticle. Navy, gray and white spheres indicate Pt, C and H atoms, respectively.

Choice of substrate possibly affects the crystallinity of Pt due to the metal-substrate interaction. The crystallinity of Pt in Pt/CNO was higher than that of its commercial counterpart (Pt/CB), which was indicated by sharper peaks at 39.77, 46.28 and 67.45 degree assigned for (111), (200) and (220) planes of Pt respectively (**Figure 2.6a**). The (111) planes of Pt were dominantly exposed to electrolytes in Pt/CNO (**Figure 2.4b**), which are known to have the highest ORR electroactivities among crystallographic orientations of Pt.[35]

DFT calculation also supported that the strong metal-support interaction of Pt/CNO improved the ORR activity. Oxygen adsorption, the rate-determining step of ORR,[36] was more encouraged on $Pt_7$ attached to the high-curvature CNO (c-ZZNR) than on $Pt_7$ attached to the low-curvature or relatively flat CB (ZZNR) (**Figure 2.19a** and **b**). Adsorption energy of oxygen on $Pt_7$ ($\Delta E_{ads}^{O2}$) decreased from -1.362 eV (ZZNR) to -1.657 eV (c-ZZNR) when the nanoribbon support was curved. Therefore, oxygen adsorption on more negatively charged Pt on CNO is thermodynamically more favored so that Pt/CNO is superior to Pt/CB in ORR electroactivity.

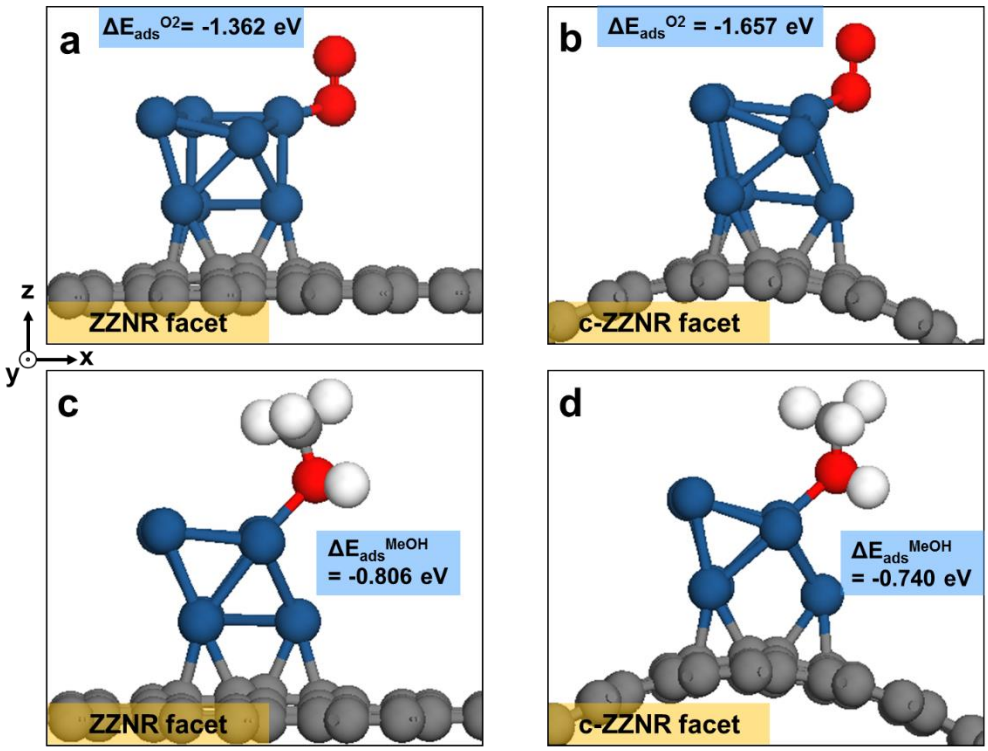


**Figure 2.19. $O_2$ and methanol (MeOH) adsorption on $Pt_7$ attached on flat and curved $sp^2$ carbon nanoribbons.** (a and b) $O_2$ adsorption. (c and d) MeOH adsorption. $Pt_7$ is attached to either flat ZZNR facet or its curved counterpart. $\Delta E_{ads}^{O2}$ and $\Delta E_{ads}^{MeOH}$ is the adsorption energy of $O_2$ and MeOH on $Pt_7$ attached to nanoribbons, respectively.

*2.3.6. The methanol tolerance test for Pt/CNO*

In addition to ORR stability, methanol tolerance was also improved by the use of CNO as Pt supports. Methanol oxidation reaction (MOR) should be suppressed because carbon monoxide generated from MOR increases the viscosity of electrolyte and poisons active sites of platinum catalysts.[37,38] The ORR current (5.32 mA/cm$^2$) of Pt/CB in the alkaline media at 0.729 $V_{RHE}$ decreased seriously to zero immediately after the introduction of 1 M methanol (**Figure 2.20a** for alkaline media and **Figure 2.20b** for acid media). However, only a small change in the ORR current was observed on Pt/CNO. Cyclic voltammograms obtained in the acidic media purged by nitrogen or saturated by oxygen indicated that methanol was easily oxidized in the presence of Pt/CB but the oxidation was significantly suppressed in Pt/CNO (**Figure 2.20d** for acid media and **Figure 2.20c** for alkaline media). A single-atomic Pt catalyst was reported to show excellent MOR resistivity because at least two neighboring Pt atoms are required for the MOR.[39] Introduction of a protective layer such as carbon[40] , polymer[41] and metal[42] to the surface of Pt was helpful for the MOR resistivity. However, it was difficult to find the cases that bare Pt nanocrystals are MOR-resistant. Carbon monoxide poisoning as a result of MOR has not been avoided by using platinum catalysts[43, 44] so that bimetallic catalysts such as Pt-Pd have been presented.[45,46] In our best knowledge, the Pt/CNO is the first carbon-supported bare platinum nanocrystal catalyst showing high performance ORR with MOR tolerance. In the same vein as the ORR stability confirmed by the DFT calculation, the electron-rich phase of platinum induced by electron donation of the CNO to Pt nanoparticle was expected to be responsible for the improved methanol tolerance.

By DFT calculation, it was revealed that methanol (MeOH) adsorption was discouraged on $Pt_7$ attached to the high-curvature CNO (c-ZZNR) when compared with the adsorption on $Pt_7$ attached to the low-curvature or relatively flat surface of Vulcan XC-72R (ZZNR) (**Figure 2.19c and d**). MeOH adsorption on curved nanoribbons was estimated less stable than that on flat ones: the MeOH adsorption energy (versus the state of MeOH in solution) = -0.740 eV for $Pt_7$/c-ZZNR > -0.806 eV for $Pt_7$/ZZNR. More negatively charged Pt on the CNO did not accommodate the MeOH molecules on its surface because the nucleophilic oxygen atom in MeOH[47] is repulsive to electron-sufficient Pt on the CNO.

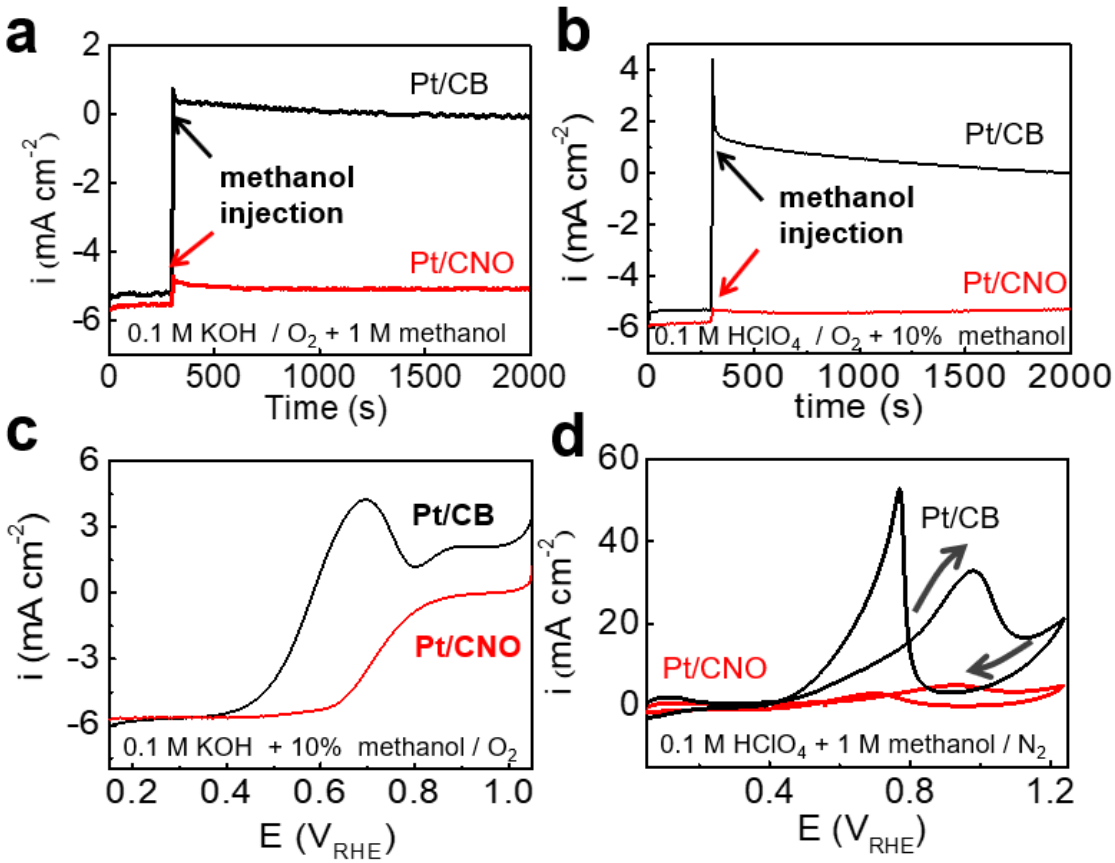


**Figure 2.20. Methanol tolerance.** (a and b) Chronoamperometric responses at 0.729 $V_{RHE}$ in the oxygen- saturated alkaline media with methanol injected at 300 s (1600 rpm). (c) ORR activities in the presence of 10 % methanol (10 mV $s^{-1}$; 1600 rpm) in alkaline media. (d) Cyclic voltammograms at 50 mV $s^{-1}$ in the nitrogen-purged acid media containing 1 M methanol.

*2.3.7. The suppression of thermal oxidation*

Pt/CNO was more resistive to thermal oxidation than Pt/CB even if Pt-unloaded CNO and CB showed the similar onset temperature of severe mass decrease around 600 °C (**Figure 2.21**). The onset temperature of Pt/CNO was 450 °C, which is 100 °C higher than that of Pt/CB. Also, the amount of the initial mass decrease of Pt/CNO below 150 °C was less than that of Pt/CB. The graphene-like concentric layers of CNO would suppress the oxidation catalyzed by platinum. As another feasible explanation on the oxidation resistance, the smaller contact area between Pt nanocrystals and the CNO particles is considered. It is difficult to imagine the hemi-spherical Pt domes sitting on the CNO particles of the same size (2.8 ± 0.83 nm for Pt versus 5.3 ± 1.3 nm for CNO). High curvature of the CNO particles provides inappropriate foundation that Pt atoms that land on. Accordingly, it is more accurate to describe the Pt/CNO composites as the mixture of two components rather than one component dispersed on the other. Therefore, the contact area between Pt nanocrystals and the CNO particles in Pt/CNO would be smaller than that of its practical counterpart Pt/CB where Pt nanocrystals are dispersed on CB. Since carbon oxidation proceeds most probably on the peripheral circumference of the contact between carbon and platinum, less number of active sites to catalyze the oxidation are involved in Pt/CNO than Pt/CB.[1]

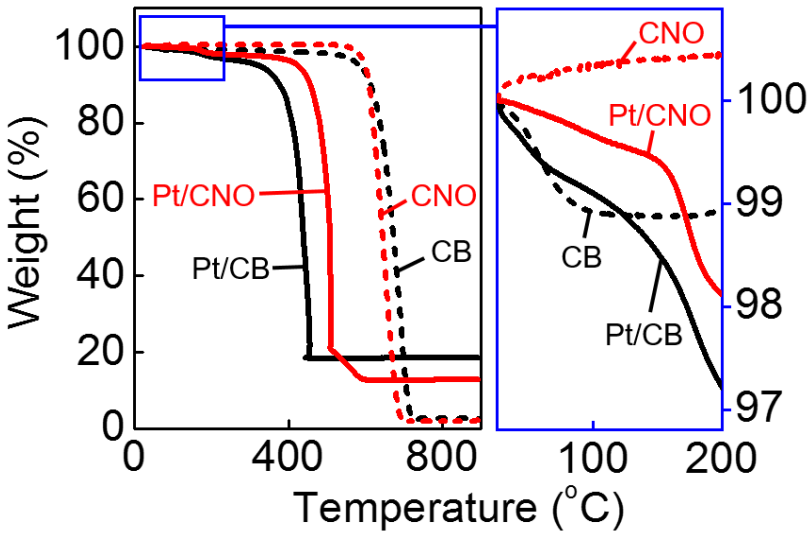


**Figure 2.21.** Thermograms of Pt/CB and Pt/CNO in air. Scan rate = 10 °C $min^{-1}$.

## 2.4. Density functional theory (DFT) calculation

*2.4.1. Computer method*

Density functional theory (DFT) calculation was carried out to investigate the adsorption of $Pt_7$ nanoparticle on Vulcan XC-72R or CNO and adsorption of methanol on the adsorbed $Pt_7$

nanoparticle. All DFT calculations were performed with Dmol$^3$ program,[48] using the generalized gradient approximation (GGA) with the Perdew-Burke-Ernzerhof (PBE) functional.[49] All electron relativistic core treatment was adopted with the numerical polarized basis sets (DNP 4.4). Spin polarized calculations were performed with the smearing value of 0.005 Ha. The Brillouin-zone was sampled by Monkhorst-Pack k-points;[50] 7×7×1 for hexagonal unit cell of graphene and Γ-point (i.e. 1×1×1) for the other systems. The convergence criteria for energy, force, and displacement were set as $1.0\times10^{-5}$ Ha, 0.002 Ha/Å, and 0.005 Å, respectively. The conductor-like screening model[51] (COSMO) was applied to consider the solvent effect of water with the dielectric constant of 78.36.[52] The atomic charge was calculated with Mulliken charge analysis.[53,54]

*2.4.2. Simulation details*

The $sp^2$ carbon nanoribbons of the zigzag or armchair structure were modeled to describe carbon supports (**Figure 2.15**). $Pt_7$ cluster was used as a representative to the Pt nanoparticle (**Figure 2.16**) since it was reported that the seven-atom cluster has the sufficient size to elucidate the adsorption behavior of Pt nanoparticle.[55] Both edge and flat facets of $sp^2$ carbon nanoribbons were considered as the adsorption sites for $Pt_7$ in the low-curvature Vulcan XC-72R and in the high-curvature CNO, curved facet was only considered as the adsorption site (**Figure 2.15**). Zigzag and armchair nanoribbons (ZZNR and ACNR) were constructed on a hexagonal graphene unit cell with the lattice parameter of 2.460 Å. The nanoribbons were modeled to have similar sizes and the number of $sp^2$ carbon atoms, where the edges were hydrogen-terminated. The lattice A and C were set to be 50 Å and 20 Å, respectively, to introduce enough vacuum space to avoid self-interaction of the system and the lattice B of nanoribbons was ~12.5 Å (**Figure 2.15, Table 2.1**). Curved ZZNR and ACNR (c-ZZNR and c-ACNR) were modeled by cutting CNT (20, 20) (diameter 27.12 Å) and CNT (30, 0) (diameter 23.49 Å) respectively while containing similar number of $sp^2$ carbon atoms (**Table 2.1**).

The adsorption energy ( $\Delta E_{ads}$ ) of $Pt_7$ on the surface of the carbon systems is calculated as follows,

$$\Delta E_{ads} = E_{Pt_7+X} - E_{Pt_7} - E_X \quad (1)$$

where $E_{Pt_7+X}$ indicates the total energy of $Pt_7$ adsorbed on $X$ = ZZNR, ACNR, c-ZZNR and c-ACNR, and $E_{Pt_7}$ and $E_X$ indicate the total energies of isolated $Pt_7$ nanoparticle and $X$ = ZZNR, ACNR, c-ZZNR and c-ACNR, respectively. The adsorption energy of $O_2$ and MeOH is calculated as follows,

$$\Delta E_{ads} = E_{Pt_7+X+adsorbate} - E_{adsorbate} - E_{Pt_7+X} \quad (2)$$

where $E_{Pt_7+X+adsorbate}$ is the total energies of adsorbate molecules (i.e. $O_2$ and MeOH) adsorbed on $Pt_7$/nanoribbon complex, and $E_{adsorbate}$ indicates the total energies of isolated adsorbate molecules.

**2.5. Conclusion**

In summary, the CNO spherical nanoparticles of ~ 5 concentric graphitic layers i n 5.3 ± 1.3 nm were synthesized as a support for Pt catalysts. The long-term ORR dur ability of Pt and its methanol tolerance was remarkably improved by the CNO instead o f the conventional counterpart, carbon black. Three factors were responsible for the dura bility. First, the *islands-by-islands* configuration of Pt/CNO isolated each Pt nanoparticle from its neighbours by the same-size CNO particles and suppressed Ostwald ripening by highly tortuous void structure. Second, the high curvature of the CNO nanoparticles ind uced facile and ready electron transfer from CNO to Pt so that the strong interaction be tween the substrate and the catalyst particles confirmed the dispersion stability. Third, th e highly graphitic layers constituting CNO improved corrosion resistivity.

**2.6. Reference**

(1) Maass, S.; Finsterwalder, F.; Frank, G.; Hartmann, R.; Merten, C. Carbon Support Oxidation in PEM Fuel Cell Cathodes. *J. Power Sources* **2008**, *176*, 444-451.

(2) Tang, H.; Qi, Z.; Ramani, M.; Elter, J. F. PEM Fuel Cell Cathode Carbon Corrosion due to the Formation of Air/Fuel Boundary at The Anode. *J. Power Sources* **2006**, *158*, 1306-1312.

(3) Shao-Horn, Y.; Sheng, W. C.; Chen, S.; Ferreira, P. J.; Holby, E. F.; Morgan, D. Instability of Supported Platinum Nanoparticles in Low-Temperature Fuel Cells. *Top. Catal.* **2007**, *46*, 285-305.

(4) Atanassova, P.; Rice, G.; Shen, J.-P.; Sun, Y.; Dowlapalli, M.; Atanassov, P. In Carbon corrosion in fuel cells, Gordon Research Conference on Fuel Cells, Bryant University, Smithfield, RI, USA 2007; Bryant University, Smithfield, RI, USA **2007**.

(5) Dicks, A. L. The Role of Carbon in Fuel Cells. *J. Power Sources* **2006**, *156*, 128-141.

(6) Yano, H.; Akiyama, T.; Watanabe, M.; Uchida, H. High Durability of Pt/Graphitized Carbon Catalysts for Polymer Electrolyte Fuel Cells Prepared by the Nanocapsule Method. *J. Electroanal. Chem.* **2013**, *688*, 137-142.

(7) Wang, Y.-J.; Wilkinson, D. P.; Zhang, J. Noncarbon Support Materials for Polymer Electrolyte Membrane Fuel Cell Electrocatalysts. *Chem. Rev.* **2011**, *111*, 7625-7651.

(8) Choi, W. C.; Woo, S. I.; Jeon, M. K.; Sohn, J. M.; Kim, M. R.; Jeon, H. J. Platinum Nanoclusters Studded in the Microporous Nanowalls of Ordered Mesoporous Carbon. *Adv. Mater.* **2005**, *17*, 446-451.

(9) Kuppan, B.; Selvam, P. Platinum-Supported Mesoporous Carbon (Pt/CMK-3) as Anodic Catalyst for Direct Methanol Fuel Cell Applications: The Effect of Preparation and Deposition Methods. *Prog. Nat. Sci. Mater. Int.* **2012**, *22*, 616-623.

(10) Yu, J.-S.; Kang, S.; Yoon, S. B.; Chai, G. Fabrication of Ordered Uniform Porous Carbon Networks and their Application to a Catalyst Supporter. *J. Am. Chem. Soc.* **2002**, *124*, 9382-9383.

(11) Perini, L.; Durante, C.; Favaro, M.; Perazzolo, V.; Agnoli, S.; Schneider, O.; Granozzi, G.; Gennaro. A. Metal-Support Interaction in Platinum and Palladium Nanoparticles Loaded on Nitrogen-Doped Mesoporous Carbon for Oxygen Reduction Reaction. *ACS Appl. Mater. Interfaces* **2015**, *7*, 1170-1179.

(12) Wang, S.; Jiang, S. P.; White, T. J.; Guo, J.; Wang, X. Electrocatalytic Activity and Interconnectivity of Pt Nanoparticles on Multiwalled Carbon Nanotubes for Fuel Cells. *J. Phys. Chem. C* **2009**, *113*, 18935-18945.

(13) Do, I.; Drzal, L. T. Ionic Liquid-Assisted Synthesis of Pt Nanoparticles onto Exfoliated

Graphite Nanoplatelets for Fuel Cells. *ACS Appl. Mater. Interfaces* **2014**, *6*, 12126-12136.

(14) Melke, J.; Peter, B.; Habereder, A.; Ziegler, J.; Fasel, C.; Nefedov, A.; Sezen, H.; Woll, C.; Ehrenberg, H.; Roth, C. Metal-Support Interactions of Platinum Nanoparticles Decorated N-Doped Carbon Nanofibers for the Oxygen Reduction Reaction. *ACS Appl. Mater. Interfaces* **2016**, *8*, 82-90.

(15) Bommersbach, P.; Chaker, M.; Mohamedi, M.; Guay, D. Physico-Chemical and Electrochemical Properties of Platinum−Tin Nanoparticles Synthesized by Pulsed Laser Ablation for Ethanol Oxidation. *J. Phys. Chem. C* **2008**, *112*, 14672-14681.

(16) Huang, H.; Ma, L.; Tiwary, C. S.; Jiang, Q.; Yin, K.; Zhou, W.; Ajayan, P. M. Worm-Shape Pt Nanocrystals Grown in Nitrogen-Doped Low-Defect Graphene Sheets: Highly Efficient Electrocatalysts for Methanol Oxidation Reaction. *Small* **2017**, *13*, 1603013.

(17) Wang, X. X.; Tan, Z. H.; Zeng, M.; Wang, J. N. Carbon Nanocages: A New Support Material for Pt Catalyst with Remarkably High Durability. *Sci. Rep.* **2014**, *4*, 4437.

(18) Cheng, N.; Norouzi Banis, M.; Liu, J.; Riese, A.; Mu, S.; Li, R.; Sham, T.-K.; Sun, X. Atomic Scale Enhancement of Metal-Support Interactions between Pt and ZrC for Highly Stable Electrocatalysts. *Energy Environ. Sci.* **2015**, *8*, 1450-1455.

(19) Xie, X.; Chen, S.; Ding, W.; Nie, Y.; Wei, Z. An Extraordinarily Stable Catalyst: Pt NPs Supported on Two-Dimensional $Ti_3C_2X_2$ (X = OH, F) Nanosheets for Oxygen Reduction Reaction. *Chem. Commun.* **2013**, *49*, 10112-4.

(20) Tian, X.; Luo, J.; Nan, H.; Zou, H.; Chen, R.; Shu, T.; Li, X.; Li, Y.; Song, H.; Liao, S.; Adzic, R. R. Transition Metal Nitride Coated with Atomic Layers of Pt as a Low-Cost, Highly Stable Electrocatalyst for Oxygen Reduction Reaction. *J. Am. Chem. Soc.* **2016**, *138*, 1575-1583.

(21) McDonough, J. K.; Gogotsi, Y. Carbon Onions: Synthesis and Electrochemical Applications. *Electrochem. Soc. Interface* **2013**, *22*, 61-66.

(22) Giovannetti, G.; Khomyakov, P. A.; Brocks, G.; Karpan, V. M.; van den Brink, J.; Kelly, P. J. Doping Graphene with Metal Contacts. *Phys. Rev. Lett.* **2008**, *101*, 026803.

(23) Kim, G.; Jhi, S.-H. Carbon Monoxide-Tolerant Platinum Nanoparticle Catalysts on Defect-Engineered Graphene. *ACS Nano* **2011**, *5*, 805-810.

(24) Goh, Y. A.; Chen, X.; Yasin, F. M.; Eggers, P. K.; Boulos, R. A.; Wang, X.; Chua, H. T.; Raston, C. L. Shear Flow Assisted Decoration of Carbon Nano-Onions with Platinum Nanoparticles. *Chem. Commun.* **2013**, *49*, 5171-5173.

(25) Portet, C.; Yushin, G.; Gogotsi, Y. Electrochemical Performance of Carbon Onions, Nanodiamonds, Carbon Black and Multiwalled Nanotubes in Electrical Double Layer Capacitors. *Carbon* **2007**, *45*, 2511-2518.

(26) McDonough, J. K.; Frolov, A. I.; Presser, V.; Niu, J.; Miller, C. H.; Ubieto, T.; Fedorov, M. V.; Gogotsi, Y. Influence of the Structure of Carbon Onions on their Electrochemical Performance in Supercapacitor Electrodes. *Carbon* **2012**, *50*, 3298-3309.

(27) Kotakoski, J.; Krasheninnikov, A. V.; Kaiser, U.; Meyer, J. C. From Point Defects in Graphene to Two-Dimensional Amorphous Carbon. *Phys. Rev. Less.* **2011**, *106*, 105505.

(28) Tachikawa, H.; Shimizu, A. Diffusion Dynamics of the $Li^+$ Ion in a Model Surface of Amorphous Carbon: A Direct Molecular Orbital Dynamics Study. *J. Phys. Chem. B* **2005,** *109*, 13255-13262.

(29) Tachikawa, H.; Shimizu, A. Diffusion Dynamics of the Li Atom on Amorphous Carbon: A Direct Molecular Orbital-Molecular Dynamics Study. *J. Phys. Chem. B*, **2006**, *110*, 20445-20450.

(30) Saito, R.; Fujita, M.; Dresselhaus, G.; Dresselhaus, M. S. Electronic Structure of Graphene Tubules Based on $C_{60}$. *Phys. Rev. B* **1992**, *46*, 1804-1811.

(31) Zhang, J.; Ong, K. P.; Wu, P. The Influence of Out-of-Plane Deformation on the Band Gap of Graphene Nanoribbons. *J. Phys. Chem. C* **2010**, *114*, 12749-12753.

(32) Escaño, M.C.S. First-Principles Calculations of the Dissolution and Coalescence Properties of Pt Nanoparticle ORR Catalysts: The Effect of Nanoparticle Shape. *Nano Res.* **2015**, *8*, 1689-1697.

(33) Sanz-Navarro, C. F.; Åstrand, P.-O.; Chen, D.; Rønning, M.; van Duin, A. C.T.; Jacob, T.; Goddard, W. A. Molecular Dynamics Simulations of the Interactions between Platinum Clusters and Carbon Platelets. *J. Phys. Chem. A* **2008**, *112*, 1392-1402.

(34) Coloma, F.; Sepulveda-Escribano, A.; Rodriguez-Reinoso, F. Heat-Treated Carbon Blacks as Supports for Platinum Catalysis. *J. Catal.* **1995**, *154*, 299-305.

(35) Nørskov, J. K.; Rossmeisl, J.; Logadottir, A.; Lindqvist, L.; Kitchin, J. R.; Bligaard, T.; Jónsson, H. Origin of the Overpotential for Oxygen Reduction at a Fuel-Cell Cathode. *J. Phys. Chem. B* **2004**, *108*, 17886-17892.

(36) Yeager, E.; Razaq, M.; Gervasio, D.; Razaq, A.; Tryk, D. The Electrolyte Factor in $O_2$ Reduction Electrocatalysis. *Proc. Electrochem. Soc.* **1992**, *92-11*, 440–473.

(37) Larminie, J.; Dicks, A.; Larminie, J.; Dicks, A. *Proton Exchange Membrane Fuel Cells.* In *Fuel Cell Systems Explained*, John Wiley & Sons: 2013; pp 67-119.

(38) Larminie, J.; Dicks, A.; Larminie, J.; Dicks, A. *Alkaline Electrolyte Fuel Cells.* In *Fuel Cell Systems Explained*, John Wiley & Sons: 2013; pp 121-139.

(39) Kamiya, K.; Kamai, R.; Hashimoto, K.; Nakanishi, S. Platinum-Modified Covalent Triazine Frameworks Hybridized with Carbon Nanoparticles as Methanol-Tolerant Oxygen Reduction Electrocatalysts. *Nat. commun.* **2014**, *5*, 5040.

(40) Song, W.; Chen, Z.; Yang, C.; Yang, Z.; Tai, J.; Nan, Y.; Lu, H. Carbon-Coated, Methanol-Tolerant Platinum/Graphene Catalysts for Oxygen Reduction Reaction with Excellent Long-Term Performance. *J. Mater. Chem. A* **2015**, *3*, 1049-1057.

(41) Yang, Z.; Nakashima, N. A Simple Preparation of Very High Methanol Tolerant Cathode Electrocatalyst for Direct Methanol Fuel Cell Based on Polymer-Coated Carbon Nanotube/Platinum. *Sci. Rep.* **2015**, *5*, 12236.

(42) Abrego-Martinez, J. C.; Wang, Y.; Ledesma-Garcia, J.; Cuevas-Muniz, F. M.; Arriaga, L. G.; Mohamedi, M. A Pulsed Laser Synthesis of Nanostructured Bi-Layer Platinum-Silver Catalyst for Metanol-Tolerant Oxygen Reduction Reaction. *Int. J. Hydrogen Energy,* **2017**, *42*, 28056-28062.

(43) Antolini, E.; Lopes, T.; Gonzalez, E. R. An Overview of Platinum-Based Catalysts as Methanol-Resistant Oxygen Reduction Materials for Direct Methanol Fuel cells. *J. Alloys Compd.* **2008**, *461*, 253-262.

(44) Sharma, S.; Ganguly, A.; Papakonstantinou, P.; Miao, X.; Li, M.; Hutchison, J. L.; Delichatsios, M.; Ukleja, S. Rapid Microwave Synthesis of CO Tolerant Reduced Graphene Oxide-Supported Platinum Electrocatalysts for Oxidation of Methanol. *J. Phys. Chem. C* **2010**, *114*, 19459-19466.

(45) Yang, J.; Lee, J. Y.; Zhang, Q.; Zhou, W.; Liu, Z. Carbon-Supported Pseudo-Core–Shell Pd–Pt Nanoparticles for ORR with and without Methanol. *J. Electrochem. Soc.* **2008**, *155*, B776-B781.

(46) Choi, B.; Nam, W. H.; Chung, D. Y.; Park, I. S.; Yoo, S. J.; Song, J. C.; Sung, Y. E. Enhanced Methanol Tolerance of Highly Pd rich Pd-Pt Cathode Electrocatalysts in Direct Methanol Fuel Cells. *Electrochim. acta* **2015**, *164*, 235-242.

(47) Fuentealba, P.; Pérez, P.; Contreras, R. On the Condensed Fukui Function. *J. Chem. Phys.* **2000**, *113*, 2544-2551.

(48) Kresse, G.; Hafner, J. *Ab Initio* Molecular Dynamics for Liquid Metals. *Phys. Rev. B* **1993**, *47*, 558-561.

(49) Perdew, J. P.; Burke, K.; Ernzerhof, M. Generalized Gradient Approximation Made Simple. *Phys. Rev. Lett.* **1996**, *77*, 3865-3868.

(50) Monkhorst, H. J.; Pack, J. D. Special Points for Brillouin-Zone Integrations. *Phys. Rev. B* **1976**, *13*, 5188-5192.

(51) Delley, B. The Conductor-Like Screening Model for Polymers and Surfaces. *Mol. Simul.* **2006**, *32*, 117-123.

(52) Fattebert, J.-L.; Gygi, F. Density Functional Theory for Efficient *Ab Initio* Molecular Dynamics Simulations in Solution. *J. Comput. Chem.* **2002**, *23*, 662-666.

(53) Mulliken, R. S. Electronic Population Analysis on LCAO-MO Molecular Wave Functions. I. *J. Chem. Phys.* **1955**, *23*, 1833-1840.

(54) Mulliken, R. S. Electronic Population Analysis on LCAO-MO Molecular Wave Function. IV. Bonding and Antibonding in LCAO and Valence-Bond Theories. *J. Chem. Phys.* **1955**, *23*, 2343-2346.

(55) Lin, K.-H.; Sun, C.; Ju, S.-P.; Smith, S. C. Density Functional Theory Study on Adsorption of Pt Nanoparticle on Graphene. *Int. J. Hydrogen Energy* **2013,** *38*, 6283-6287.

(56) Obraztsova, E. D.; Fujii, M.; Hayashi, S.; Kuznetsov, V. L.; Butenko, Y. V.; Chuvilin, A. L. Raman Identification of Onion-Like Carbon. *Carbon* **1998**, *36*, 821-826.

(57) Dresselhaus, M. S.; Dresselhaus, G.; Hofmann, M. The Big Picture of Raman Scattering in Carbon Nanotubes. *Vib. Spectro.* **2007**, *45*, 71-81.

(58) Ferrari, A. C. Raman Spectroscopy of Graphene and Graphite: Disorder, Electron-Phonon Coupling, Doping and Nonadiabatic. *Solid State Commun.* **2007**, *143*, 47-57.

** Chapter 2 is reproduced in part with permission of "**Juchan Yang**, Su Hwan Kim, Sang Kyu Kwak* and Hyun–Kon Song*, Curvature-Induced Metal-Support Interaction of an Islands-by-Islands Composite of Platinum Catalyst and Carbon Nano-onion for Durable Oxygen Reduction, ACS Applied Materials & Interfaces, 9, (2017) 23302-23308". Copyright © 2017 American Chemical Society.*

# Chapter 3: Sphere-to-multipod transmorphic change of nanoconfined platinum electrocatalyst during oxygen reduction reaction

## 3.1. Introduction

Oxygen reduction reaction (ORR) is the cathodic process of fuel cells and metal air batteries. Pt has been considered as the electrocatalyst exhibiting the highest ORR electroactivity. In spite of its superior intrinsic activity, Pt nanoparticles (practically around 5 nm) supported by carbon (Pt/C) suffers from unsatisfied durability during practical fuel cell operations[1]. The main causes have been considered to be (1) active area loss by Pt agglomeration[2] via Ostwald ripening (dissolution and re-deposition)[3] and/or surface migration along carbon support surface[4-6] and (2) active mass loss due to carbon corrosion[7, 8].

The durability of Pt/carbon systems has been improved by support-side approaches including controlling graphitic characteristics as well as nanostructuring carbon materials[9]. Carbon black of Pt/C was replaced by various nanostructured and/or graphitic carbon materials including an ordered hierarchical nanostructured carbon (OHNC)[10], multiwall carbon nanotubes (MWCNTs)[11], carbon nano-onions (CNOs) in an island-by-island configuration[12], an ordered mesoporous carbon[13] and carbon shells[14, 15]. The corrosion-resistive nature of graphitic carbons suppressed the carbon corrosion[9, 11, 12] while the tortuous void or pore structures of nanostructured carbons discouraged Pt agglomeration[16].

To address the ORR durability issues of the conventional Pt/C catalyst, we confined Pt nanoparticles within nano-holes of graphene to block surface migration and restrict diffusion length of dissolved Pt ions in Ostwald ripening. Holey crumpled reduced graphene oxide (hCR-rGO)[17, 18] was prepared and used as the support for Pt. As expected, the durability of ORR activity of Pt was significantly improved in the nanoconfined situation. Unexpectedly and interestingly, we found that the nanoconfined Pt particles in a spherical shape was evolved to dendritic multi-pods as oxygen reduction was repeated.

**3.2. Experimental section**

*3.2.1. Graphene oxide (GO)*

GO was prepared from purified natural graphite (SP-1, Bay Carbon) using the m odified Hummers method. Graphite powder (2.0 g) was added to concentrated $H_2SO_4$ (4 6 ml), and $KMnO_4$ (6.0 g) was added gradually with stirring and cooling, while the te mperature of the mixture was maintained below 20 °C. The mixture was then stirred at 35 °C for 2 h, and distilled water (92 ml) was added. After 15 min, the reaction was t erminated by the addition of a large amount of distilled water (280 ml) and a 30% $H_2O_2$ solution (5.0 ml), after which the color of the mixture changed from black to bright yellow. The mixture was centrifuged at 4000 rpm and washed with a 1:10 HCl solution (500 ml) in order to remove metal ions. The graphite oxide product was suspended in d istilled water producing a viscous, brown dispersion, which was subjected to dialysis to completely remove metal ions and acids. To obtain the GO dispersion, the graphite oxid e was exfoliated by ultrasonication (Sonic Dismembrator Model 500, Fisher Scientific) at 100 W for 15 min and then centrifugation at 4000 rpm for 10 min.

*3.2.2. Pt-loaded reduced GO (Pt/FL-rGO)*

The colloidal mixture of GO and $H_2PtCl_6{\cdot}6H_2O$ were prepared and their weight r atio was 1:0.5 with the concentration of GO in colloidal mixture fixed at 0.5 mg/ml. T hen, the mixture was poured into a glass Petri dish with a diameter of 9.5 cm and a d epth of 1.6 cm, and incubated at 80 °C for 24 h. The GO/$H_2PtCl_6{\cdot}6H_2O$ film was caref ully peeled off from the glass dish. Then, FL-RGO/Pt was fabricated by followed therm al annealing at 900 °C (ramp: 5 °C/min) in a vacuum for 3 hr.

*3.2.3. Crumpled rGO (CR-rGO)*

GO dispersion was atomized through a 7.0 μm nozzle of a spray dryer (Buchi B-90) to micrometer-size droplets by 30 mbar. The droplets were dried by hot air at 120 °C. The dry powders were settled by a cyclone separator to remove tiny particles. The powders were thermally annealed at 900 °C in a ramp of 5 °C $min^{-1}$ in vacuum for 3 h.

*3.2.4. Pt-loaded holey CR-rGO (Pt/hCR-rGO)*

The colloidal mixture of GO and $H_2PtCl_6{\cdot}6H_2O$ were used as starting materials for porous and crumpled rGO-supported Pt catalyst, and their weight ratio was 1 : 0.5 with the concentration of GO in colloidal mixture fixed at 0.5 mg ml-1. Then, crumpled rGO/Pt was fabricated by the spray dryer (Buchi B-90 spray dryer) followed by thermal annealing at 900 °C (ramp: 5 °C /min)

in a vacuum for 3 hr. In this process, micrometer-sized droplets of dispersion were produced by the atomizer (nozzle in 7.0 μm) of the spray dryer. The droplets were carried away and dried by inflow warm air (120 °C) to produce powder particles. The dry powders were settled by a cyclone separator and the air was discharged from the separator along with small particles. The atomizer pressure was about 30 mbar and the hot air temperature was 120 °C. In all experiments, 30-40 % of the spray rate was used for spraying the dispersions.

The porous crumpled rGO/Pt samples were prepared in a single-step air oxidation process by directly heating the starting crumpled rGO/Pt sample in static air at an elevated temperature in an open-ended tube furnace. The samples were prepared at 350 °C and held for 3 h, and then, thermally reduced at 900 °C (ramp: 5 °C/min) in a vacuum for 3 h to remove oxidized carbon in rGO.

*3.2.5. Electrochemical measurements*

Cyclic voltammetry (CV) as well as linear sweep voltammetry (LSV) for ORR measurements were conducted by a potentiostat (BioLogic VMP 3). Three-electrode systems were configured with graphite rod as a counter electrode and a commercial Hg/HgO for alkaline media or a commercial Ag/AgCl (3 M KCl) for acid media as a reference electrode. Aqueous solution of 0.1 M KOH or $HClO_4$ was used as electrolyte. The rotating ring disk electrodes (RRDEs) were polished consecutively with two different alumina powders (0.3 and 0.05 μm) and cleaned by 20 min sonication in deionized water for removing alumina powders from electrodes. 20 mg of catalyst powders was dispersed in a mixture of 900 μl of ethanol and 100 μl of 5 wt. % nafion suspension in alcohol (Sigma- Aldrich) by sonication for 30 min. 6 μl droplet of the catalyst ink placed on disk of polished RRDEs was dried in an oven at 80 °C for 5 min to evaporate solvent. Electrolytes were purged with nitrogen for measuring the background currents while they were saturated by oxygen for measuring ORR currents. All potentials were reported versus reversible hydrogen electrode (RHE) ($V_{RHE}$ = V versus RHE).

*3.2.6. Physicochemical characterization*

TEM characterization. BFTEM images were acquired by a JEOL JEM 2100F at an accelerating voltage of 200 kV. Atomic-resolution TEM images were performed by using a FEI Titan$^3$ G2 60-300 equipped with a double-side spherical aberration corrector at an accelerating voltage of 80 kV. Change in binding energy of Pt after durability test was measured by X-ray photoelectron spectroscopy (XPS; Thermo Scientific K-Alpha using a monochromic Al Kα X-ray source). X-ray absorption fine spectra (XAFS) were inv

estigated by the Beamline 6D of the Pohang Accelerator Laboratory (PAL) at 3 GeV be am energy and 300 mA currents. Diffraction patterns of the samples were collected on a Bruker D8 advance diffractometer using Cu-Kα radiation (40 kV, 40 mA). Samples w ere scanned over a 2θ range 10-80° in a step scan for 0.05°/step. Thermogravimetric ana lysis (TGA) of the samples was conducted on a Thermal Analysis TA Q500 instrument. The experiment was performed at a temperature range of 25 – 800 ℃ with a heating ra te of 10 ℃ $min^{-1}$ in constant airflow.

### 3.3. Results and discussion

*3.3.1. Nanoconfined Pt electrocatalyst*

Morphology of reduced graphene oxide (rGO) was tuned from flat (FL) to crumpled (CR) to holey (h) (**Figure 3.2**) in order to control Pt-to-Pt distances ($d_{Pt\text{-}Pt}$) for mitigating Pt agglomeration (**Figure 3.1**). It is easily expected that holey crumpled rGO (hCR-rGO) have the longest $d_{Pt\text{-}Pt}$, followed by crumpled rGO without holes (CR-rGO) and then normal rGO (FL-rGO). FL-rGO was crumpled to be CR-rGO via an aerosol spray drying process at 120 °C. The crumpling of GO nanosheets is driven by the capillary force associated with rapid solvent loss[19]. The CR-rGO was catalytically pitted to be hCR-rGO by annealing Pt-loaded CR-rGO at 350 °C. Carbon mass was corroded at the interface between Pt and carbon. Resultantly, Pt particles were loaded and confined in holes during the pitting process. The size of holes was around 10 nm, which corresponded to the size of Pt particles (**Figure 3.3c**). A single Pt nanoparticle is thought to be nano-confined within a hole even if several particles were often found in an open space resulting from interconnected holes (**Figure 3.3**).

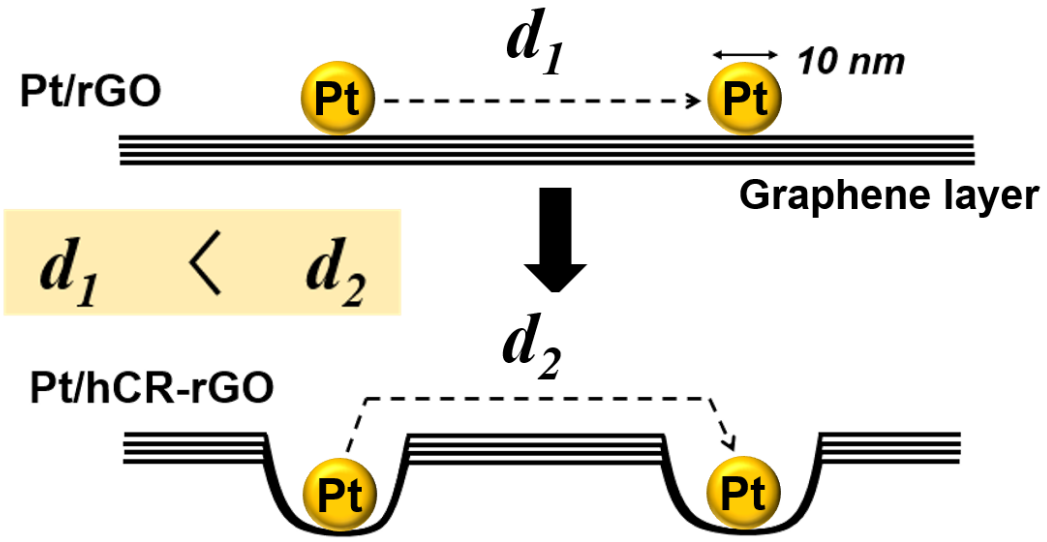


**Figure 3.1.** Pt-to-Pt distances ($d_{Pt\text{-}Pt}$) along which Pt travels during surface migration.

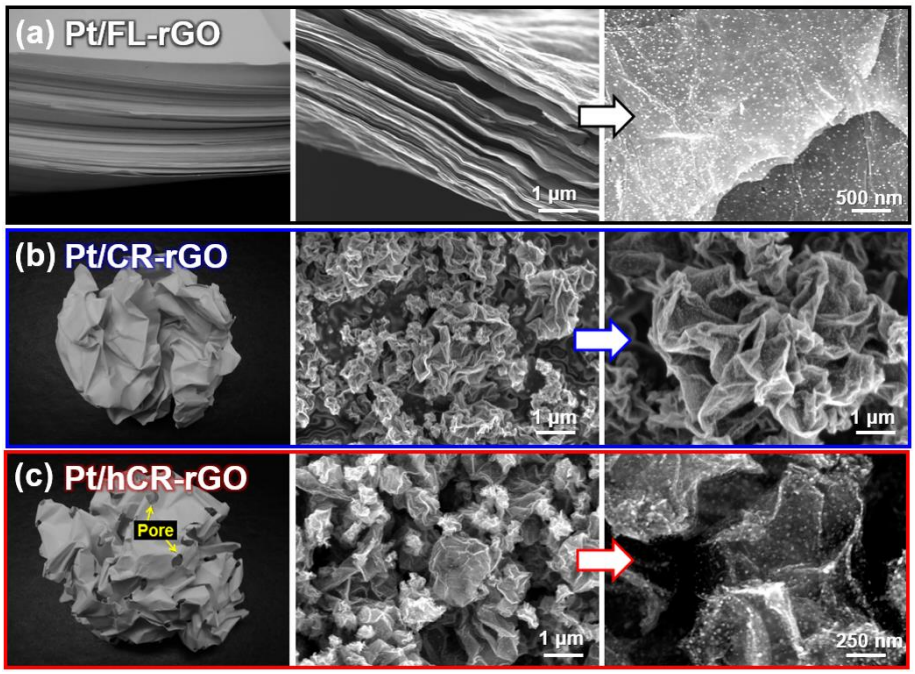


**Figure 3.2. SEM image of holey graphene.** (a to c) Morphologically tuned reduced graphene oxides (rGO) containing Pt particles on their surface. FL = flat; CR = crumpled; hCR = holey crumpled. Paper models on left; SEM images on center; SEM images of Pt-loaded rGO on right

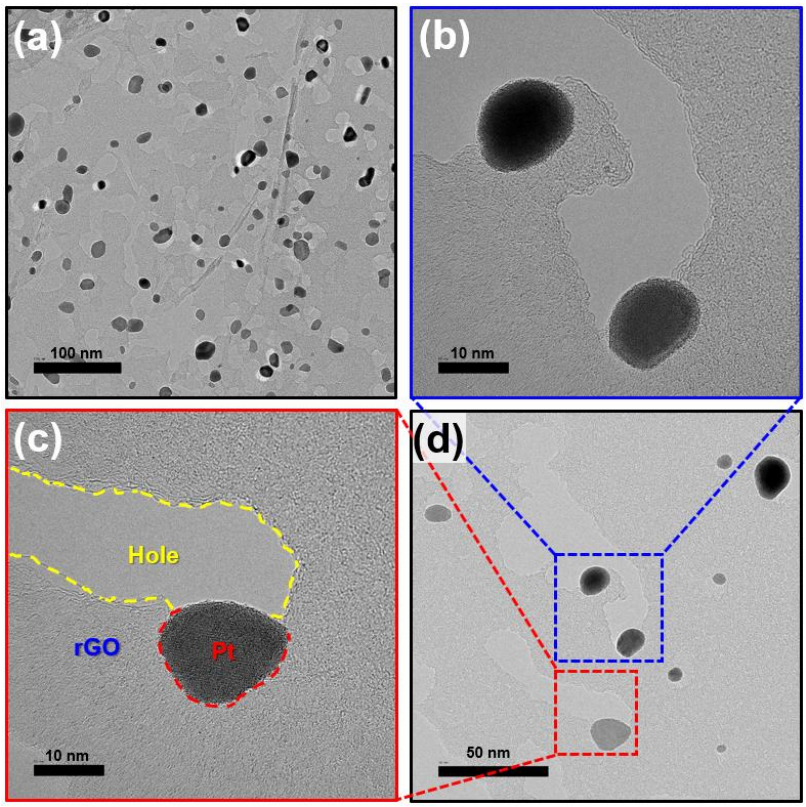


**Figure 3.3.** Isolated loading of Pt nanoparticles in hCR-rGO. (a to d) TEM images.

After crumpling and then pitting, the characteristic XRD peak of graphite (002) at 25° was reduced in intensity and broadened (Left of **Figure 3.4a**)[20]. Pt crystallites were identified by three diffraction peaks of Pt (111) at 40°, (200) at 46° and (220) at 68° (JCPDS card: 04-0802) (right of **Figure 3.4a**). Pt loadings of both samples were estimated at 20 wt. % by thermogravimetric analysis (TGA; **Figure 3.4b**). Pt/hCR-rGO was more resistive to thermal oxidation than commercial Pt/C probably due to the more graphitic characteristics of rGO than carbon black (Vulcan XC-72R) of Pt/C.

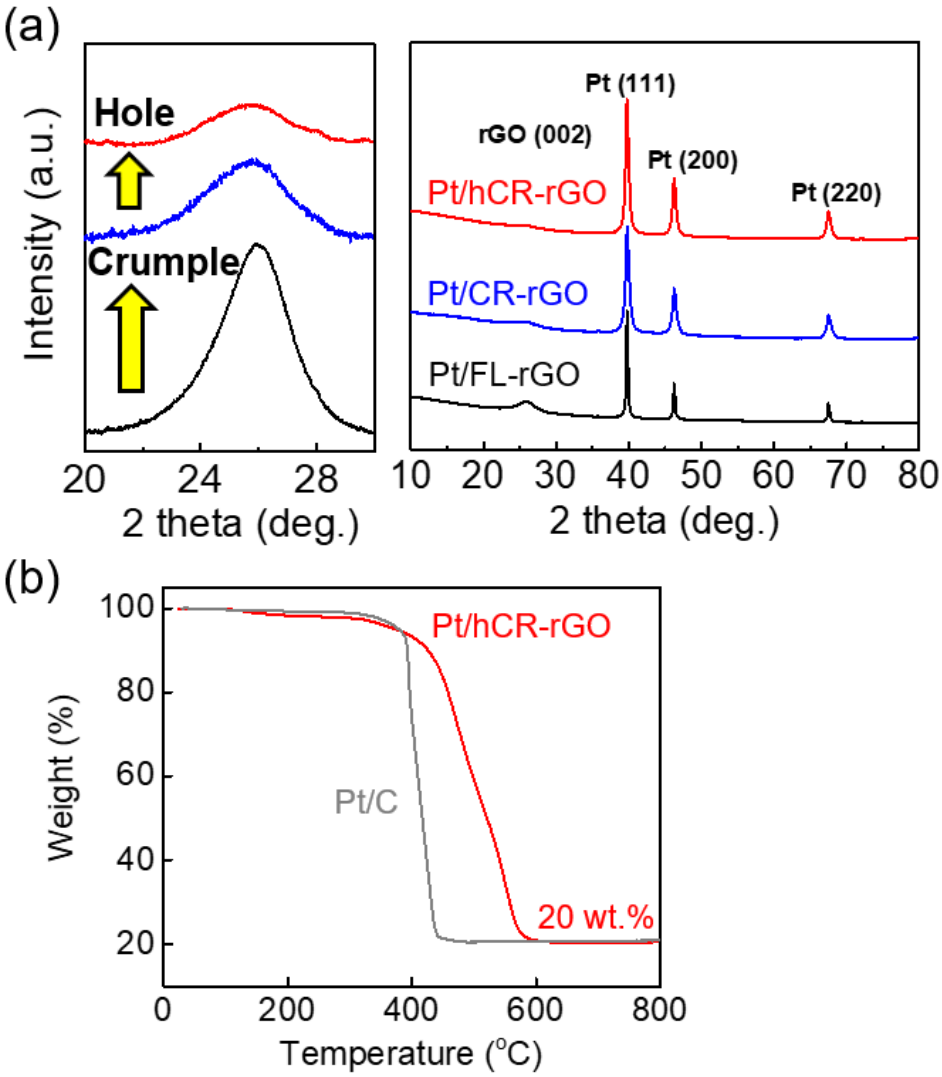


**Figure 3.4. Identification of Pt-loaded graphenes.** (a) X-ray diffraction (XRD) spectra. (b) Thermograms in air at 10 min °C$^{-1}$. The same amount of Pt was loaded on both samples.

*3.3.2. ORR activity and ORR durability*

The ORR electroactivities of Pt/hCR-rGO in comparison with its practical counterpart Pt/C were studied in both alkaline and acidic electrolytes (0.1 M KOH (aq) in **Figure 3.5a** and 0.1 M $HClO_4$ (aq) in **Figure 3.5b**). There were no significant differences in ORR polarization observed between Pt/hCR-rGO and Pt/C at the 1st scan (dotted lines in **Figure 3.5a and b**). After repeated scans (e.g., 10,000 times), however, their ORR electroactivities were confirmed different. Pt/hCR-rGO showed insignificant change or slight improvement in polarization at the 10,000th cycle (red solid). On the contrary, significant overpotentials were developed in Pt/C along cycles (black solid). Also, our Pt/hCR-rGO was superior to Pt/C at potentiostatic oxygen reduction at 0.63 $V_{RHE}$ (**Figure 3.5c**). Higher currents as well as smaller current decrease along time were obtained from Pt/hCR-rGO.

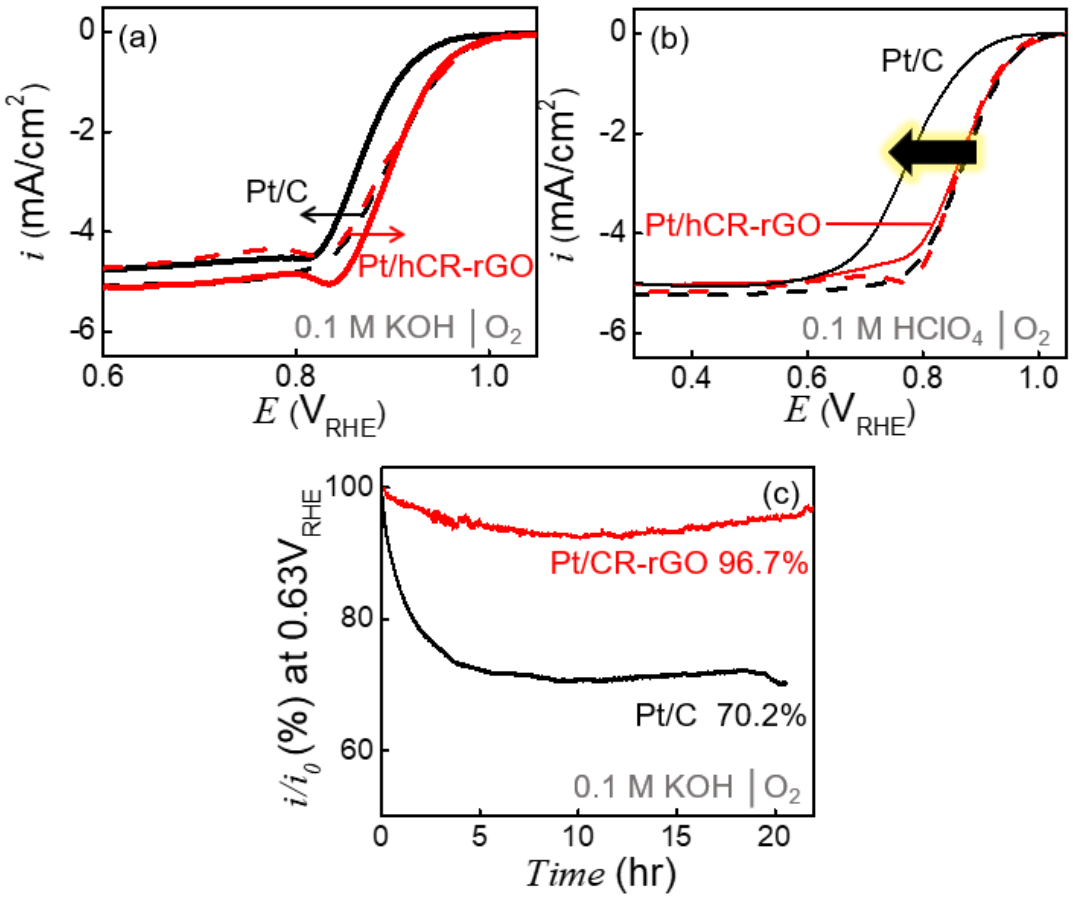


**Figure 3.5. ORR activity and durability.** Electrolytes and purge gases were indicated in plots. (a and b) Polarization curves (10 mV $s^{-1}$; 1600 rpm) obtained from the 1st (dotted) and 10,000th (solid) cycles of potential sweep. (c) Chronoamperometric responses at -0.63 $V_{RHE}$ on 1600 rpm with 1600 rpm in oxygen saturated 0.1 M KOH.

*3.3.3. Electrochemical surface area*

Cyclic voltammograms (CVs) in nitrogen-purged acid media supported hCR-rGO (**Figure 3.6a**) rather than practical carbon substrate (**Figure 3.6b**) for activity durability. Interestingly, electrochemical surface area (ECSA) of Pt/hCR-rGO, estimated by area of peaks relevant to hydrogen underpotential deposition (0.3 $V_{RHE}$ to -0.07 $V_{RHE}$) in CVs, clearly increased with cycles, which contrasts to the serious ECSA decrease of Pt/C.

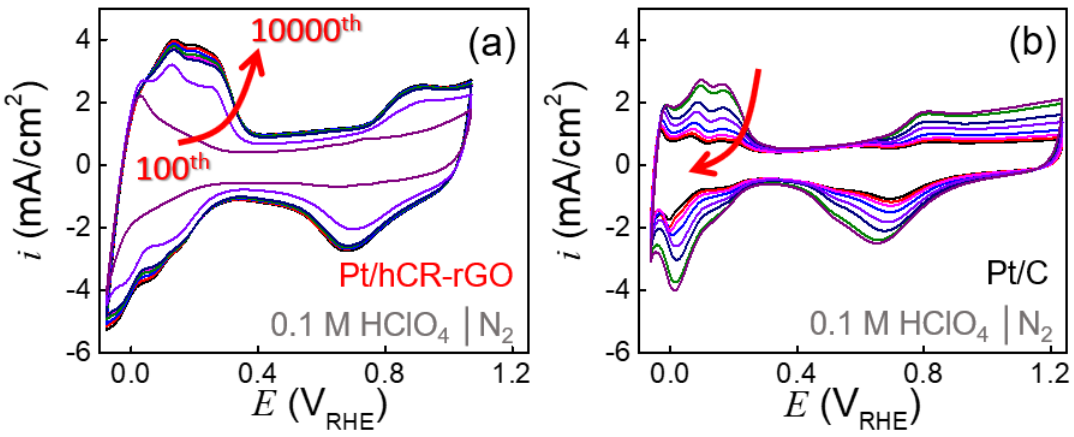


**Figure 3.6. The change of electrochemical surface area (ECSA).** (a and b) 10,000-repeated cyclic voltammograms at 50 mV $s^{-1}$ of Pt/hCR-rGO (a) and its control counterpart, Pt/C (b).

*3.3.4. Methanol tolerance test*

Methanol tolerance, which should be guaranteed for low-temperature fuel cells, was also improved by the use of hCR-rGO as Pt support. Severe methanol oxidation reaction (MOR) current was measured on Pt/C at 0.63 $V_{RHE}$ when 1 M methanol was injected (**Figure 3.7a and b** for alkaline and acidic media, respectively). Much smaller MOR current was obtained on Pt/hCR-rGO in the same condition. Cyclic voltammograms confirmed the chronoamperometric responses (**Figure 3.7c**). MOR proceeds during the anodic scan of potential (forward scan; the peak current of MOR = $i_f$), generating CO and/or $CO_2$. Then, the CO adsorbed on Pt ($CO_{ads}$) is oxidized during the backward scan (the peak current of $CO_{ads}$ oxidation = $i_b$). The ratio of $i_f$ to $i_b$ ($i_f$ / $i_b$) can be used as a measure of CO poisoning. Higher values of $i_f$ / $i_b$ support less serious CO poisoning: $i_f$ / $i_b$ = 1.21 for Pt/hCR-rGO and 0.73 for Pt/C. Therefore, Pt/hCR-rGO is superior to Pt/C in terms of methanol tolerance.

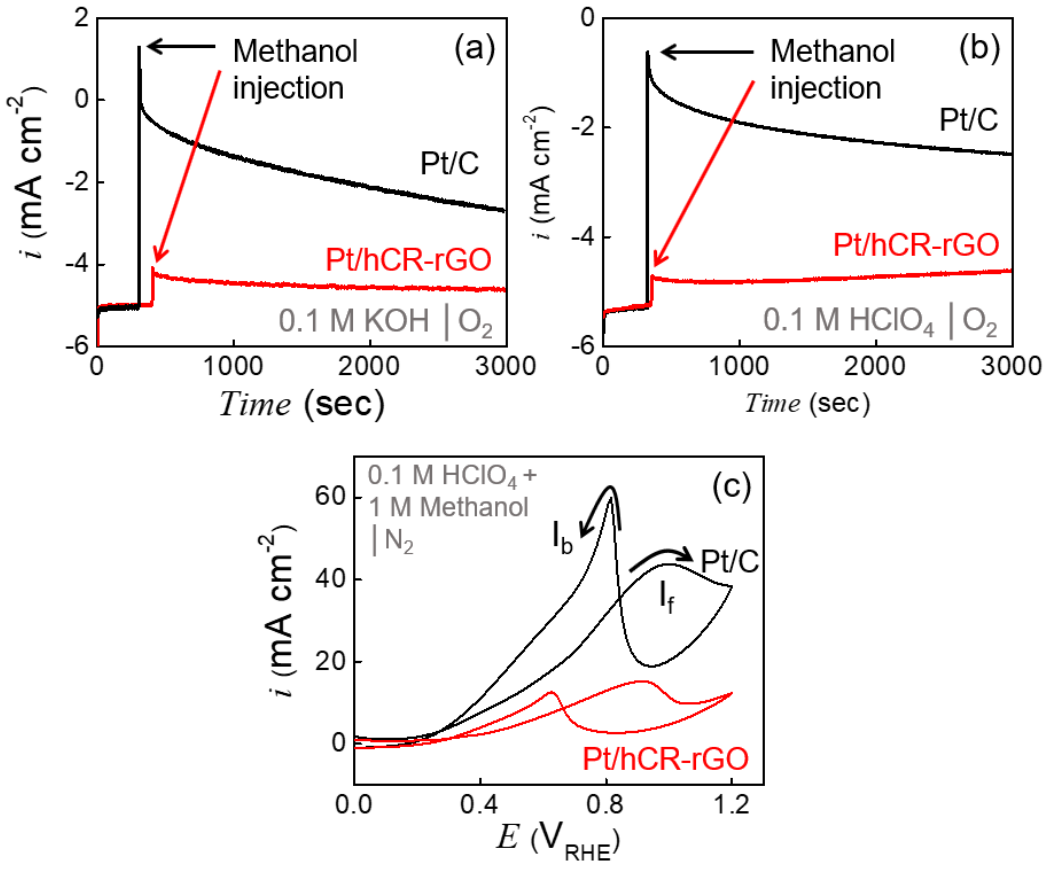


**Figure 3.7. Methanol tolerance test.** Electrolytes and purge gases were indicated in plots. Chronoamperometric responses to 1 M methanol injection at 0.63 $V_{RHE}$ in the oxygen saturated electrolyte (a for alkaline media and b for acid media). (c) Cyclic voltammograms at 50 mV $s^{-1}$ in the presence of 1M methanol.

*3.3.5. Sphere-to-multipod transmorphic change*

The increase in ECSA of Pt confined in hCR-rGO as well as the decrease in ECSA of Pt loaded on carbon black was confirmed by morphological changes in Pt along cycles. Our intention to reduce Pt agglomeration by confining Pt particles within holes (**Figure 3.1**) successfully worked in Pt/hCR-rGO when compared with Pt/C. Serious Pt agglomeration was found in Pt/C (**Figure 3.8**). Average particle size of Pt increased from 3.0 ± 0.77 nm to 9.0 ± 2.0 nm at 5,000 cycles. However, there was an insignificant change in Pt size of Pt/hCR-rGO at least up to the 5,000th cycles (**Figure 3.9a and b**). At the 10,000th cycle, more interestingly, the spherical shape of Pt nanoparticles was clearly changed to dendritic multi-pods. (**Figure 3.9c**). The morphological evolution along cycles were carefully investigated from the viewpoint of crystallographic features by atomic-resolution TEM technique (**Figure 3.9d**). Pt nanoparticles initially having multi-faceted cubic structure showed a dendritic growth of (110) planes along <100> direction. Preferential crystal growth brought {110} face-dominant multi-pod shapes, the sizes of which were limited by hole dimensions of hCR-rGO. Two merits are obtained from the dendritically evolved structure. First, the dendritic pod skeleton allows more number of active sites to be exposed to reactants, providing high active surface area. Second, Pt {110} plane is dominant on surface, which is known to exhibit high ORR activity[21].

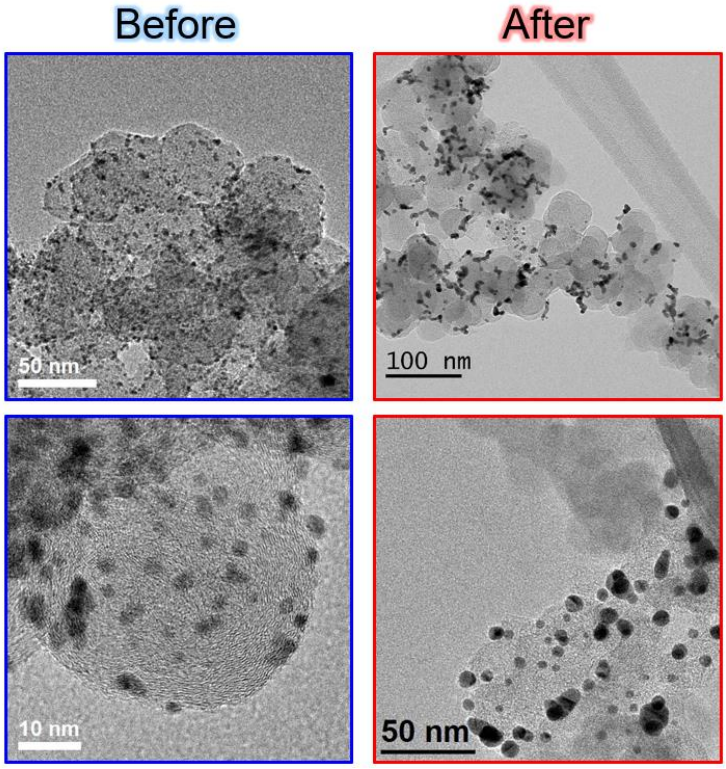


**Figure 3.8**. TEM images of a commercial Pt/C before and after the durability test described in the caption of Figure 3.11.

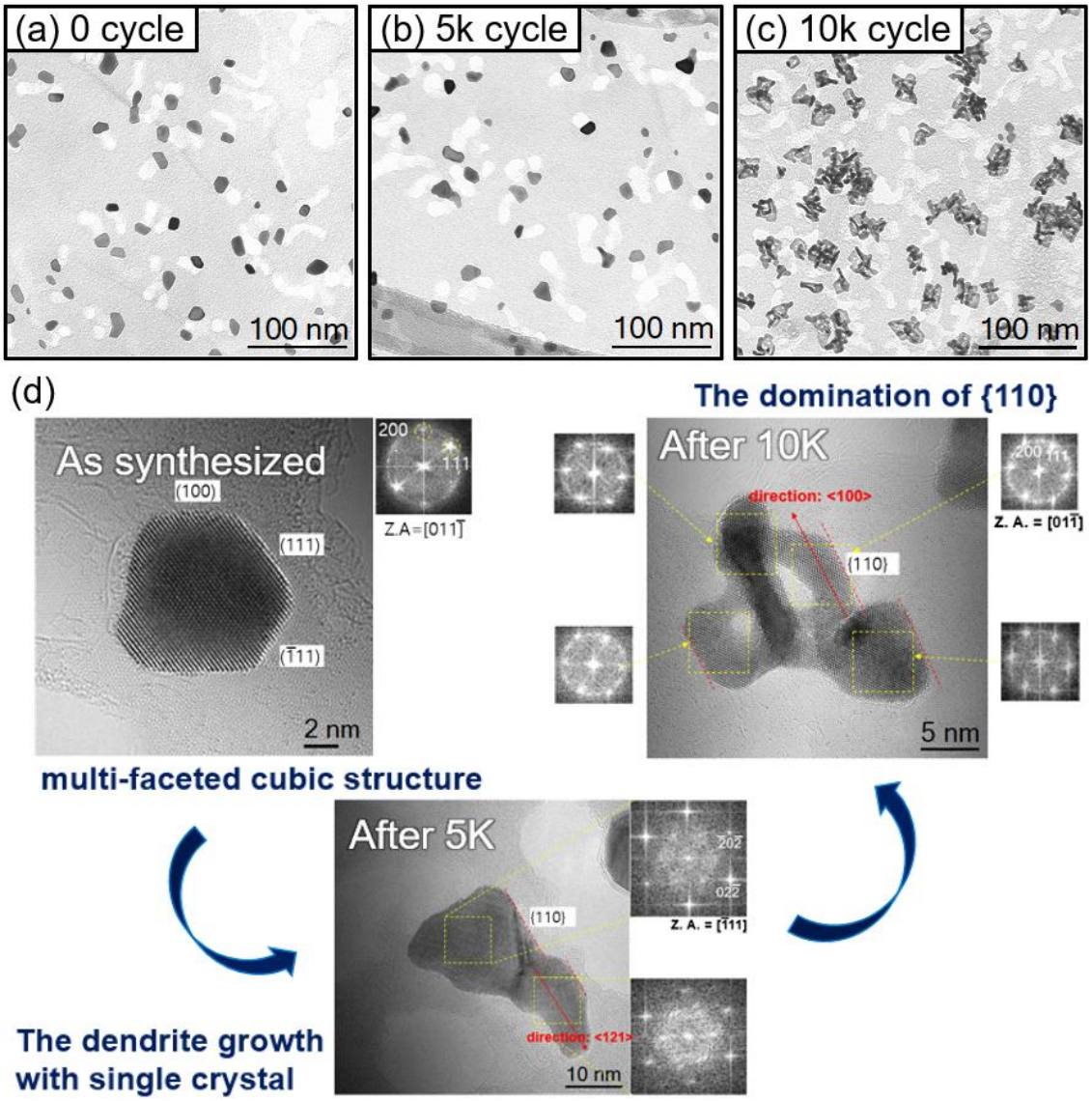


**Figure 3.9. Transmorphic evolution of Pt from sphere to dendritic multipod along cycles.** (a to d) TEM images. The cycles of potential scans were indicated: 5k =5,000; 10k = 10,000.

*3.3.6. Change in electronic structure of Pt after durability test*

Change in electronic structure of Pt loaded on supports after a durability test (refer to the caption of **Figure 3.11**) was investigated spectroscopically (**Figure 3.11**). Before the durability test, there was a gap of the binding energy of XPS Pt 4f peak between Pt/hCR-rGO and Pt/C observed (**Figure 3.11a and b**): 70.68 eV for Pt/hCR-rGO versus 71.28 eV for Pt/C. The more negative binding energy of Pt/hCR-rGO indicates that more reduced species of Pt is more dominant in Pt of Pt/hCR-rGO. Electron transfer from hCR-rGO to Pt results in stronger interaction between Pt and hCR-rGO[12, 22]. In Pt/C, however, more oxidized Pt species would be

more dominant with weaker Pt-C interaction. The electronic Pt-support interaction became stronger as Pt precursor ($H_2PtCl_6$) loaded on graphene oxide (GO) was thermally reduced to Pt/FL-rGO and the FL-rGO of Pt/FL-rGO was transformed to CR-rGO and then hCR-rGO (**Figure 3.10**).

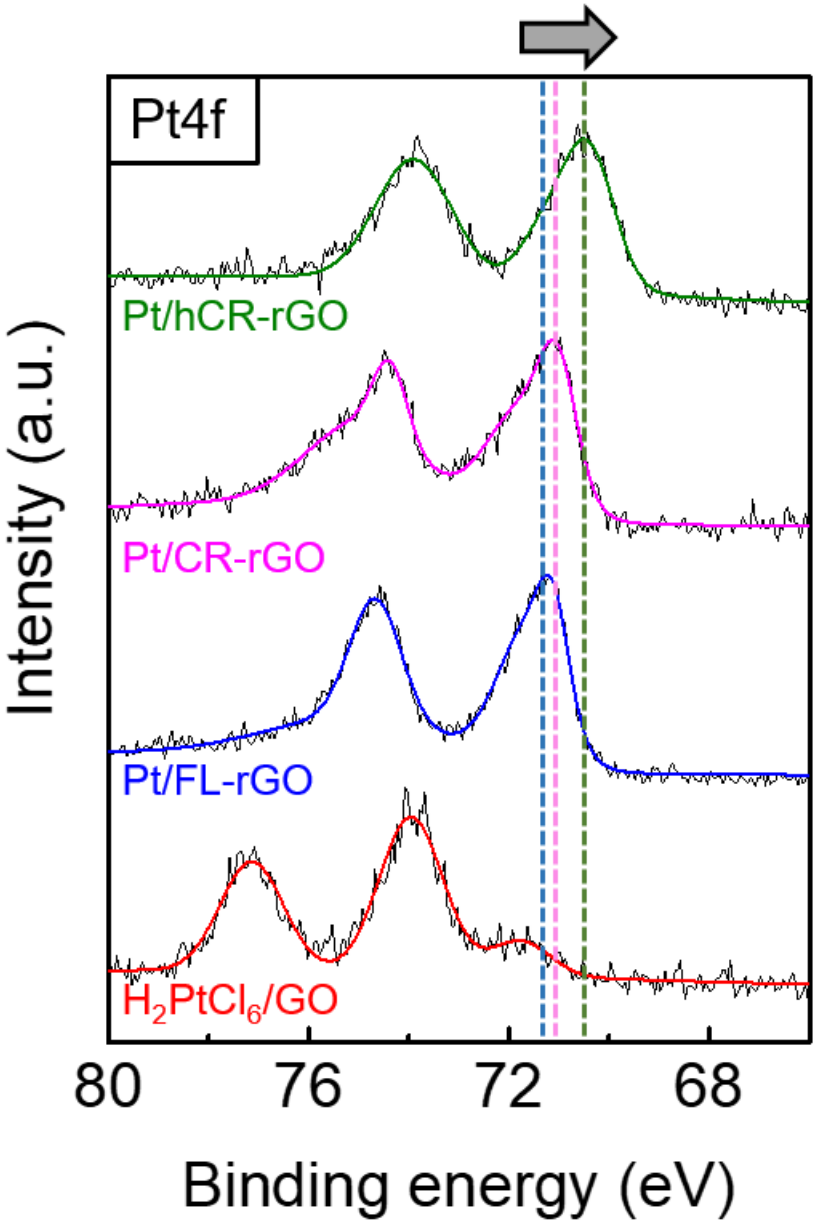


**Figure 3.10. XPS data for Pt4f spectra.** GO= graphene oxide, $H_2PtCl_6$ = Pt precursor

After the durability test, Pt/hCR-rGO exhibited no change in the Pt4f XPS spectra (**Figure 3.11a**). This invariant electronic structure of Pt, which was also confirmed by no change in Pt L3-edge XANES spectra (**Figure 3.11c**), was unexpected and surprising because the clear sphere-to-multipod transmorphic change was observed after 10,000 potential scans. In contrast, Pt/C showed a negative binding energy shift of Pt4f peak (**Figure 3.11b**). The negative shift in peak binding energy would indicate Pt aggregation caused by surface migration and/or Ostwald ripening rather than reinforced Pt-C interaction (**Figure 3.8**). The decrease in exposed surface of Pt by the agglomeration reduces the effects of high oxidation number Pt species such as surface oxide on binding energy of Pt. Less charged Pt species becomes more dominant after the aggregation, leading to the Pt4f peak shift to lower binding energy.

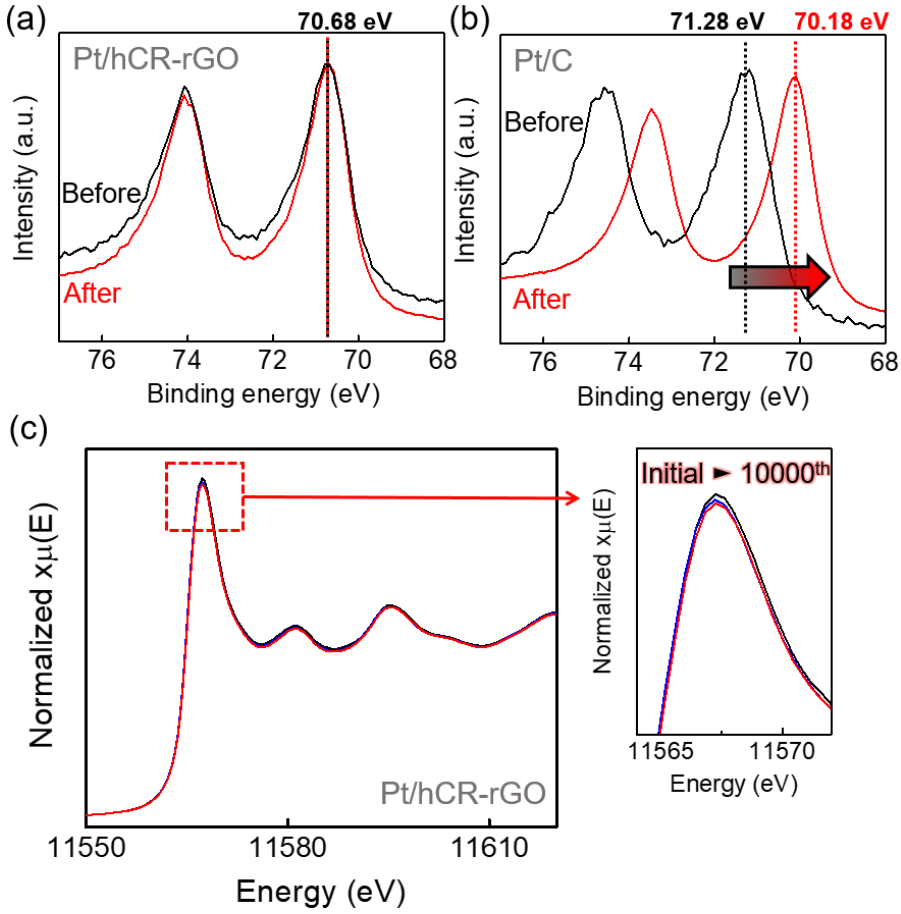


**Figure 3.11. Electronic properties of Pt on carbon supports.** (a and b) X-ray photoelectron spectroscopic (XPS) Pt 4f spectra of Pt/hCR-rGO and Pt/C before and after a durability test. The durability test was performed by sweeping potential between -0.1 $V_{RHE}$ and +1.2 $V_{RHE}$ for 10,000 cycles. Nitrogen-saturated 0.1 M $HClO_4$ solution was used. (c) Pt L3-edge X-ray adsorption near edge structure spectra (XANES) by a synchrotron light source.

*3.3.7. The mechanism of morphological change of Pt*

The electrochemically induced morphological changes of Pt, characterized by dendritic growth in shape and preferential growth in crystallography, have never been reported previously. Similar changes of bimetallic electrocatalysts ($Pt_xNi_{1-x}$ and $Pt_3Cu$) were reported[23, 24] but the mechanism suggested for the alloys cannot be applied to this single-component system. We suggest that nano-confinement of a limited number of Pt within a nano-dimensionally limited space is responsible for the morphological changes. Pt agglomeration is driven by (1) surface migration and (2) Ostwald ripening. In surface migration, Pt mass is transported along substrate surface and then agglomerated. Growth kinetics via surface migration would decrease as particle size increases (**Figure 3.12a**). Larger particles are difficult to move to meet their neighbor particles[25]. In practical situations where Pt is loaded on carbon surface (Pt/C), also, it becomes difficult to observe the Ostwald ripening as more particles are agglomerated *without* porosity developed. The number of surface Pt atoms having opportunities of dissolution becomes less due to reduced surface area of larger particles. In this work, on the other hand, the increase of Pt agglomerate size caused by surface migration is limited because only a single or a few particles are located within a restricted region. Ostwald ripening kinetics possibly increases along the growth progress only if particles are grown with more porosity developed (**Figure 3.12b**). Preferential re-deposition of dissolved Pt atoms (Ostwald ripening) favored high-surface dendritic structures (**Figure 3.9c**). Structural evolution to higher surface area accelerates Pt dissolution along growth progress. Therefore, initially spherical and multi-faceted Pt particles are disassembled and then re-assembled in a form of dendritic {110}-dominant multi-pods.

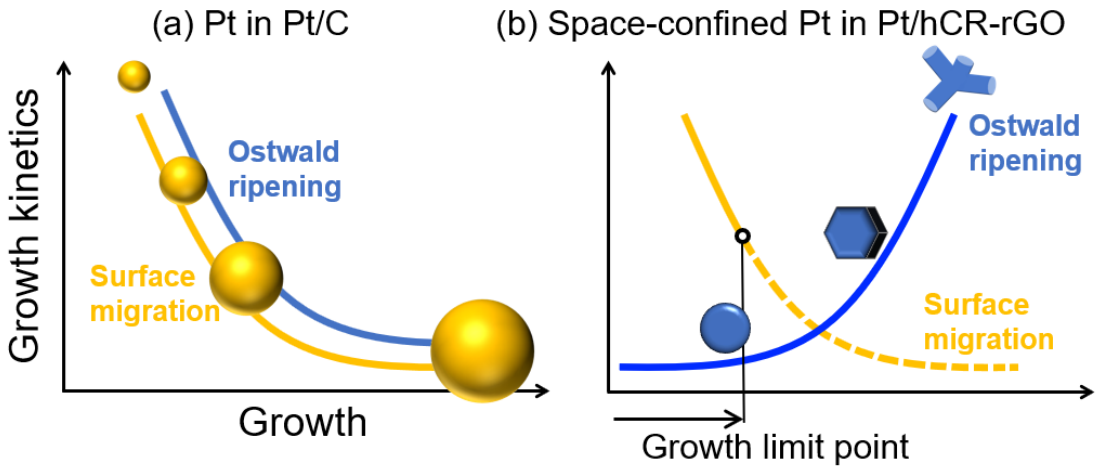


**Figure 3.12. Growth kinetics of Pt agglomeration by Ostwald ripening versus surface migration.** (a) Pt nanoparticles loaded on the surface of carbon support (Pt/C). (b) Pt nanoparticles space-confined within pores of hCR-rGO (Pt/ hCR-rGO).

### 3.4. Conclusions

In a summary, holey crumpled rGO (hCR-rGO) was prepared as a carbon support for Pt electrocatalyst for ORR. Long-term durability of Pt was remarkably improved by confining Pt particles within holes of hCR-rGO. Limited Pt mass confined within holes restricted Pt agglomeration caused by surface migration. Dominancy of Ostwald ripening in nanoconfined situations supported structural evolution from simple sphere to dendritic multi-pod. High electrochemically active area of the multi-pod and highly ORR-active {110} face dominancy on its surface supported the ORR durability of Pt/hCR-rGO.

### 3.5. References


(1) Rabis, A.; Rodriguez, P.; Schmidt, T. J. Electrocatalysis for Polymer Electrolyte Fuel Cells: Recent Achievements and Future Challenges. *ACS Catal.* **2012,** *2*, (5), 864-890.

(2) Shao-Horn, Y.; Sheng, W. C.; Chen, S.; Ferreira, P. J.; Holby, E. F.; Morgan, D. Instability of Supported Platinum Nanoparticles in Low-Temperature Fuel Cells. *Top. Catal.* **2007,** *46*, (3), 285-305.

(3) Borup, R.; Meyers, J.; Pivovar, B.; Kim, Y. S.; Mukundan, R.; Garland, N.; Myers, D.; Wilson, M.; Garzon, F.; Wood, D.; Zelenay, P.; More, K.; Stroh, K.; Zawodzinski, T.; Boncella, J.; McGrath, J. E.; Inaba, M.; Miyatake, K.; Hori, M.; Ota, K.; Ogumi, Z.; Miyata, S.; Nishikata, A.; Siroma, Z.; Uchimoto, Y.; Yasuda, K.; Kimijima, K.-i.; Iwashita, N. Scientific Aspects of Polymer Electrolyte Fuel Cell Durability and Degradation. *Chem. Rev.* **2007,** *107*, (10), 3904-3951.

(4) Bett, J. A.; Kinoshita, K.; Stonehart, P. Crystallite growth of platinum dispersed on graphitized carbon black. *J. Catal.* **1974,** *35*, (2), 307-316.

(5) Gruver, G. A.; Pascoe, R. F.; Kunz, H. R. Surface Area Loss of Platinum Supported on Carbon in Phosphoric Acid Electrolyte. *J. Electrochem. Soc.* **1980,** *127*, (6), 1219-1224.

(6) Jiang, Z.-Z.; Wang, Z.-B.; Chu, Y.-Y.; Gu, D.-M.; Yin, G.-P. Ultrahigh stable carbon riveted Pt/$TiO_2$-C catalyst prepared by in situ carbonized glucose for proton exchange membrane fuel cell. *Energy Environ. Sci.* **2011,** *4*, (3), 728-735.

(7) Maass, S.; Finsterwalder, F.; Frank, G.; Hartmann, R.; Merten, C. Carbon support oxidation in PEM fuel cell cathodes. *J. Power Sources* **2008,** *176*, (2), 444-451.

(8) Tang, H.; Qi, Z.; Ramani, M.; Elter, J. F. PEM fuel cell cathode carbon corrosion due to the formation of air/fuel boundary at the anode. *J. Power Sources* **2006,** *158*, (2), 1306-1312.

(9) del Carmen Gimenez-Lopez, M.; Kurtoglu, A.; Walsh, D. A.; Khlobystov, A. N. Extremely Stable Platinum-Amorphous Carbon Electrocatalyst within Hollow Graphitized Carbon Nanofibers for the Oxygen Reduction Reaction. *Adv. Mater.* **2016,** *28*, (41), 9103-9108.

(10) Fang, B.; Kim, J. H.; Kim, M.; Yu, J.-S. Ordered Hierarchical Nanostructured Carbon as a Highly Efficient Cathode Catalyst Support in Proton Exchange Membrane Fuel Cell. *Chem. Mater.* **2009,** *21*, (5), 789-796.

(11) Hasche, F.; Oezaslan, M.; Strasser, P. Activity, stability and degradation of multi walled carbon nanotube (MWCNT) supported Pt fuel cell electrocatalysts. *Phy. Chem. Chem. Phy.* **2010,** *12*, (46), 15251-15258.

(12) Yang, J.; Kim, S. H.; Kwak, S. K.; Song, H.-K. Curvature-Induced Metal–Support

Interaction of an Islands-by-Islands Composite of Platinum Catalyst and Carbon Nano-onion for Durable Oxygen Reduction. *ACS Appl. Mater. Interfaces* **2017,** *9*, (28), 23302-23308.

(13) Ding, J.; Chan, K.-Y.; Ren, J.; Xiao, F.-s. Platinum and platinum–ruthenium nanoparticles supported on ordered mesoporous carbon and their electrocatalytic performance for fuel cell reactions. *Electrochim. Acta* **2005,** *50*, (15), 3131-3141.

(14) Schaefer, Z. L.; Gross, M. L.; Hickner, M. A.; Schaak, R. E. Uniform Hollow Carbon Shells: Nanostructured Graphitic Supports for Improved Oxygen-Reduction Catalysis. *Angew. Chem. Int. Ed.* **2010,** *49*, (39), 7045-7048.

(15) Kim, J. H.; Fang, B.; Yoon, S. B.; Yu, J.-S. Hollow core/mesoporous shell carbon capsule as an unique cathode catalyst support in direct methanol fuel cell. *Appl. Catal. B: Environ.* **2009,** *88*, (3), 368-375.

(16) Galeano, C.; Meier, J. C.; Peinecke, V.; Bongard, H.; Katsounaros, I.; Topalov, A. A.; Lu, A.; Mayrhofer, K. J. J.; Schüth, F. Toward Highly Stable Electrocatalysts via Nanoparticle Pore Confinement. *J. Am. Chem. Soc.* **2012,** *134*, (50), 20457-20465.

(17) Xu, Y.; Lin, Z.; Zhong, X.; Huang, X.; Weiss, N. O.; Huang, Y.; Duan, X. Holey graphene frameworks for highly efficient capacitive energy storage. *Nat. Commun.* **2014,** *5*, 4554.

(18) Han, X.; Funk, M. R.; Shen, F.; Chen, Y.-C.; Li, Y.; Campbell, C. J.; Dai, J.; Yang, X.; Kim, J.-W.; Liao, Y.; Connell, J. W.; Barone, V.; Chen, Z.; Lin, Y.; Hu, L. Scalable Holey Graphene Synthesis and Dense Electrode Fabrication toward High-Performance Ultracapacitors. *ACS Nano* **2014,** *8*, (8), 8255-8265.

(19) Ma, X.; Zachariah, M. R.; Zangmeister, C. D. Crumpled Nanopaper from Graphene Oxide. *Nano Lett.* **2012,** *12*, (1), 486-489.

(20) Zhu, Y.; Murali, S.; Stoller, M. D.; Ganesh, K. J.; Cai, W.; Ferreira, P. J.; Pirkle, A.; Wallace, R. M.; Cychosz, K. A.; Thommes, M.; Su, D.; Stach, E. A.; Ruoff, R. S. Carbon-Based Supercapacitors Produced by Activation of Graphene. *Science* **2011,** *332*, (6037), 1537-1541.

(21) Khudhayer, W. J.; Kariuki, N. N.; Wang, X.; Myers, D. J.; Shaikh, A. U.; Karabacak, T. Oxygen Reduction Reaction Electrocatalytic Activity of Glancing Angle Deposited Platinum Nanorod Arrays. *J. Electrochem. Soc.* **2011,** *158*, (8), B1029-B1041.

(22) Xie, X.; Chen, S.; Ding, W.; Nie, Y.; Wei, Z. An extraordinarily stable catalyst: Pt NPs supported on two-dimensional $Ti_3C_2X_2$ (X = OH, F) nanosheets for oxygen reduction reaction. *Chem. Commun.* **2013,** *49*, (86), 10112-10114.

(23) Kuang, Y.; Zhang, Y.; Cai, Z.; Feng, G.; Jiang, Y.; Jin, C.; Luo, J.; Sun, X. Single-crystalline dendritic bimetallic and multimetallic nanocubes. *Chem. Sci.* **2015,** *6*, (12),

7122-7129.

(24) Cui, C.; Gan, L.; Heggen, M.; Rudi, S.; Strasser, P. Compositional segregation in shaped Pt alloy nanoparticles and their structural behaviour during electrocatalysis. *Nat. Mater.* **2013,** *12*, 765.

(25) Harris, P. J. F. Growth and structure of supported metal catalyst particles. *Int. Mater. Rev.* **1995,** *40*, (3), 97-115.

# Publications

1. **Juchan Yang**[†]**,** Dong Woo Kang[†], Hu Young Jeong*, Hyeon Suk Shin*, Hyun-Kon Song*, "Sphere-to-multipod transmorphic change of nanoconfined Pt electrocatalyst during oxygen reduction reaction", Under review in Small. **([†]Authors contributed equally)**
2. Minsoo P. Kim[†], Jinhyup Han[†], **Juchan Yang**, Hyun-Kon Song, Hyunhyup Ko, Kyoungho Kim*, "Seawater battery using conducting hydrogel-based electrode for chloride ion capturing", submitted to ChemSusChem.
3. Seungyoung Park, **Juchan Yang**, Su Hwan Kim, Hyun-Kon Song, Sang Kyu Kwak, Hyunhyup Ko*, "NiFe layered double hydroxide nanosheets with co-doped Fe and V as efficient oxygen evolution electrocatalyst", submitted to Nature communication.
4. Ziyauddin Khan, **Juchan Yang**, Seungyoung Park, Youngsu Lee, Hyun-Kon Song, Hyunhyup Ko*, "Binary N, S-doped carbon nanospheres from bio-inspired artificial melanosomes: Route to efficient air electrodes for seawater flow batteries", submitted to Advanced Science.
5. **Juchan Yang**, Seungyoung Park, Kyoung young Choi, Han-Saem Park, Yoon-Gyo Cho, Hyunhyub Ko, Hyun-Kon Song*, "Activity-durability coincidence of oxygen evolution reaction in the presence of carbon corrosion", Accepted to ACS Sustainable Chemistry & Engineering.
6. **Juchan Yang**, Seok min Shin, Jinhyup Han, Han-Saem Park, Youngsik Kim, Hyun-Kon Song*, "Efficient use of oxygen catalyst induced by capacitance currents in metal-air battery", Under review in Journal of Power Sources.
7. Han-Saem Park[†], **Juchan Yang**[†], Min Kyung Cho, Yeongdae Lee, Seonghun Cho, Sung-Dae Yim, Byeong-Su Kim, Jong Hyun Jang, Hyun-Kon Song*, "$RuO_2$ nanocluster as a 4-in-1 electrocatalyst for hydrogen and oxygen electrochemistry", Under review in Nano Energy. **([†]Authors contributed equally)**
8. V.S. Dilimon, Chihyun Hwang, Yoon-Gyo Cho, **Juchan Yang**, Hee Dae Lim, Kisuk Kang, Seok Ju Kang, Hyun-Kon Song*, *"Superoxide stability for reversible Na-$O_2$ electrochemistry"*, Scientific Reports, 7, (2017), 17635.
9. Chihyun Hwang, Sinho Choi, Gwan Yeong Jung, **Juchan Yang**, Sang Kyu Kwak, Soojin Park*, Hyun-Kon Song*, *"Graphene-wrapped porous Sb anodes for sodium-ion batteries by mechanochemical compositing and metallomechanical reduction of $Sb_2O_3$"*, Electrochimica acta, 252, (2017), 25-32.
10. Han-Saem Park[†], Eunyong Seo[†], **Juchan Yang**, Yeongdae Lee, Byeong-Su Kim*, Hyun–Kon Song*, Youngsik Kim, *"Bifunctional hydrous $RuO_2$ nanocluster electrocatalyst*

*embedded in carbon matrix for efficient and durable operation of rechargeable zinc-air batteries"*, Scientific Reports, 7, (2017), 7150.

11. **Juchan Yang†,** Su Hwan Kim†, Sang Kyu Kwak*, Hyun–Kon Song*, *"Curvature-Induced Metal-Support Interaction of an Islands-by-Islands Composite of Platinum Catalyst and Carbon Nano-onion for Durable Oxygen Reduction"*, ACS Applied Materials & Interfaces, 9, (2017) 23302-23308. **(†Authors contributed equally)**
12. Ziyauddin Khan†, B. Senthilkumar†, Sung O Park†, Seungyoung Park, **Juchan Yang**, Jeong Hyeon Lee, Hyun–Kon Song, Youngsik Kim, Sang Kyu Kwak*, and Hyunhyub Ko*, *"Carambola Shaped $VO_2$ Nanostructures: A Binder–Free Air Electrode for Aqueous Na–Air Battery"*, Journal of Materials Chemistry A, 5, (2017), 2037-2044.
13. Mari Abirami, Soo Min Hwang*, **Juchan Yang**, Sirugaloor Thangavel Senthilkumar, Junsoo Kim, Woo-Seok Go, Baskar Senthilkumar, Hyun-Kon Song, and Youngsik Kim*, *"A Metal−Organic Framework Derived Porous Cobalt Manganese Oxide Bifunctional Electrocatalyst for Hybrid Na−Air/Seawater Batteries"*, ACS Applied Materials & Interfaces, 8, (2016), 32778-32787.
14. Ziyauddin Khan, Seungyoung Park, Soo Min Hwang, **Juchan Yang**, Youngsu Lee, Hyun-Kon Song, Youngsik Kim*, Hyunhyub Ko*, *"Hierarchical Urchin-Shaped α-$MnO_2$ on Graphene-Coated Carbon Microfibers: A Binder-Free Electrode for Rechargeable Aqueous Na-Air Battery"*, NPG asia materials, 8, (2016), e294
15. Dong-Gyu Lee, Ohhun Gwon, Han-Saem Park, Su Hwan Kim, **Juchan Yang**, Sang Kyu Kwak, Guntae Kim*, Hyun-Kon Song*, *"Conductivity-Dependent Completion of Oxygen Reduction on Oxide Catalysts"*, Angewandte Chemie International Edition, 54, (2015), 15730-15733.
16. **Juchan Yang**, Yan Zhang, Doo Young Kim*, *"Electrochemical sensing performance of nanodiamond-derived carbon nano-onion: comparison with multiwalled carbon nanotubes, graphite nanoflake, and glassy carbon"*, Carbon, 98, (2016), 74-82.
17. Joonho Bae, Young Jun Park, **Ju Chan Yang**, Hyoun Woo Kim, Doo Young Kim. *"Toward wearable and stretchable fabric-based supercapacitors: Novel ZnO and SnO2 nanowires-carbon fiber and carbon paper hybrid structure"*, Journal of Solid State Electrochemistry, 19, (2015.01), 211-219
18. Rituraj Borgohain, **Ju Chan Yang**, John P. Selegue*, Doo Young*, *"Controlled synthesis, efficient purification, and electrochemical characterization of arc-discharge carbon nano-onions"*, Carbon, 66, (2014.01) 272-284.
19. Han Gil Na, **Ju Chan Yang**, Dong Sub Kwak, Yong Jung Kwon, Chongmu Lee, Sang Sub Kim, Hyoun Woo Kim*, *"Drastic improvement of sensing characteristics in $SnO_2$*

*nanowires by functionalizing with Pt"*, Journal of Nanoscience and Nanotechnology 13 (2013.09) 6216-6221.

20. **Ju Chan Yang**, Han Gil Na, Dong Sub Kwak, Hyoun Woo Kim*, *"ZnO-cored hetero nanowires sheathed with Cu shells: Structural, magnetic, and photoluminescence properties"*, Surface and Coatings Technology, 228 (2013.08.15) S374-S378
21. Hyoun Woo Kim*, **Ju Chan Yang**, Han Gil Na, Dong Sub Kwak, Chongmu Lee, "*Generation of $Zn_2SiO_4$ nanocrystallites in a shell of ZnO/$SiO_x$ core-shell nanowires to change photoluminescence properties"*, Metals and Materials International 18 (2012.08) 705-710.
22. Hyoun Woo Kim, Han Gil Na, Joonho Bae, **Ju Chan Yang**, Sung Soo Kim, Hyeon sik Cheong, Doo Young Kim*, *"Synthesis and Characterization of Orthorhombic $Sb_2O_4$ Nanowire Prepared by Heating $Sb_2S_3$ Powder",* Electrochemical and Solid-State Letters, 15 (2012.04) K49-K52.
23. Han Gil Na, **Ju ChanYang**, Dong Sub Kwak, Hyoun Woo Kim*, *"Bismuth-catalyzed synthesis of ZnO nanowires and their photoluminescence properties*", Ceramics International 38 (2012.07) 3659-3666.
24. Hyoun Woo Kim, Han Gil Na, **Ju Chan Yang**, Dong Sub Kwak *"Tailoring the photoluminescence of MgO nanowires using the Ag shell layers and nanoparticles",* Thin Solid Films 520 (2012. 01.31) 2627-2631.
25. Sang Sub Kim, Jae Young Park, Sun-Woo Choi, Han Gil Na, **Ju Chan Yang**, Dong Sub Kwak, Hyun Jung Nam, Chang Kwon Hwangbi, Hyoun Woo Kim* *"Drastic change in shape of tetragonal $TeO_2$ nanowires and their application to transparent chemical gas sensors"*, Applied Surface Science 258 (2011.10.15) 501-506.
26. Sang Sub Kim, Jae Young Park, Sun-Woo Choi, Han Gil Na, **Ju Chan Yang**, Hyoun Woo Kim* *"Enhanced $NO_2$ sensing characteristics of Pd-functionalized networked $In_2O_3$ nanowires"*, Journal of Alloys and Compounds 509 (2011.09.15) 9171-9177
27. Hyoun Woo Kim*, **Ju Chan Yang**, Han Gil Na, Chong mu Lee *"Atomic layer deposition coating of ZnO shell for GaN-ZnO core-sheath hetero nanowires"*, Applied Surface Science 257 (2011.09.01) 9420-9424.
28. Hyoun Woo Kim*, Han Gil Na, **Ju Chan Yang**, Chong mu Lee *"Temperature-controlled synthesis of $Zn_2GeO_4$ nanowires in a vapor-liquid-solid mode and their photoluminescence properties"*, Chemical Engineering Journal 171(2011.07) 1439-1445.
29. Doo Young Kim, **Ju Chan Yang**, Hyoun Woo Kim, Greg M. Swain*, *"Heterogeneous electron-transfer rate constants for Ferrocene and Ferrocene Carboxylic acid at Boron-*

*doped diamond electrodes in a room temperature ionic liquid"*, Electrochimica Acta, 94 (2013.02) 49-56.

30. Doo Young Kim, Jian Wang, **Ju Chan Yang**, Hyoun Woo Kim, Greg M. Swain* *"Electrolyte and Temperature Effects on the Electron Transfer Kinetics of $Fe(CN)_6^{-3/-4}$ at Boron-Doped Diamond Thin Film Electrodes"*, The Journal of Physical Chemistry C 115 (2011.05) 10026-10032.
31. Hyoun Woo Kim*, Hyo Sung Kim, Han Gil Na, **Ju Chan Yang**, *"Silica-coated ZnO nanowires"*, Vacuum 86 (2012.01.27) 789-793.
32. Sang Sub Kim, Sun-Woo Choi, Chongmu Lee, **Ju ChanYang**, Han Gil Na, Dong Sub Kwak, Hyoun Woo Kim*, "*Temperature-induced evolution of novel mixture-phased particles at the tips of $SnO_2$ whiskers"*, Chemical Engineering Journal 179 (2012.01.01) 381-387.
33. Hyoun Woo Kim*, Han Gil Na, **Ju Chan Yang**, Jinho Ahn, Chong Seung Yoon, Heon Ham, Kwang Bo Shim, Chang hwan Choi, In pil Kang, Jae Hak Yang, Chong mu Lee *"Annealing-induced enhancement of ferromagnetism in $SnO_2$-core/Cu-shell coaxial nanowires"*, Metals and Materials International 17 (2011.08.31) 641-647.
34. Hyoun Woo Kim*, Han Gil Na, **Ju Chan Yang** *"Simply heating to remove the sacrificial core $TeO_2$ nanowires and to generate tubular nanostructures of metal oxides"*, Chemical Engineering Journal, 170 (2011.05) 326-332.
35. Hyo Sung Kim, Han Gil. Na, **Ju Chan Yang**, Chong mu. Lee, Hyoun Woo Kim *"Synthesis, Structure, Photoluminescence, and Raman Spectrum of Indium Oxide Nanowires"*, Acta Physica Polonica A 119 (2011.02) 143-145.
36. **Ju Chan Yang**, Han Gil Na, Hyo Sung Kim, M.A. Kebede, Rino Choi, Jae.Kyung Jeong, Chong mu Lee, Hyoun Woo Kim *"Photoluminescence Studies of Aluminum Nitride Nanowires"*, Acta Physica Polonica A 119 (2011.02) 125-127.
37. Sang Sub Kim, Jae Young Park, Sun-Woo Choi, Hyo Sung Kim, Han Gil Na, **Ju Chan Yang**, Chong mu Lee, Hyoun Woo Kim* *"Room temperature sensing properties of networked GaN nanowire sensors to hydrogen enhanced by the $Ga_2Pd_5$ nanodot functionalization"*, International Journal of Hydrogen Energy 36 (2011.02) 2313-2319.
38. Hyoun Woo Kim*, Hyo Sung Kim, Han Gil Na, **Ju Chan Yang**, Mesfin Abayneh Kebede, Chong mu Lee *"Growth of $Sb_2O_3$ submicron rods by the thermal evaporation of a mixture of Zn and Sb powders"*, Ceramics International 37 (2011.02) 593-598.
39. Sang Sub Kim, Jae Young Park, Hyo Sung Kim, Han Gil Na, **Ju Chan Yang**, Seung Hyun Shim, Chong mu Lee, Do young Park, Da hyun Nam, Hyeon sik Cheong, Hyoun Woo Kim* *"Temperature-controlled synthesis of $In_2Ge_2O_7$ nanowires and their photoluminescence properties"*, Journal of Physics D: Applied Physics 44 (2011) 025502.

40. Hyo Sung Kim, Han Gil Na, **Ju Chan Yang**, Chong mu Lee, Hyoun Woo Kim* *"GaN-based core-shell nanowires sputtered with Pd target and their annealing characteristics"*, Surface & Coatings Technology 205 (2010.12.25) S90-S95.
41. Hyoun Woo Kim*, Hyo Sung Kim, Han Gil Na, **Ju Chan Yang**, Sang Sub Kim, Chong mu Lee *"Self-catalytic growth and characterization of composite (GaN,InN) nanowires"*, Chemical Engineering Journal 165 (2010.12) 720-727.
42. Hyoun Woo Kim*, Hyo Sung Kim, Han Gil Na, **Ju Chan Yang**, Rino Choi, Jae Kyeong Jeong, Chongmu Lee, Doo Young Kim *"One-step fabrication and characterization of silica-sheathed ITO nanowires"*, Journal of Solid State Chemistry 183 (2010.10) 2490-2495.
43. Hyo Sung Kim, Han Gil Na, **Ju Chan Yang**, Jong Hoon Jung, Yong Sung Koo, Nam Hung Hur, Hyoun Woo Kim* *"Annealing effects on the structure, photoluminescence, and magnetic properties of GaN/$Mn_3O_4$ core-shell nanowires"*, Journal of Solid State Chemistry 183 (2010.10) 2445-2450.
44. Sang Sub Kim, Jae Young Park, Sun-Woo Choi, Hyo Sung Kim, Han Gil Na, **Ju Chan Yang**, Hyoun Woo Kim* *"Significant enhancement of the sensing characteristics of $In_2O_3$ nanowires by functionlization with Pt nanoparticles"*, Nanotechnology 21 (2010.10.15) 415502.
45. Hyoun Woo Kim*, Hyo Sung Kim, Han Gil Na, **Ju Chan Yang**, Doo Young Kim *"Growth, structural, Raman, and photoluminescence properties of rutile $TiO_2$ nanowires synthesized by the simple thermal treatment"*, Journal of Alloys and Compounds 504 (2010.08.13) 217-213.
46. Hyoun Woo Kim*, Hyo Sung Kim, Han Gil Na, **Ju Chan Yang**, Chongmu Lee *"Preparation and annealing of GaN/Cu core-shell nanowires"*, Journal of Alloys and Compounds 500 (2010.06.25) 175-180.
47. Hyoun Woo Kim*, Han Gil Na, **Ju Chan Yang**, Hyo Sung Kim, Ji-Hye Lee, and Keon-Ho Yoo, *"Fabrication and Characteristics of β-$Bi_2O_3$ Nanowires Prepared by Heating a Mixture of In and Bi Powders"*, Electrochemical and Solid State Letters 13 (7) (2010.04.15) K67-K71
48. **Ju Chan Yang**, Han Gil Na, Msefin Abayneh Kebede, Hyo Sung Kim, Hyoun Woo Kim* *"GaN-cored heteronanowires sheathed with Pt shells: Preparation and annealing studies"*, Journal of Crystal Growth 312 (2010.04.01) 1199-1204.
49. Hyoun Woo Kim*, Mesfin Abayneh Kebede, Hyo Sung Kim, Han Gil Na, **Ju Chan Yang**, Chongmu Lee *"Effect of temperature on GaN nanowires fabricated via thermal heating of GaN powders"*, Metals and Materials International 16 (2010.02.26) 87-91.

50. Hyoun Woo Kim*, Hyo Sung Kim, Mesfin Abayneh Kebede, Han Gil Na, **Ju Chan Yang** *"$SnO_2$-Core/$SiO_x$-shell coaxial whiskers with a needle-like morphology"*, Metals and Materials International 16 (2010.02.26) 77-81.
51. Hyoun Woo Kim*, Seung Hyun Shim, Jong Woo Lee, Hyo Sung Kim, Mesfin Abayneh Kebede, Han Gil Na, **Ju Chan Yang**, Myung Ho Kong, Chongmu Lee *"Fabrication and annealing effects of $SnO_2/SiO_x$ nanocables sheathed by the sputtering technique"*, Current Applied Physics 10 (2010.01) 47-51.
52. Hyoun Woo Kim*, Hyo Sung Kim, Mesfin Abayneh Kebede, Han Gil Na, **Ju Chan Yang**, Yong Sung Koo, Jong Hoon Jung, Nam Jung Hur *"Co-sheathed $SiO_x$ nanowires"*, Applied Surface Science 255 (2009.07.30) 8425-8429.
53. Hyoun Woo Kim*, Hyo Sung Kim, Mesfin Abayneh Kebede, Han Gil Na, **Ju Chan Yang**, Chongmu Lee *"Structural and photoluminescence properties of GaN/ZnO core-shell nanowires with their shells sputtered"*, Crystal Research and Technology 44 (2009.06) 636-640.

# Acknowledgements

**"내게 능력 주시는 자 안에서 내가 모든 것을 할 수 있느니라" (빌립보서 4장 13절)**

**"*I can do everything through him who gives me strength.*" (Philippians 4:13, NIV)**

시작하게 하시고 약속대로 유종의 미를 거두게 하신 나의 왕 되신 하나님께 제일 먼저 감사드리며 영광을 돌려 드립니다. 어려움과 고난이 있을 때에서도 하나님이 주신 약속을 붙잡고 나아갈 수 있게 해주셔서 감사드립니다. 또한, 늘 매순간과 작은 호흡 하나도 나와 동행하여 주셔서 감사드립니다. 주님이 주신 사명 기억하면서 주님의 계획대로 쓰임 받는 일꾼이 되길 소망합니다.

박사과정의 배움의 길을 걸어오는 동안, 늘 좌우명처럼 생각하였던 문구 "뜨는 해를 아끼자". 너무 바쁘게 살아오다 보니, 감사의 글을 쓰는 이 순간에 비로소 가장 먼저 생각나는 소중한 단어가 있습니다. 감사입니다. 삶이 행복해서 감사한 사람이 아니라 감사할 줄 알아서 삶이 행복한 사람이 되길 소망하며 그 소중한 단어의 보따리를 풀어보고자 합니다.

가장 먼저 나의 사랑하는 아버지, 어머니. 배움의 긴 여정동안, 두 분의 매일 새벽을 깨우는 끊임없는 기도와 아들을 향한 신뢰 너무나 감사드립니다. 두 분의 사랑과 헌신 없이는 그 어떤 것도 이야기할 수가 없습니다. 앞으로도 두 분의 기도에 맞게 사명 감당하는 아들이 되도록 노력하겠습니다. 항상 기도해주고 그 어떤 상황에도 응원해준 우리 친누나에게도 감사를 전합니다.
그리고, 어떤 순간에도 늘 내 편이 되어 주시고 힘이 되어 주신 장인/장모님 진심으로 감사드립니다. 마지막 발표 마치고 축하한다 자랑스럽다 말씀해 주셔서 감사드립니다. 앞으로 더 좋은 모습으로 성장하여 보답할 수 있도록 노력하겠습니다. 만나면 즐겁고 늘 웃음으로 응원해준 처남 경승이, 처제 내외에게도 고마운 마음을 전합니다.

학위과정동안 **同苦同樂**(동고동락)했던 eclat 여러분 감사합니다. 먼저, 가장 좋은 연구환경을 만들어 주시고 연구 기회를 풍부하게 주신 송현곤 지도교수님 감사드립니다. 교수님께로부터 배운 지식과 보고 들은 삶의 교훈을 가득 안고 갈 수 있어서 감사드립니다. 더 멋진 연구자의 모습으로 보답 드릴 것을 약속드립니다. 같은 연구를 하면서 연구와 삶속에서 서로 의지가 되고 힘이 되었던 한샘형님. 먼저 필드에 나가셨지만, 형님 말처럼 서로의 길이 어떻게 될지 모르지만 늘 힘이 되었으면 좋겠습니다. 그리고 다시 한번 결혼 축하드립니다. 연구실에서 나의 농담과 장난을 기쁘게 받아주던 중학교 대학교 후배 황치현 박사. 당신이 꿈꾸

는 멋진 연구자가 되길 소망합니다. 유일하게 육아와 연구에 있어 대화가 가능했던 명희누나, 늘 부지런하게 노력하면서 사는 윤교, 랩생활은 개선이 많이 필요하지만 나와는 좋은 기억으로 남게 될 동규, 늘 언제나 매사에 최선을 다하고 TEM 많이 찍어줘서 고마운 유주, 운동경기 이야기에 말벗이 되어준 도형이, 열심히 노력하려고 하는 영대 그리고 착한 종학이 모두 감사합니다. 그 외 함께했던 eclat 가족에게도 감사의 마음을 전합니다. 즐거웠거나 얼굴 찌푸리는 일들 모두 여러분과의 추억으로 남아서 저의 인생의 한 페이지를 만들 수 있어서 기뻤습니다.

UNIST에서 만난 많은 사람들이 저에게는 큰 자산입니다. 미국에서 UNIST로 올 때 먼저 손내밀어 주신 신현석 교수님과 LNN 연구실분들, 심사위원으로 승락해주시고 날카로운 지적과 격려를 아낌없이 주신 백종범, 주상훈, 김영식 교수님, 훌륭한 co-worker 진협씨, 승영씨, 그리고 LNN에서 큰 힘이 되어주었던 동우씨, 연구지원 본부 선생님들, 특히 김영기 선생님 감사드립니다.

학위기간동안 신앙의 안식처가 되어준 울산 태화교회 분들 감사드립니다. 매주 말씀으로 붙잡게 해주신 양성태 목사님, 학교까지 찾아와 늘 응원해 주신 최용근 목사님, 만날 때 마나 환한미소로 힘이 되어주신 허진 목사님, 아무도 없는 울산 땅에서 우리 가정을 가족처럼 돌보아 주신 목자님과 목장식구 분들, 언제나 신앙의 깊은 원동력이 되어준 나의 모교회 일산충만한 교회와 임다윗 목사님, 가족처럼 늘 나와 우리 가정을 위해 기도해주시고 어머니같이 챙겨 주시는 우리 배은주 전도사님 너무 감사드립니다. 모든 분들의 기도와 격려에 맞는 사람이 되도록 노력하겠습니다.

마지막으로 나의 사랑하는 아내 현아와 사랑과 희망이 되는 아들 의성이. 사랑할 수 있는 존재가 있다는 것이 큰 기쁨을 가져다준다는 것을 알게 해주어서 감사합니다. 가족의 헌신과 희생 없이는 이룰 수 없었을 것입니다. 아침에 출근해서 다음날 새벽에 귀가하는 여유가 없는 삶의 일과였지만, 나를 위해 매일같이 가족이라는 이름으로 기다려주고 뒷바라지해준 와이프와 이런 아빠를 세상 누구보다 좋아해주는 우리 아들에게 진심으로 고맙다고 말하고 싶습니다. 그리고 사랑합니다.

미처 지면에 다 표현하지 못한 분들께도 감사의 인사를 드립니다. 많은 분들이 주신 사랑과 하나님께서 보여주신 사랑을 기억하면서 그 사랑을 흘려보내면서 사는 제가 될 것을 약속드립니다. 감사합니다.